

Generalized (Wiener-Askey) Polynomial Chaos

by

Dongbin Xiu

Sc.M., Mechanical Engineering, The University of Virginia, 1999

B.S., Department of Mechanics, Zhejiang University, P.R.China, 1993

Thesis

Submitted in partial fulfillment of the requirements for
the degree of Doctor of Philosophy
in the Division of Applied Mathematics at Brown University

May 2004

UMI Number: 3134379

INFORMATION TO USERS

The quality of this reproduction is dependent upon the quality of the copy submitted. Broken or indistinct print, colored or poor quality illustrations and photographs, print bleed-through, substandard margins, and improper alignment can adversely affect reproduction.

In the unlikely event that the author did not send a complete manuscript and there are missing pages, these will be noted. Also, if unauthorized copyright material had to be removed, a note will indicate the deletion.

UMI[®]

UMI Microform 3134379

Copyright 2004 by ProQuest Information and Learning Company.

All rights reserved. This microform edition is protected against unauthorized copying under Title 17, United States Code.

ProQuest Information and Learning Company
300 North Zeeb Road
P.O. Box 1346
Ann Arbor, MI 48106-1346

© Copyright

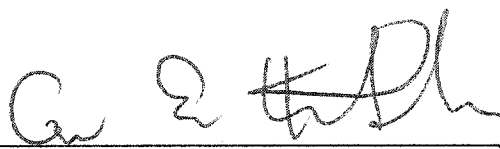
by

Dongbin Xiu

2004

This dissertation by Dongbin Xiu is accepted in its present form by
the Division of Applied Mathematics as satisfying the
dissertation requirement for the degree of
Doctor of Philosophy

Date 9/12/2003



George Em Karniadakis, Director

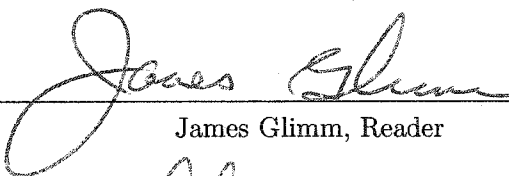
Recommended to the Graduate Council

Date 9/12/2003



David Gottlieb, Reader

Date 9/22/2003



James Glimm, Reader

Date 9/15/03



Roger Ghanem, Reader

Approved by the Graduate Council

Date 9/30/03



Karen Newman

Dean of the Graduate School

Abstract of “Generalized (Wiener-Askey) Polynomial Chaos,” by Dongbin Xiu, Ph.D.,
Brown University, May 2004

A new methodology for uncertainty quantification in practical applications is developed. The method, termed as ‘generalized polynomial chaos’ or ‘Wiener-Askey polynomial chaos’, is an extension of the mathematical theory of Norbert Wiener (1938). The original Wiener’s polynomial chaos employs *Hermite* orthogonal polynomials in terms of *Gaussian* random variables to represent stochastic processes. This approach was adopted by Ghanem and his co-workers, who have conducted extensive research on uncertainty quantification via the Wiener-Hermite expansions in various areas. The generalized polynomial chaos is a broader framework which includes the Wiener-Hermite polynomial chaos as a subset. In addition to Hermite polynomials, more orthogonal polynomials from the Askey scheme are employed as the expansion bases in random space. Accordingly, the random variables in the basis functions are not necessarily Gaussian, and are determined by the random inputs to achieve fast convergence. Several types of *discrete* expansions are also incorporated that increase further the flexibility of generalized polynomial chaos. In the first part of this thesis, the construction of generalized polynomial chaos is presented and its mathematical properties examined. We then apply it to various differential equations subject to random inputs, including elliptic equations, parabolic equations, advection-diffusion equations, and Navier-Stoke equations. The results of generalized polynomial chaos are examined in model problems, and exponential convergence is demonstrated when the exact solutions are known and the appropriate type of chaos is employed. For model problems without explicit exact solutions, we validate the results by conducting Monte Carlo simulations. It is shown that the cost of generalized polynomial chaos is, in many cases, significantly lower than that of Monte Carlo methods, and that the generalized polynomial chaos can serve as an effective means for uncertainty quantification in real systems.

Citizenship:

People's Republic of China

Education:

- University of Virginia, Master of Science in Mechanical Engineering, May 1999.
Thesis Title: "Numerical Simulation of Vortex Breakdown in an Eccentric Spherical Gap"
Advisor: Professor Hossein Haj-Hariri
- Zhejiang University, P.R.China, Bachelor of Science in Department of Mechanics, June 1993.
Thesis Title: "Numerical Simulation of Incompressible Flows in Complex Geometry by Domain Decomposition Method"
Advisor: Professor An-Lu Ren

Honors:

- Nominated to Sigma Xi, the Scientific Research Society, in 2003.
- 2003 Sigma Xi Award for Excellence in Research.

Publications and Conferences

Invited Talks:

1. Seminar speaker. School of Mathematics, Institute for Advanced Study, Princeton, NJ, December 6, 2002.
2. Invited speaker. DOE/NSF Workshop on Predictability of Complex Phenomena, hosted by Los Alamos National Laboratory, Santa Fe, NM, December 16-18, 2002.
3. Seminar speaker. "Predictability and Uncertainty in Large-Scale Simulations", CSIRO, Manufacturing and Infrastructure Technology, Highett, Victoria, Australia, June 6, 2003.

Journal Publications:

1. D. Xiu and G.E. Karniadakis, "A Semi-Lagrangian High-Order Method for Navier-Stokes Equations", *Journal of Computational Physics*, Vol. 172, 658-684, 2001.
2. D. Xiu and G.E. Karniadakis, "Modeling Uncertainty in Flow Simulations via Generalized Polynomial Chaos", *Journal of Computational Physics*, Vol. 187, 137-167, 2003.
3. D. Xiu and G.E. Karniadakis, "The Wiener-Askey Polynomial Chaos for Stochastic Differential Equations", *SIAM Journal on Scientific Computing*, Vol. 24, 619-644, 2002.
4. D. Xiu and G.E. Karniadakis, "Modeling Uncertainty in Steady State Diffusion Problems via Generalized Polynomial Chaos", *Computer Methods in Applied Mechanics and Engineering*, Vol. 191, 4927-4948, 2002.
5. D. Xiu, D. Lucor, C.-H. Su and G.E. Karniadakis, "Stochastic Modeling of Flow-Structure Interactions using Generalized Polynomial Chaos", *Journal of Fluids Engineering*, Vol. 124, 51-59, 2002.
6. J. Xu, D. Xiu and G.E. Karniadakis, "A Semi-Lagrangian Method for Turbulence Simulations Using Mixed Spectral Discretizations", *Journal of Scientific Computing*, Vol. 17, 585-597, 2002.
7. D. Lucor, D. Xiu, C.-H. Su and G.E. Karniadakis, "Predictability and Uncertainty in CFD", *International Journal for Numerical Methods in Fluids*, 2003 (in press).
8. D. Xiu and G.E. Karniadakis, "A New Stochastic Approach to Transient Heat Conduction Modeling with Uncertainty", *International Journal of Heat and Mass Transfer*, Vol. 46, 4681-4693, 2003.
9. D. Xiu and G.E. Karniadakis, "On the Well-posedness of Generalized Polynomial Chaos Expansions for the Stochastic Diffusion Equation", *SIAM Journal of Numerical Analysis*, 2003 (under review).

10. D. Xiu and G.E. Karniadakis, "Supersensitivity Due to Uncertain Boundary Conditions", *International Journal for Numerical Methods in Engineering*, 2003 (under review).
11. X. Wan, D. Xiu and G.E. Karniadakis, "Stochastic Solutions for the Two-dimensional Advection-Diffusion Equation", *SIAM Journal of Scientific Computing*, 2003 (under review).

Conference Proceedings:

1. D. Xiu, D. Lucor, M. Jardak, C.-H. Su and G.E. Karniadakis, "Polynomial Chaos Solutions of Fluid Dynamics with Applications", Proceedings of Stochastic Numerics Conference 2001, ETH Zurich, Switzerland, February 2001.
2. D. Xiu, D. Lucor and G.E. Karniadakis, "Modeling Uncertainty in Flow-structure Interactions", Computational Fluid and Solid Mechanics, Proceedings of the First MIT Conference on Computational Fluid and Solid Mechanics, Cambridge, MA, June 2001. Edited by K.J. Bathe, Vol. 2, pp.1420-1423, Elsevier Press, 2001.
3. D. Xiu and G.E. Karniadakis, "Modeling Uncertainty of Elliptic Partial Differential Equations via Generalized Polynomial Chaos", Proceedings of the 5th ASCE Engineering Mechanics Division Conference, Columbia University, New York City, June 2002.
4. D. Xiu and G.E. Karniadakis, "Uncertainty Modeling of Burgers' Equation by Generalized Polynomial Chaos", Computational Stochastic Mechanics, Proceedings of the 4th International Conference on Computational Stochastic Mechanics, Corfu, Greece, June 2002. Edited by P.D. Spanos and G. Deodatis, pp.655-661, Millpress Rotterdam, 2003.
5. D. Xiu, D. Lucor, C.-H. Su and G.E. Karniadakis, "Performance Evaluation of Generalized Polynomial Chaos", Computational Science – ICCS 2003, LNCS 2660, Proceedings of the 2003 International Conference on Computational Science, Melbourne, Australia, June 2003. Edited by P.M.A. Sloot et al, Vol. 4, pp.346–354, Springer-Verlag, 2003.

Conference Abstracts:

1. D. Xiu, R.M. Kirby and G.E. Karniadakis, "A Semi-Lagrangian Spectral/hp Element Method for Advection-Diffusion", Presented at Finite Element in Flow Problems 2000, Austin, Texas, April 30-May 4, 2000.
2. D. Xiu and G.E. Karniadakis, "A Semi-Lagrangian Method for DNS with Large Time-Stepping", Presented at the 53rd Annual Meeting of the American Physics Society's (APS) Division of Fluid Dynamics, Washington D.C., November 19-21, 2000.
3. D. Xiu and G.E. Karniadakis, "A Semi-Lagrangian Spectral/hp Element Method for the Navier-Stokes Equations", Presented at the International Conference on Spectral and High Order Methods 2001 (ICOSAHOM-01), Uppsala University, Sweden, June 11-15, 2001.
4. D. Lucor, D. Xiu, C.-H. Su and G.E. Karniadakis, "Spectral Representations of Uncertainty in Simulations: Algorithms and Applications", Presented at the International Conference on Spectral and High Order Methods 2001 (ICOSAHOM-01), Uppsala University, Sweden, June 11-15, 2001.
5. D. Xiu and G.E. Karniadakis, "Modeling Uncertainty in Navier-Stokes Equations via Polynomial Chaos", Presented at the 6th U.S. National Congress on Computational Mechanics (USNCCM), Dearborn, MI, July 31-August 4, 2001.
6. D. Xiu and G.E. Karniadakis, "Modeling Uncertainty in CFD via Generalized Polynomial Chaos", Presented at the 54th Annual Meeting of the American Physics Society's (APS) Division of Fluid Dynamics, San Diego, CA, November 18-20, 2001.
7. D. Xiu and G.E. Karniadakis, "Modeling Uncertainty via Generalized Polynomial Chaos", Presented at the 2002 SIAM Conference on Optimization, Toronto, Canada, May 20-22, 2002.
8. D. Xiu and G.E. Karniadakis, "Modeling Uncertainty by Generalized Polynomial

Chaos”, Presented at the SIAM 50th Anniversary and 2002 Annual Meeting, Philadelphia, July 8-12 2002.

9. S. Dong, D. Xiu and G.E. Karniadakis, “Semi-Lagrangian Method for Turbulence Simulation”, Presented at the SIAM Conference on Computational Science and Engineering, San Diego, CA, February 10-13, 2003.
10. S. Sherwin and D. Xiu, “Sub-stepping and Semi-Lagrangian Formulations of the Spectral/hp Element Navier-Stokes Equations”, Presented at the SIAM Conference on Computational Science and Engineering, San Diego, CA, February 10-13, 2003.
11. D. Xiu and D.M. Tartakovsky, “Generalized Polynomial Chaos and Random Domain Decomposition”, Presented at the NSF workshop on Applications of Modern Tools of Mathematics and Physics to Subsurface Hydrology, Purdue University, West Lafayette, IN, August 11-15, 2003.

Acknowledgments

Finally, my journey as a student has come to an end. As I look back to the past, while waiting for what the future will bring, I realize that I have many individuals to thank to.

First of all, my gratitude goes to Professor George Em Karniadakis, my Ph.D. thesis advisor at the Division of Applied Mathematics of Brown University. During the years I spent at Brown, he has been an understanding mentor and a supportive advisor. His vision in science and insight in physics are unparalleled, and have been vital to the completion of this thesis. I am truly grateful to the encouragement, support and opportunities he has provided. His guidance, which is often beyond the scope of academia, has been an invaluable asset to me, and is the one I will always treasure.

Secondly, I would like to express my thanks to two of my former advisors. Professor Hossein Haj-Hariri was my MS thesis advisor in Mechanical Engineering of the University of Virginia. It was him who taught me how to understand mathematics from a physics point of view, and how to associate virtually any concept in fluid dynamics with concrete examples. Professor An-Lu Ren was my undergraduate advisor in the Mechanics Department of Zhejiang University in China. He introduced me to the field of CFD (Computational Fluid Dynamics), and taught me how to understand computational results by literally examining the numbers on the screen in the early days of computers when good visualization softwares were scarce.

Thirdly, I would like to express my appreciation to my thesis readers, Professor Roger Ghanem of Johns Hopkins University, Professor James Glimm of SUNY at Stony Brook, and Professor David Gottlieb of Brown University, for sparing their precious time and providing valuable comments on the thesis. I am also privileged to have had the opportunity to interact with many of the professors, students and staff members here in the Division. Such interactions have made my life at Brown, both academic life and social life, much more enjoyable. Among them, an important part takes place within the CRUNCH group. I thank the help I received from several former CRUNCH members, Dr. Spencer Sherwin, Dr. Tim Warburton, Dr. George Karamanos, Dr. Mike Kirby, and Dr. Xia Ma. I would also like to acknowledge the current members, whom I frequently interacted with

and learned valuable lessons from.

Last but not the least, my utmost gratitude goes to my family members, for their unconditionally support throughout the years. My parents, Richen Xiu and Yuhe Gu, have guided me to the doorstep of science, and have always believed in me and been patient with my progress. On the other side of the family, my loving wife Yvette Shen and her mother Meela Shen, have supported me during the Ph.D. years in every possible way, and made my life a much better and a much more comfortable one. My special thanks also go to my beloved sister, Angela Xiu, and her loving family. My journey to a Ph.D. degree would not have been possible without the support of my family.

Contents

Acknowledgments	ix
1 Introduction	1
1.1 Illustrative Examples	2
1.2 Review of Probabilistic Methods	5
1.2.1 Statistical Methods	5
1.2.2 Non-statistical Methods	6
1.3 Objective and Outline	7
2 Orthogonal Polynomials and Generalized Polynomial Chaos	10
2.1 The Askey Scheme of Orthogonal Polynomials	10
2.1.1 Orthogonal Polynomials	11
2.1.2 The Askey Scheme	12
2.2 Representation of Stochastic Processes	14
2.2.1 Karhunen-Loeve Expansion	14
2.2.2 Wiener-Hermite Expansion	15
2.3 Generalized Polynomial Chaos	17
2.3.1 Construction and Properties	17
2.3.2 Representation of Random Variables	19
2.3.3 Representation of Random Processes	23
2.3.4 Solutions of Stochastic Equations	24
2.3.5 Application to Stochastic Ordinary Differential Equations	25

3	Elliptic Equations	36
3.1	Stochastic Formulations and a Block-Jacobi Iterative Algorithm	37
3.2	Numerical Examples	39
3.2.1	One-Dimensional Model Problem	39
3.2.2	Two-Dimensional Model Problem	43
3.2.3	Random Heat Conduction in a Grooved Channel	52
3.3	Problems with Random Boundary: Roughness	54
4	Parabolic Equations	57
4.1	Stochastic Formulation with Uncertain Diffusivity	57
4.2	Well-posedness of Generalized Polynomial Chaos Expansion	58
4.2.1	Gaussian Input and Hermite-chaos	62
4.2.2	Beta Input and Jacobi-chaos	64
4.2.3	Gamma Input and Laguerre-chaos	66
4.2.4	Discussion	69
4.3	Applications to Transient Heat Conduction	70
4.3.1	Algorithm	70
4.3.2	Random Heat Conduction in an Electronic Chip	74
5	Advection-Diffusion Equation	83
5.1	Linear Advection-Diffusion	83
5.1.1	Model problem: convergence	84
5.1.2	Results with two-dimensional ‘truncated’ Gaussian input	92
5.2	Nonlinear Advection-Diffusion: Burgers’ Equation	96
5.2.1	Deterministic Supersensitivity	97
5.2.2	Stochastic Supersensitivity	101
6	Incompressible Navier-Stokes Equations	116
6.1	Stochastic Formulation	116
6.1.1	Governing Equations	116
6.1.2	Numerical Formulation	117

6.2	Microchannel Flow	119
6.2.1	Uniform Boundary Conditions	119
6.2.2	Non-uniform Boundary Conditions	121
6.3	Flow Past a Circular Cylinder	126
6.3.1	Onset of instability	126
6.3.2	Vortex Shedding	128
6.4	Flow in a Grooved Channel	129
7	Summary	138
A	Some Important Orthogonal Polynomials in Askey-scheme	141
A.1	Continuous Polynomials	142
A.1.1	Hermite Polynomial $H_n(x)$ and Gaussian Distribution	142
A.1.2	Laguerre Polynomial $L_n^{(\alpha)}(x)$ and Gamma Distribution	142
A.1.3	Jacobi Polynomial $P_n^{(\alpha, \beta)}(x)$ and Beta Distribution	143
A.2	Discrete Polynomials	144
A.2.1	Charlier Polynomial $C_n(x; a)$ and Poisson Distribution	144
A.2.2	Krawtchouk Polynomial $K_n(x; p, N)$ and Binomial Distribution . . .	145
A.2.3	Meixner Polynomial $M_n(x; \beta, c)$ and Negative Binomial Distribution	146
A.2.4	Hahn Polynomial $Q_n(x; \alpha, \beta, N)$ and Hypergeometric Distribution .	147
B	Estimation of the Largest Zero of Hermite Polynomials	149
C	The Truncated Gaussian Model $G(\alpha, \beta)$	151
D	Numerical Results for Supersensitivity of Burgers' Equation	154
D.1	Numerical Results for Deterministic Supersensitivity	154
D.2	Numerical Results for Stochastic Supersensitivity	154

List of Figures

1.1	Solution profile of Burgers' equation subject to perturbation of the left boundary condition.	3
2.1	The Askey scheme of hypergeometric orthogonal polynomials.	14
2.2	Approximation of exponential distribution with Hermite-chaos; Left: The expansion coefficients, Right: The PDF of different orders of approximations.	21
2.3	PDF of approximations of beta distributions by Hermite-chaos; Left: $\alpha = \beta = 0$, the uniform distribution, Right: $\alpha = 2, \beta = 0$	22
2.4	Solution with Gaussian random input by 4th-order Hermite-chaos; Left: Solution of each random mode, Right: Error convergence of the mean and the variance.	27
2.5	Solution with Gamma random input by 4th-order Laguerre-chaos; Left: Solution of each mode ($\alpha = 0$: exponential distribution), Right: Error convergence of the mean and the variance with different α	28
2.6	Solution with Beta random input by 4th-order Jacobi-chaos; Left: Solution of each mode ($\alpha = \beta = 0$: Legendre-chaos), Right: Error convergence of the mean and the variance with different α and β	29
2.7	Solution with Poisson random input by 4th-order Charlier-chaos; Left: Solution of each mode ($\lambda = 1$), Right: Error convergence of the mean and the variance with different λ	30

2.8	Solution with binomial random input by 4th-order Krawtchouk-chaos; Left: Solution of each mode ($p = 0.5, N = 5$), Right: Error convergence of the mean and the variance with different p and N	31
2.9	Solution with negative binomial random input by 4th-order Meixner-chaos; Left: Solution of each mode ($\beta = 1, c = 0.5$), Right: Error convergence of the mean and the variance with different β and c	32
2.10	Solution with hypergeometric random input by 4th-order Hahn-chaos; Left: Solution of each mode ($\alpha = \beta = 5, N = 4$), Right: Error convergence of the mean and the variance with different α, β and N	33
2.11	Error convergence of the mean solution of the Laguerre-chaos and Hermite-chaos to stochastic ODE with random input of the exponential distribution	34
3.1	Convergence of Jacobi-chaos for the one-dimensional model problem.	41
3.2	Convergence of Hermite-chaos for the one-dimensional model problem.	42
3.3	Convergence of Charlier-chaos for the one-dimensional model problem.	42
3.4	Convergence of Krawtchouk-chaos for the one-dimensional model problem.	43
3.5	Eigenvalues of KL decomposition with Bessel correlation function (3.20), $b = 20$	46
3.6	Eigenfunctions of the KL decomposition with the Bessel correlation function (3.20), $b = 20$; Left: first eigenfunction, Right: second eigenfunction. (Dashed lines denote negative values.)	46
3.7	Eigenfunctions of the KL decomposition with the Bessel correlation function (3.20), $b = 20$; Left: third eigenfunction, Right: fourth eigenfunction. (Dashed lines denote negative values.)	47
3.8	Two-dimensional model problem: uniform random distribution and Legendre-chaos; Left: Mean solution along the horizontal centerline, Right: Close-up view.	48
3.9	Two-dimensional model problem: uniform random distribution and Legendre-chaos; Left: Variance along the horizontal centerline, Right: Close-up view.	48

3.10	Two-dimensional model problem: Gaussian random distribution and Hermite-chaos; Left: Mean solution along the horizontal centerline, Right: Close-up view.	49
3.11	Two-dimensional model problem: Gaussian random distribution and Hermite-chaos; Left: Variance along the horizontal centerline, Right: Close-up view.	50
3.12	Two-dimensional model problem: Poisson random distribution and Charlier-chaos; Left: Mean solution along the horizontal centerline, Right: Close-up view.	50
3.13	Two-dimensional model problem: Poisson random distribution and Charlier-chaos; Left: Variance along the horizontal centerline, Right: Close-up view.	51
3.14	Two-dimensional model problem: binomial random distribution and Krawtchouk-chaos; Left: Mean solution along the horizontal centerline, Right: Close-up view.	51
3.15	Two-dimensional model problem: binomial random distribution and Krawtchouk-chaos; Left: Variance along the horizontal centerline, Right: Close-up view.	52
3.16	Schematic of the domain of the grooved channel	53
3.17	Standard deviations of heat conduction in the grooved channel; Left: solution subject to random diffusivity only; Right: solution subject to random diffusivity and random boundary conditions.	54
3.18	Schematic of the mapping of a uncertain domain.	56
3.19	Mean square error convergence for a model problem with uncertain boundary.	56
4.1	Critical expansion order (N) versus σ for the well-posedness of Hermite-chaos ($\mu = 1$).	65
4.2	Critical expansion order (N) versus σ for the well-posedness of Laguerre-chaos ($\mu = 1, \alpha = 0$).	68
4.3	Schematic of the domain of the chip geometry. It consists of 16 spectral elements of order 6 th (7 points).	75
4.4	Eigenmodes of the correlation field. Left: the first eigenmode; Right: the second eigenmode.	75

4.5	Contours of temperature distribution in the electronic chip at steady state (case 1). Left: mean field; Right: standard deviation.	76
4.6	Temperature evolution at reference points (case 1). Left: mean temperature; Right: COV (coefficient of variance).	77
4.7	Time evolution of cross-correlation coefficients between reference point A and other points (case 1).	77
4.8	Contours of temperature distribution in the electronic chip (unsteady state at $t = 1$, case 2). Left: mean field; Right: standard deviation.	77
4.9	Temperature evolution at reference points (case 2: unsteady problem). Left: mean temperature; Right: COV (coefficient of variance).	78
4.10	Time evolution of cross-correlation coefficients between reference point A and other points (case 2: unsteady problem).	78
4.11	Stochastic solution at reference points (case 2: unsteady problem).	79
4.12	Comparison of results obtained by Monte Carlo simulation and generalized polynomial chaos expansion. Left: evolution of cross-correlation coefficients at reference points for case 1 (20,00 realizations for MCS); Right: evolution of COVs at reference points for case 2 (150,000 realizations for MCS).	80
4.13	Temperature COV evolution at reference points. Left: random capacity only; Right: random conductivity only.	81
4.14	Evolution of cross-correlation coefficient between reference point A and the other points. Left: random capacity only; Right: random conductivity only.	82
5.1	L^∞ error of Legendre-chaos with uniform random input at $T = 3\pi$	85
5.2	L^∞ error of Jacobi-chaos with $Be^{(10,10)}(-1, 1)$ random input at $T = 3\pi$	86
5.3	L^∞ error of Hermite-chaos with Gaussian random input at $T = 3\pi$	86
5.4	PDF of the peak solution at $T = \pi$ with Gaussian input and Hermite-chaos expansion.	87
5.5	L^∞ error of Jacobi-chaos with truncated Gaussian $G^{(10,10)}$ random input at $T = 3\pi$	88
5.6	PDF of the peak solution at $T = \pi$ with $G^{(10,10)}$ input and Jacobi-chaos expansion.	89

5.7	Error bars of the evolution of the peak solution with $G^{(10,10)}$ input and Jacobi-chaos expansion. The circles represent the stochastic mean solution and the dotted line the deterministic solution.	89
5.8	Jacobi-chaos solution with $G^{(10,10)}$ random input at $T = 0.5\pi$. Left: mean solution; Right: variance.	90
5.9	Jacobi-chaos solution $G^{(10,10)}$ random input at $T = \pi$. Left: mean solution; Right: variance.	90
5.10	Jacobi-chaos solution $G^{(10,10)}$ random input at $T = 1.5\pi$. Left: mean solution; Right: variance.	91
5.11	Jacobi-chaos solution $G^{(10,10)}$ random input at $T = 2\pi$. Left: mean solution; Right: variance.	91
5.12	Jacobi-chaos solution $G^{(10,10)}$ random input at $T = 2.5\pi$. Left: mean solution; Right: variance.	91
5.13	Jacobi-chaos solution $G^{(10,10)}$ random input at $T = 3\pi$. Left: mean solution; Right: variance.	92
5.14	Error bars of the evolution of the peak solution with two-dimensional 'truncated' Gaussian input and Jacobi-chaos expansion. The circles represent the stochastic mean solution and the dotted line the deterministic solution.	93
5.15	Jacobi-chaos solution with 2D-Gaussian random input at $T = 0.5\pi$. Left: mean solution; Right: variance.	93
5.16	Jacobi-chaos solution of 2D-Gaussian random input at $T = \pi$. Left: mean solution; Right: variance.	94
5.17	Jacobi-chaos solution of 2D-Gaussian random input at $T = 1.5\pi$. Left: mean solution; Right: variance.	94
5.18	Jacobi-chaos solution of 2D-Gaussian random input at $T = 2\pi$. Left: mean solution; Right: variance.	94
5.19	Jacobi-chaos solution of 2D-Gaussian random input at $T = 2.5\pi$. Left: mean solution; Right: variance.	95
5.20	Jacobi-chaos solution of 2D-Gaussian random input at $T = 3\pi$. Left: mean solution; Right: variance.	95

5.21	Stochastic solutions by Legendre-chaos with $\delta \sim U(0, 0.1)$ and $\nu = 0.05$. The upper and lower bounds are the deterministic solutions corresponding to the bounds of the random inputs, $\delta = 0.1$ and $\delta = 0$, respectively.	105
5.22	Stochastic solutions by Legendre-chaos with $\delta \sim U(0, 0.1)$ and $\nu = 0.1$. The upper and lower bounds are the deterministic solutions corresponding to the bounds of the random inputs, $\delta = 0.1$ and $\delta = 0$, respectively.	105
5.23	Probability density functions at various locations for $\delta \sim U(0, 0.1)$ and $\nu = 0.05$. Gibb's oscillations are present at $x = 0.6$ and 0.5	107
5.24	Probability density functions at various locations for $\delta \sim U(0, 0.1)$ and $\nu = 0.1$	107
5.25	Probability density functions at $x = 0.6$ and $x = 0.9$ for $\delta \sim U(0, 0.1)$ and $\nu = 0.05$ by Monte Carlo simulation and Legendre-chaos expansion. (The oscillations at $x = 0.9$ are due to Gibb's phenomenon.)	108
5.26	Probability density functions at $x = 0.7$ and $x = 0.8$ for $\delta \sim U(0, 0.1)$ and $\nu = 0.05$ by Monte Carlo simulation and Legendre-chaos expansion.	108
5.27	Stochastic solution by Jacobi-chaos ($\alpha = \beta = 10$) with $\delta \sim G^{(10,10)}(0, 0.1)$ and $\nu = 0.05$. The upper and lower bounds are the deterministic solutions corresponding to the bounds of the random inputs $\delta = 0.1$ and $\delta = 0$, respectively.	111
5.28	Stochastic solution by Jacobi-chaos ($\alpha = \beta = 10$) with $\delta \sim G^{(10,10)}(0, 0.1)$ and $\nu = 0.1$. The upper and lower bounds are the deterministic solutions corresponding to the bounds of the random inputs $\delta = 0.1$ and $\delta = 0$, respectively.	111
5.29	Probability density functions at various locations ($\delta \sim G^{(10,10)}(0, 0.1)$ and $\nu = 0.05$).	112
5.30	Probability density functions at various locations ($\delta \sim G^{(10,10)}(0, 0.1)$ and $\nu = 0.1$).	112
5.31	Probability density functions with $\nu = 0.05$, $\delta \sim G^{(10,10)}(0, 0.1)$. Left: $x = 0.6$, Right: $x = 0.7$	113

5.32	Probability density functions with $\nu = 0.05$, $\delta \sim G^{(10,10)}(0, 0.1)$. Left: $x = 0.8$, Right: $x = 0.9$	113
5.33	Probability density functions with $\nu = 0.1$, $\delta \sim G^{(10,10)}(0, 0.1)$. Left: $x = 0.6$, Right: $x = 0.7$	113
5.34	Probability density functions with $\nu = 0.1$, $\delta \sim G^{(10,10)}(0, 0.1)$. Left: $x = 0.8$, Right: $x = 0.9$	114
6.1	Schematic of the domain for pressure-driven channel flow with random boundary conditions.	119
6.2	Solution of the pressure-driven channel with uniform Gaussian random boundary conditions; Left: the solution profile, Right: development of random modes of v -velocity with nonzero initial conditions.	120
6.3	Deviation of mean solution from a parabolic profile in pressure-driven channel flow with partially-correlated random boundary conditions at the lower wall; Upper: u -velocity, Lower: v -velocity.	121
6.4	Contours of rms of u -velocity (upper) and v -velocity (lower).	122
6.5	Monte Carlo (MC) and Hermite-Chaos (HC) solution of the mean velocities along the centerline of the channel; Left: u -velocity, Right: v -velocity.	123
6.6	Hermite-Chaos solution of the mean velocities along the centerline of the channel with different σ ; Left: u -velocity, Right: v -velocity.	123
6.7	Chaos solution of mean velocities along the centerline of the channel with different types of input processes; Left: u -velocity, Right: v -velocity.	124
6.8	Chaos solution of variance along the centerline of the channel with different types of input processes; Left: variance of u -velocity, Right: variance of v -velocity.	125
6.9	Monte Carlo (MC) and Legendre-Chaos solution of the mean velocities along the centerline of the channel with uniform stochastic inputs; Left: u -velocity, Right: v -velocity.	125
6.10	Schematic of the domain for flow past an elastically mounted circular cylinder.	126

6.11	Time history of mean pressure at the rear stagnation point at $Re = 40$ (Gaussian perturbation with $\sigma = 0.1$); Left: The time history, Right: Close-up view.	127
6.12	Time history of mean pressure at the rear stagnation point at $Re = 35$; Left: The time history, Right: Close-up view.	128
6.13	Pressure signal of cylinder flow with non-uniform Gaussian random inflow. Upper: High modes. Lower: Zero mode (mean).	129
6.14	Frequency spectrum for the deterministic (high peak) and stochastic simulation (low peak).	130
6.15	Instantaneous profiles of the two velocity components along the centerline (in the wake) for the deterministic and the mean stochastic solution.	130
6.16	Instantaneous vorticity field : Upper - Deterministic solution with uniform inflow; Lower - Mean solution with non-uniform Gaussian random inflow.	131
6.17	Instantaneous contours of <i>rms</i> of vorticity field with non-uniform Gaussian random inflow.	131
6.18	Flow in a grooved channel: the computational mesh. (The history point is shown as a solid dot.)	133
6.19	Evolution of mean velocity field at the history point (solid lines), with the reference deterministic results shown in dashed lines. $r = 220$ and $Re = 238.6$. Left: u -velocity, Right: v -velocity.	135
6.20	Mean velocity fields at $t = 5,000$. $r = 220$ and $Re = 238.6$. Left: u -velocity, Right: v -velocity.	135
6.21	Standard deviation of velocity fields at $t = 5,000$. $r = 220$ and $Re = 238.6$. Left: u -velocity, Right: v -velocity.	136
C.1	Approximated Gaussian random variables by Jacobi-chaos; Left: $\alpha = \beta = 0$, Right: $\alpha = \beta = 2$	152
C.2	Approximated Gaussian random variables by Jacobi-chaos; Left: $\alpha = \beta = 4$, Right: $\alpha = \beta = 6$	152
C.3	Approximated Gaussian random variables by Jacobi-chaos; Left: $\alpha = \beta = 8$, Right: $\alpha = \beta = 10$	153

List of Tables

1.1	Stochastic solutions and computational cost of different methods for Burgers' equation with uncertain boundary condition. (One unit of cost corresponds to the cost of one deterministic simulation.)	4
2.1	The correspondence between the type of generalized polynomial chaos and their underlying random variables ($N \geq 0$ is a finite integer).	19
2.2	Error convergence of the mean solution by Monte-Carlo simulation: N is the number of realizations and $\varepsilon_{\text{mean}}$ is the error of mean solution defined in (2.46); Random input has exponential distribution.	34
4.1	Coefficients in the mixed explicit-implicit integration (4.37) (see [63], chapter 8).	73
5.1	Locations of transition layer of Burgers' equation with $\nu = 0.1$ subject to deterministic perturbation on boundary condition. z_{as} is the asymptotic estimate from (5.15), z_{GK} is the numerical result from [33], z is the present direct numerical computation, and z_{ex} is the numerical solution from exact formula (5.11).	100
5.2	Locations of transition layer of Burgers' equation with $\nu = 0.05$ subject to deterministic perturbation on boundary condition. z_{as} is the asymptotic estimate from (5.15), z_{GK} is the numerical result from [33], z is the present direct numerical computation, and z_{ex} is the numerical solution from exact formula (5.11).	100

5.3	The mean locations (\bar{z}) of the transition layer and their corresponding standard deviations (σ_z) subject to uniform random perturbation $\delta \sim U(0, \epsilon)$ on the boundary condition.	104
5.4	The mean location of the transition layer (\bar{z}) and its standard deviation (σ_z) from Monte Carlo simulations. n is the number of realizations, $\delta \sim U(0, 0.1)$ and $\nu = 0.05$. Also shown are the converged Legendre-chaos solutions for comparison.	107
5.5	The mean location of the transition layer (\bar{z}) and its standard deviation (σ_z) from the perturbation method. k is the order of the perturbative expansion, $\delta \sim U(0, 0.1)$ and $\nu = 0.05$. Also shown are the converged results from Legendre-chaos.	109
5.6	The mean location of the transition layer (\bar{z}) and its standard deviation (σ_z) with truncated Gaussian random inputs $\delta \sim G^{(10,10)}(0, 0.1)$, for $\nu = 0.05$ and $\nu = 0.1$	110
6.1	Reynolds number (Re) and the modified Reynolds number (r) in a grooved channel (Equation (6.19) and (6.20)).	133
6.2	Comparison of the least stable mode ($\lambda = \sigma + i2\pi f$) of the Orr-Sommerfeld equation for plain Poiseuille flow.	137
C.1	Approximating Gaussian via Jacobi-chaos: expansion coefficients y_k and errors. (ϵ_2 is the error in variance; ϵ_4 is the error in kurtosis. There is no error in mean.) $y_k = 0$ when k is even.	153
D.1	The locations of the transition layer at $\nu = 0.05$ with different values of perturbation δ . N is the order of spectral elements, and the dash “—” indicates the number there is the same as the one above it. Also shown are the results from exact formula.	155
D.2	The locations of the transition layer at $\nu = 0.1$ with different values of perturbation δ . N is the order of spectral elements, and the dash “—” indicates the number there is the same as the one above it. Also shown are the results from exact formula.	155

D.3 The stochastic solution of the locations of the transition layer at $\nu = 0.05$ listed in form of (\bar{z}, σ_z) , where \bar{z} is the mean location and σ_z its standard deviation. M is the order of Legendre-chaos; N is the order of spectral elements. The dash “—” indicates the number there is the same as the one above it. The reference values obtained by $M = 10$ and $N = 22$ are (0.81390488, 0.41403291). 156

Chapter 1

Introduction

During the last four decades, computer simulations of physical processes have been increasingly used in scientific research and in the analysis and design of engineering systems. Because of the impact that simulation predictions can have, the credibility of computational results is of great concern, and there has been an intense interest in verification and validation of large-scale simulations and in uncertainty quantification [1, 45, 46, 47, 53, 87, 93, 94, 107, 108, 137].

Characterization of uncertainty is a complex subject in general, but it can be roughly classified as numerical uncertainty and physical uncertainty. The former includes spatiotemporal discretization errors, errors in numerical boundary conditions (e.g., outflow), errors in solvers or geometry description, etc. On the other hand, physical uncertainty includes errors due to unknown boundary and initial conditions, imprecise transport coefficients or interaction terms, insufficient knowledge of the geometry, approximate constitutive laws, etc. There are also coupled problems involving source and interaction terms and are difficult to simulate even deterministically, so providing error bars for such solutions is even more difficult.

With regards to numerical uncertainty, accuracy tests and error control have been employed in simulations for the modern discretizations. High-order, high-resolution numerical methods are used in increasingly more applications to reduce the discretization errors. Also, *a posteriori* error bounds and estimates are available in some cases for better error control. With regards to physical uncertainty, it is only recently that a systematic

effort has been made to address it. The common practice in engineering is to analyze systems based on deterministic mathematical models with precisely defined input data. However, such ideal conditions are rarely encountered in practice, and there is a need to address physical uncertainty in real systems. The purpose of uncertainty quantification is to identify and quantify each source of uncertainty and to assess their integrated effect on the simulation results. Because incomplete knowledge of the properties of complex systems often leads to a probabilistic description of each source of uncertainty, uncertainty quantification is naturally a concept of stochastic modeling, and there has been a growing interest in developing probabilistic methods.

1.1 Illustrative Examples

In this section, we present two examples to illustrate the effect of uncertainty on physical systems. First, we demonstrate, through the viscous Burgers' equation, that a small perturbation on the boundary condition can lead to a much larger response in the solution. Next, we show, via a simple model of hyperbolic system, that introducing randomness into the system could change the mathematical nature of the governing equation.

Consider a one-dimensional viscous Burgers' equation

$$\begin{cases} u_t + uu_x = \nu u_{xx}, & x \in [-1, 1], \\ u(-1) = 1 + \delta, & u(1) = -1, \end{cases} \quad (1.1)$$

where $\delta > 0$ is a small perturbation to the left boundary condition ($x = -1$) and $\nu > 0$ is the viscosity. The solution has a transition layer, which is a region of rapid variation and extends over a distance $O(\nu)$ as $\nu \downarrow 0$. The location of the transition layer z , defined as the zero of the solution profile $u(z) = 0$, varies with time, and its eventual location at steady state is sensitive to the boundary data.

In figure 1.1, we show two solutions with viscosity $\nu = 0.05$, computed by high-order spectral/*hp* method ([63]) with five non-uniform meshes as shown in the figure. The dashed line corresponds to the solution with no perturbation ($\delta = 0$), and the solid line to a small *deterministic* perturbation ($\delta = 0.01$). We observe that with a perturbation

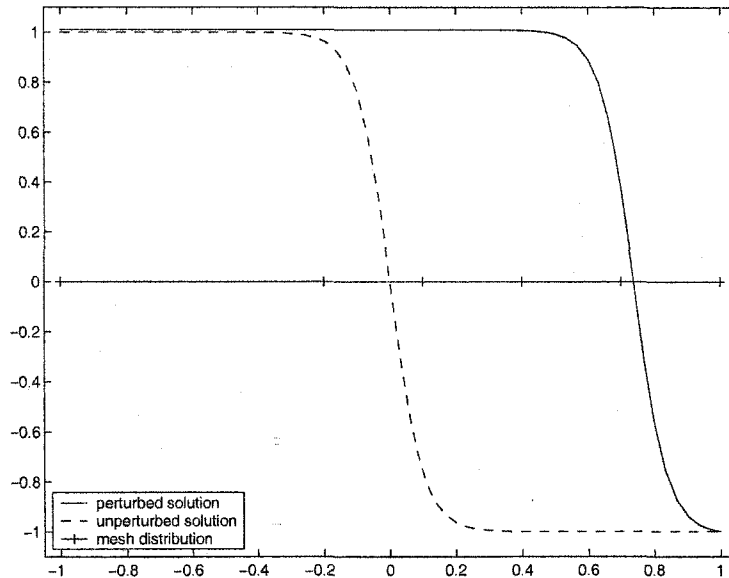


Figure 1.1: Solution profile of Burgers' equation subject to perturbation of the left boundary condition.

as small as 0.01, the location of the transition layer moves from $z = 0$ (dashed line) to $z = 0.73746$ (solid line), i.e. by a $O(1)$ change. This example shows the impact a small perturbation on input can make.

If we assume that the perturbation on the left-side boundary condition is uncertain and model it as a random number, then the system (1.1) becomes stochastic. In table 1.1, the mean location of the transition layer (\bar{z}) and its standard deviation (σ_z) are shown. They are obtained by assuming $\delta \in (0, 0.1)$ is a uniform random number between $(0, 0.1)$ and $\nu = 0.05$. The results of several methods are shown, along with their computational cost normalized by the cost of one deterministic simulation. Specifically, interval analysis deals with the maximal output bounds, and is straightforward to apply to this problem¹. However, it does not provide any statistical information of the solution. The results from perturbation methods are noticeably different from the accurate solution obtained by Monte Carlo simulation with 10,000 realizations. In addition, the fourth-order perturbation method does not yield any improvement over the first-order method. This suggests

¹For this problem, we only need to conduct one simulation corresponding to the maximum input of $\delta = 0.1$ to determine the maximum output. In general, however, such monotonic dependence between input and output does not exist, and a systematic search in the input range is needed to locate the maximum response.

Method	(\bar{z}, σ_z)	Cost (unit)
Interval analysis	N/A	≤ 2
First-order perturbation method	(0.823, 0.349)	~ 2
Fourth-order perturbation method	(0.824, 0.328)	~ 5
Fourth-order Legendre-chaos	(0.814, 0.414)	~ 5
Monte Carlo simulation	(0.814, 0.414)	$\sim 10,000$

Table 1.1: Stochastic solutions and computational cost of different methods for Burgers' equation with uncertain boundary condition. (One unit of cost corresponds to the cost of one deterministic simulation.)

that the perturbation method converges slowly, if at all. The Legendre-chaos method, one of the subsets of the generalized polynomial chaos, accurately resolves the solution statistics. At fourth-order, its cost is about the same as the fourth-order perturbation method and is *much less* than the Monte Carlo method. This illustrative example reveals the promise of generalized polynomial chaos for stochastic modeling, which is the focus of this thesis. (More details of computations of stochastic Burgers' equation can be found in section 5.2 of this thesis; see also [134].)

Dealing with noises in physical systems requires new formalism and effective tools to handle the mathematical complexity. The following example serves as a demonstration.

Consider a one-dimensional hyperbolic system,

$$\frac{\partial u}{\partial t} + \frac{\partial F(u)}{\partial x} = 0, \quad (1.2)$$

where

$$u = [u_1, u_2]^T, \quad F(u) = [u_2, \alpha^2 u_1], \quad \alpha \neq 0. \quad (1.3)$$

The Jacobian is

$$A(u) \equiv \frac{\partial F(u)}{\partial u} = \begin{bmatrix} 0 & 1 \\ \alpha^2 & 0 \end{bmatrix}. \quad (1.4)$$

This is a strongly hyperbolic system with eigenvalue $\lambda_{1,2} = \pm\alpha$. Now assume that the system is subject to random input and the flux takes the form $F(u) = [u_2(1 + \epsilon(\omega)), \alpha^2 u_1]$,

where $\epsilon(\omega)$ is a random variable. The stochastic Jacobian becomes

$$A(u) = \begin{bmatrix} 0 & 1 + \epsilon \\ \alpha^2 & 0 \end{bmatrix}. \quad (1.5)$$

The eigenvalues are $\lambda_{1,2}(\omega) = \alpha\sqrt{1 + \epsilon(\omega)}$. It is clear that the stochastic problem is weakly (strongly) hyperbolic if $\epsilon \geq -1$ ($\epsilon > -1$). Therefore, while the original deterministic problem is always hyperbolic, the stochastic problem is not whenever the random variable $\epsilon(\omega)$ has support within $(-\infty, -1)$, e.g. a Gaussian distribution.

This example shows that under stochastic assumptions, the properties of the governing equations may change and we need to pay extra attention in studying such problems.

1.2 Review of Probabilistic Methods

Many methods have been developed to solve stochastic systems. In this section, we briefly review the techniques that are more popular in engineering applications. Following [76], these methods can be broadly classified into two major categories: methods using a statistical approach and methods using a non-statistical approach.

1.2.1 Statistical Methods

The statistical approach includes Monte Carlo simulation, stratified sampling, Latin hypercube sampling, etc (cf. [30]). These methods involve sampling and estimation and in most cases are straightforward to apply. The accuracy of Monte Carlo method is not dependent on the dimensionality of the system but, rather, on the number of realizations used to characterize the system. For the interested reader, a wide range of literature describing the methodology, tools, and the applicability of the Monte Carlo methods is available [11, 24, 26, 30, 35, 49, 59, 103, 109, 115]. Since the accuracy of the sampling techniques depends on the sample size, in accordance with the ‘weak law of large number’, simulations can become prohibitively expensive, especially for the systems that are already complicated in the *deterministic* case. Also, it is not suited to assessing the low probability domain of the stochastic response, as a large number of realizations will be

required. To accelerate convergence, several techniques have been developed, for example, Latin Hypercube Sampling [80, 116], Quasi-Monte Carlo (QMC) method [31, 91, 92], Markov Chain Monte Carlo method (MCMC) [32, 44, 82], Response Surface method (RSM) [12, 13, 29, 102, 104, 113], etc. These methods can improve the efficiency of the brute-force Monte Carlo method. However, additional restrictions are imposed based on their specific designs and the applicability of these methods is limited.

Statistical methods will not be the focus of this thesis.

1.2.2 Non-statistical Methods

Recently, more research effort has been made in developing non-statistical methods. The most popular method is perturbation method, where a random field is expanded via Taylor series around its mean and truncated at certain order. Typically, at most second-order expansion is employed because the system of equations becomes extremely complicated beyond second-order. This approach, also called the ‘second moment analysis’ [75, 76, 77], has been used extensively in various fields [51, 52, 64, 74, 78, 121, 139]. An inherent limitation of perturbation methods is that the uncertainties cannot be too large, i.e., the deviations of the random fields cannot be too large compared with their mean values, e.g., typically less than 10%². Also, higher-order statistics are not readily available for second moment methods.

Another approach is based on the manipulation of the stochastic operators. Methods along this line of approach include Neumann expansion, which is based on the inverse of the stochastic operator in a Neumann series [114, 136, 138], and the weighted integral method [22, 23, 118, 119]. These methods have limitations on the type of model equations they can address, and they are also restricted to small uncertainties.

Another methodology of the non-statistical type is to ‘discretize’ directly a random field in the random space. Ghanem and Spanos pioneered a *polynomial chaos* expansion method and have successfully applied it to various problems in mechanics [43]. The polynomial chaos expansion is based on the homogeneous chaos theory of Wiener [124] and is

²Note that this requirement needs to be satisfied by not only the stochastic inputs, but also the stochastic outputs. This is especially difficult to verify *a priori* for nonlinear problems as small random inputs may result in large responses, as demonstrated by our example of Burgers’ equation in section 1.1.

essentially a spectral expansion of the random variables. It allows high-order representation and promises fast convergence; coupled with Karhunen-Loeve decomposition for the stochastic input [79] and Galerkin projection in the random space, it results in computationally tractable algorithms for large engineering systems [37, 38, 39, 41, 42, 43, 71, 73]. Other applications and analysis, including the limitation of Wiener-Hermite expansion, can be found in [2, 17, 54, 83, 84, 85, 98]. More recently, a theoretical framework of discretizing random fields via the finite element approach, i.e. piecewise polynomials, was proposed in [5, 6, 21].

The classical polynomial chaos expansion is based on the *Hermite* polynomials in terms of *Gaussian* random variables. Although, in theory it converges to any L_2 functionals in the random space [14], it achieves optimal convergence rate only for Gaussian and near Gaussian random fields [130], and does not readily apply to random fields with *discrete* distributions. A more general framework, called the ‘generalized polynomial chaos’ or the ‘Askey-chaos’, was proposed in [130], following the more fundamental work on stochastic theory [95, 111] and orthogonal polynomials [3, 65]. Here the polynomials are chosen from the hypergeometric polynomials of the Askey scheme [3], and the underlying random variables are not restricted to Gaussian random variables. Instead, the type of random variables are chosen according to the stochastic input, and the weighting function of the random input determines the type of orthogonal polynomials to be used. The convergence properties of different bases were studied in [130] and exponential convergence rate was demonstrated for model problems. Applications to stochastic ODE, PDE, Navier-Stokes and flow-structure interactions have been reported, along with convergence for model problems in [122, 129, 130, 131, 132, 134, 135]. More recently, another generalized polynomial chaos expansion based on wavelets was proposed in [72].

1.3 Objective and Outline

The objective of this thesis is to give a comprehensive introduction of the theory of generalized polynomial chaos and examine its properties. Various stochastic systems are to be considered, and the pros and cons of generalized polynomial chaos will be shown via these

applications.

In chapter 2, we review the fundamental theory of orthogonal polynomials, in particular, the Askey scheme of hypergeometric polynomials. After discussing the two popular representation techniques for stochastic processes, the Karhunen-Loeve expansion and the Wiener-Hermite expansion, we present the construction of generalized polynomial chaos. The techniques of representing a random variable and random process are discussed, and the outline of applying generalized polynomial chaos to a general stochastic system is presented. At the end of this chapter, we show convergence and efficiency of generalized polynomial chaos by solving a model stochastic ordinary differential equation.

In chapter 3, we consider the elliptic equation with uncertain inputs, i.e., random diffusivity, source term, and/or boundary conditions. An efficient block-Jacobi iterative algorithm is constructed to solve the coupled deterministic equations from the generalized polynomial chaos expansion. Several applications with diffusivity and source terms being random fields are solved via multi-dimensional chaos expansion. Finally, we propose a random mapping technique to tackle problems with uncertain boundary.

The parabolic equation, i.e., unsteady diffusion equation, is considered in chapter 4. In the first part, we apply the generalized polynomial chaos expansion to a simple diffusion equation with constant random diffusivity. The well-posedness of the semi-discrete system of equation resulted from the chaos expansion is studied. It is shown that Hermite-chaos expansion is ill-posed beyond a critical expansion order, due to the inappropriate Gaussian assumption on the random diffusivity. The lower and upper bounds of this critical expansion order are estimated via polynomial theory. On the other hand, the Jacobi-chaos is always well-posed as long as the support of diffusivity remains positive. Similar study on Laguerre-chaos is also conducted. In the second part of this chapter, the unsteady random diffusion equation is solved in a general setting. We first show convergence for a model one-dimensional problem, then apply the algorithm to unsteady random heat conduction in an electronic chip.

Chapter 5 includes the study of advection-diffusion equations. We first consider a linear advection-diffusion equation with random transport velocity, with a focus on the low viscosity cases. Special attention is paid on the solution statistics, including the evolution

of probability density function (PDF) of the solution. We show that the under-resolved Hermite-chaos solution may develop long tails which are not physical. In the second part of this chapter, we study the nonlinear advection-diffusion, i.e., the Burgers' equation. The supersensitivity of Burgers' equation, as illustrated in section 1.1, is considered, where a detailed numerical study is presented.

Incompressible flow subject to random inputs is the theme of chapter 6. After presenting the numerical procedure for discretizing Navier-Stokes equation via generalized polynomial chaos, we show three examples of two-dimensional flow. The first one is a microchannel flow driven by pressure drop, where the boundary conditions are random processes. Extensive Monte Carlo simulations are conducted to validate the results from generalized polynomial chaos. Next we study the effect of uncertainty in boundary conditions on the flow instability. To this end, we focus on an external flow (flow past a circular cylinder) and an internal flow (flow in a periodically driven grooved channel).

A summary is in chapter 7 to conclude this thesis, where we also address several important open issues in the development of generalized polynomial chaos.

Chapter 2

Orthogonal Polynomials and Generalized Polynomial Chaos

In this chapter, we present the constructions and basic properties of generalized polynomial chaos. Because these issues rely heavily on the theory of orthogonal polynomials, we first review briefly, in section 2.1, the fundamental properties of orthogonal polynomials and Askey scheme. In section 2.2, two important representation techniques for stochastic processes are discussed: the Karhunen-Loeve expansion and the Wiener-Hermite expansion. Karhunen-Loeve expansion provides a means of representing stochastic processes with reduced dimensionality in random space; Wiener-Hermite expansion is the original Wiener's polynomial chaos. The construction of the generalized polynomial chaos is then presented in section 2.3. Techniques to represent an arbitrary random variable and process are discussed (section 2.3.2 and 2.3.3), followed by applications to stochastic ordinary differential equation (section 2.3.4).

2.1 The Askey Scheme of Orthogonal Polynomials

The theory of orthogonal polynomials is relatively mature and many books have been devoted to their study (e.g. [10, 16, 117]). More recent work has shown that an important class of orthogonal polynomials belongs to the Askey scheme of hypergeometric polynomials [3]. In this section, we review the theory of hypergeometric orthogonal polynomials;

we adopt the notation of Koekoek and Swarttouw [65] and Schoutens [112].

2.1.1 Orthogonal Polynomials

Consider a system of polynomials $\{Q_n(x), n \in \mathcal{N}\}$, where $Q_n(x)$ is a polynomial of exact degree n and $\mathcal{N} = \{0, 1, 2, \dots\}$ or $\mathcal{N} = \{0, 1, \dots, N\}$ for a finite non-negative integer N . Every polynomial $Q_n(x)$ of degree n can be expressed in a monic version as

$$Q_n(x) = \sum_{k=0}^n a_k x^k, \quad n \geq 0, \quad a_n \neq 0. \quad (2.1)$$

$\{Q_n(x), n \in \mathcal{N}\}$ is an orthogonal system of polynomials if

$$\int_x Q_n(x) Q_m(x) w(x) dx = h_n^2 \delta_{mn}, \quad n, m \in \mathcal{N} \quad (2.2)$$

for continuous x , or in the discrete case

$$\sum_x Q_n(x) Q_m(x) w(x) = h_n^2 \delta_{mn}, \quad n, m \in \mathcal{N}. \quad (2.3)$$

Here $w(x)$ is the weighting function and δ_{mn} is the Kronecker delta. If the normalization coefficients $h_n^2(x) \equiv 1$, the system is called *orthonormal*.

Orthogonal polynomials $\{Q_n(x)\}$ satisfy a three-term recurrence relation

$$Q_{n+1}(x) = (A_n x + B_n) Q_n(x) - C_n Q_{n-1}(x), \quad n \geq 0, \quad (2.4)$$

where $A_n, C_n \neq 0$ and $C_n A_n A_{n-1} > 0$. Together with $Q_{-1}(x) = 0$ and $Q_0(x) = 1$, all $Q_n(x)$ can be determined by the recurrence relation. Another way of expressing the recurrence relation is

$$-x Q_n(x) = b_n Q_{n+1}(x) + \gamma_n Q_n(x) + c_n Q_{n-1}(x), \quad n \geq 0, \quad (2.5)$$

where $b_n, c_n \neq 0$, $c_n/b_{n-1} > 0$. An important converse theorem was proven by Favard [16].

Theorem 2.1 (Favard's Theorem). *Let A_n , B_n , and C_n be arbitrary sequences of real numbers and let $\{Q_n(x)\}$ be defined by the recurrence relation*

$$Q_{n+1}(x) = (A_n x + B_n)Q_n(x) - C_n Q_{n-1}(x), \quad n \geq 0,$$

together with $Q_0(x) = 1$ and $Q_{-1}(x) = 0$. Then the $\{Q_n(x)\}$ are a system of orthogonal polynomials if and only if $A_n \neq 0$, $C_n \neq 0$, and $C_n A_n A_{n-1} > 0$ for all n .

2.1.2 The Askey Scheme

We first introduce the *Pochhammer symbol* $(a)_n$ defined by

$$(a)_n = \begin{cases} 1, & \text{if } n = 0, \\ a(a+1) \cdots (a+n-1), & \text{if } n = 1, 2, 3, \dots \end{cases} \quad (2.6)$$

In terms of Gamma function, we have

$$(a)_n = \frac{\Gamma(a+n)}{\Gamma(a)}, \quad n > 0. \quad (2.7)$$

The *generalized hypergeometric series* ${}_rF_s$ is defined by

$${}_rF_s(a_1, \dots, a_r; b_1, \dots, b_s; z) = \sum_{k=0}^{\infty} \frac{(a_1)_k \cdots (a_r)_k}{(b_1)_k \cdots (b_s)_k} \frac{z^k}{k!}, \quad (2.8)$$

where $b_i \neq 0, -1, -2, \dots$ for $i = \{1, \dots, s\}$ to ensure the denominator factors in the terms of the series are never zero. Clearly, the ordering of the numerator parameters and of the denominator parameters are immaterial. The radius of convergence ρ of the hypergeometric series is

$$\rho = \begin{cases} \infty & \text{if } r < s + 1, \\ 1 & \text{if } r = s + 1, \\ 0 & \text{if } r > s + 1. \end{cases} \quad (2.9)$$

Some elementary cases of the hypergeometric series are:

- Exponential series ${}_0F_0$,

- Binomial series ${}_1F_0$,
- Gauss hypergeometric series ${}_2F_1$.

If one of the numerator parameters $a_i, i = 1, \dots, r$ is a negative integer, say $a_1 = -n$, the hypergeometric series (2.8) terminates at the n^{th} -term and becomes a polynomial in z , the *hypergeometric orthogonal polynomials*,

$${}_rF_s(-n, \dots, a_r; b_1, \dots, b_s; z) = \sum_{k=0}^n \frac{(-n)_k \cdots (a_r)_k}{(b_1)_k \cdots (b_s)_k} \frac{z^k}{k!}. \quad (2.10)$$

The Askey-scheme, which can be represented as a tree structure shown in figure 2.1, classifies the hypergeometric orthogonal polynomials and indicates the limit relations between them. The ‘tree’ starts with the Wilson polynomials and the Racah polynomials on the top. They both belong to the class ${}_4F_3$ of the hypergeometric orthogonal polynomials (2.10). The Wilson polynomials are continuous polynomials and the Racah polynomials are discrete. The lines connecting different polynomials denote the limit transition relationships between them, which imply that polynomials at the lower end of the lines can be obtained by taking the limit of one parameter from their counterparts on the upper end. For example, the limit relation between Jacobi polynomials $P_n^{(\alpha, \beta)}(x)$ and Hermite polynomials $H_n(x)$ is

$$\lim_{\alpha \rightarrow \infty} \alpha^{-\frac{1}{2}n} P_n^{(\alpha, \alpha)}\left(\frac{x}{\sqrt{\alpha}}\right) = \frac{H_n(x)}{2^n n!},$$

and between Meixner polynomials $M_n(x; \beta, c)$ and Charlier polynomials $C_n(x; a)$ is

$$\lim_{\beta \rightarrow \infty} M_n\left(x; \beta, \frac{a}{a + \beta}\right) = C_n(x; a).$$

For a detailed account of the limit relations of Askey-scheme, the interested reader should consult [65] and [112].

The orthogonal polynomials associated with the Wiener-Askey polynomials chaos include: Hermite, Laguerre, Jacobi, Charlier, Meixner, Krawtchouk and Hahn polynomials. A survey with their definitions and properties can be found in appendix A.

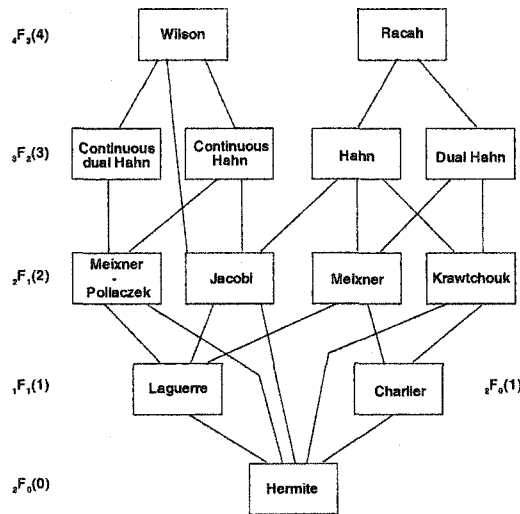


Figure 2.1: The Askey scheme of hypergeometric orthogonal polynomials.

2.2 Representation of Stochastic Processes

2.2.1 Karhunen-Loeve Expansion

The Karhunen-Loeve (KL) expansion is a method of representing a random process [79]. It is based on the spectral expansion of the correlation function of the process. It is particularly useful for the generalized polynomial chaos expansion as it provides a means of reducing dimensionality in random space. Let us denote the process by $h(\mathbf{x}; \omega)$ and its correlation function by $R_{hh}(\mathbf{x}, \mathbf{y})$, where \mathbf{x} and \mathbf{y} are the spatial or temporal coordinates. The KL expansion then takes the following form:

$$h(\mathbf{x}; \omega) = \bar{h}(\mathbf{x}) + \sum_{i=1}^{\infty} \sqrt{\lambda_i} \phi_i(\mathbf{x}) \xi_i(\omega), \quad (2.11)$$

where $\bar{h}(\mathbf{x})$ denotes the mean of the random process, and $\xi_i(\omega)$ forms a set of uncorrelated random variables. Also, $\phi_i(\mathbf{x})$ and λ_i are the eigenfunctions and eigenvalues of the

correlation function, respectively, i.e.,

$$\int R_{hh}(\mathbf{x}, \mathbf{y}) \phi_i(\mathbf{y}) d\mathbf{y} = \lambda_i \phi_i(\mathbf{x}). \quad (2.12)$$

In practice, a finite-term expansion of (2.11) is employed, where the summation is truncated at finite number n . The number of terms n is determined by the decay of eigenvalues from (2.12) to ensure the truncation error is acceptably small. Among other possible decompositions of a random process, the KL expansion is optimal in the sense that the mean-square error of the finite-term representation is minimized. It provides an effective way to represent the input random processes with known correlation function.

2.2.2 Wiener-Hermite Expansion

Wiener-Hermite expansion is the original polynomial chaos which was first introduced by Wiener [124]. It is also termed as the *homogeneous chaos*. It employs the *Hermite* polynomials in terms of *Gaussian* random variables. According to a theorem by Cameron and Martin [14], it can approximate any functionals in $L_2(C)$ and converges in the $L_2(C)$ sense, where C is the space of real functions which are continuous on the interval $[0, 1]$ and vanish at 0. Therefore, polynomial chaos provides a means for expanding second-order random processes in terms of Hermite polynomials. Second-order random processes are processes with finite variance, and this applies to most physical processes. Thus, a general second-order random process $X(\omega)$, viewed as a function of ω , i.e. the random event, can be represented in the form

$$\begin{aligned} X(\omega) &= a_0 H_0 \\ &+ \sum_{i_1=1}^{\infty} a_{i_1} H_1(\xi_{i_1}(\omega)) \\ &+ \sum_{i_1=1}^{\infty} \sum_{i_2=1}^{i_1} a_{i_1 i_2} H_2(\xi_{i_1}(\omega), \xi_{i_2}(\omega)) \\ &+ \sum_{i_1=1}^{\infty} \sum_{i_2=1}^{i_1} \sum_{i_3=1}^{i_2} a_{i_1 i_2 i_3} H_3(\xi_{i_1}(\omega), \xi_{i_2}(\omega), \xi_{i_3}(\omega)) \\ &+ \dots, \end{aligned} \quad (2.13)$$

where $H_n(\xi_{i_1}, \dots, \xi_{i_n})$ denote the *Hermite* polynomials of order n in terms of the multi-dimensional independent standard *Gaussian* random variables $\boldsymbol{\xi} = (\xi_{i_1}, \dots, \xi_{i_n})$ with zero mean and unit variance. The above equation is the discrete version of the original Wiener polynomial chaos expansion, where the continuous integrals are replaced by summations. The general expression of the Hermite polynomials is given by

$$H_n(\xi_{i_1}, \dots, \xi_{i_n}) = e^{\frac{1}{2}\boldsymbol{\xi}^T \boldsymbol{\xi}} (-1)^n \frac{\partial^n}{\partial \xi_{i_1} \dots \partial \xi_{i_n}} e^{-\frac{1}{2}\boldsymbol{\xi}^T \boldsymbol{\xi}}. \quad (2.14)$$

For example, the one-dimensional Hermite polynomials are:

$$\Psi_0 = 1, \quad \Psi_1 = \xi, \quad \Psi_2 = \xi^2 - 1, \quad \Psi_3 = \xi^3 - 3\xi, \quad \dots \quad (2.15)$$

For notational convenience, equation (2.13) can be rewritten as

$$X(\omega) = \sum_{j=0}^{\infty} \hat{a}_j \Psi_j(\boldsymbol{\xi}), \quad (2.16)$$

where there is a one-to-one correspondence between the functions $H_n(\xi_{i_1}, \dots, \xi_{i_n})$ and $\Psi_j(\boldsymbol{\xi})$, and also between the coefficients \hat{a}_j and a_{i_1, \dots, i_r} . In equation (2.13), the summation is carried out according to the order of the Hermite polynomials, while in equation (2.16) it is simply a re-numbering with the polynomials of lower order counted first. For clarity, the two-dimensional expansion is shown here, both in the fully expanded form (see equation (2.13))

$$\begin{aligned} X(\omega) &= a_0 H_0 + a_1 H_1(\xi_1) + a_2 H_1(\xi_2) \\ &+ a_{11} H_2(\xi_1, \xi_1) + a_{21} H_2(\xi_2, \xi_1) + a_{22} H_2(\xi_2, \xi_2) + \dots, \end{aligned} \quad (2.17)$$

and the simplified form (see equation (2.16))

$$\begin{aligned} X(\omega) &= \hat{a}_0 \Psi_0 + \hat{a}_1 \Psi_1 + \hat{a}_2 \Psi_2 + \hat{a}_3 \Psi_3 + \hat{a}_4 \Psi_4 + \hat{a}_5 \Psi_5 + \dots \\ &= \hat{a}_0 + \hat{a}_1 \xi_1 + \hat{a}_2 \xi_2 + \hat{a}_3 (\xi_1^2 - 1) + \hat{a}_4 (\xi_1 \xi_2) + \hat{a}_5 (\xi_2^2 - 1) + \dots \end{aligned} \quad (2.18)$$

The polynomial chaos forms a complete *orthogonal* basis in the L_2 space of the Gaussian random variables, i.e.,

$$\langle \Psi_i \Psi_j \rangle = \langle \Psi_i^2 \rangle \delta_{ij}, \quad (2.19)$$

where δ_{ij} is the Kronecker delta and $\langle \cdot, \cdot \rangle$ denotes the ensemble average. This is the inner product in the Hilbert space of the Gaussian random variables

$$\langle f(\boldsymbol{\xi})g(\boldsymbol{\xi}) \rangle = \int f(\boldsymbol{\xi})g(\boldsymbol{\xi})W(\boldsymbol{\xi})d\boldsymbol{\xi}. \quad (2.20)$$

The weighting function is

$$W(\boldsymbol{\xi}) = \frac{1}{\sqrt{(2\pi)^n}} e^{-\frac{1}{2}\boldsymbol{\xi}^T \boldsymbol{\xi}}, \quad (2.21)$$

where n is the dimension of $\boldsymbol{\xi}$. What distinguishes the Wiener-Hermite expansion from many other possible complete sets of expansions is that the polynomials here are orthogonal with respect to the weighting function $W(\boldsymbol{\xi})$ which has the form of the multi-dimensional independent Gaussian probability distribution with unit variance. We will use the term Hermite-chaos hereafter to denote the Wiener-Hermite polynomial chaos. For more details on the mathematical foundation of Hermite-chaos, see [27, 56, 124]; for its reformulation and applications to practical problems, see [39, 43].

2.3 Generalized Polynomial Chaos

2.3.1 Construction and Properties

The Hermite-chaos expansion has been quite effective in solving stochastic differential equations with Gaussian inputs as well as certain types of non-Gaussian inputs, e.g., lognormal distributions [40, 39, 43]; this can be justified by the Cameron-Martin theorem [14]. However, for general non-Gaussian random inputs, the convergence may be slow. In some cases, the convergence rate is, in fact, severely deteriorated.

In order to deal with more general random inputs, we introduce the generalized polynomial chaos expansion, the *Askey-chaos*, as a generalization of the original Wiener's Hermite-chaos expansion. The expansion basis of the Askey-chaos is formed by the complete set of orthogonal polynomials from the Askey scheme (see section 2.1.2). Similar to

section 2.2.2, we represent the general second-order random process $X(\omega)$ as

$$\begin{aligned}
X(\omega) &= a_0 I_0 \\
&+ \sum_{i_1=1}^{\infty} c_{i_1} I_1(\zeta_{i_1}(\omega)) \\
&+ \sum_{i_1=1}^{\infty} \sum_{i_2=1}^{i_1} c_{i_1 i_2} I_2(\zeta_{i_1}(\omega), \zeta_{i_2}(\omega)) \\
&+ \sum_{i_1=1}^{\infty} \sum_{i_2=1}^{i_1} \sum_{i_3=1}^{i_2} c_{i_1 i_2 i_3} I_3(\zeta_{i_1}(\omega), \zeta_{i_2}(\omega), \zeta_{i_3}(\omega)) \\
&+ \dots, \tag{2.22}
\end{aligned}$$

where $I_n(\zeta_{i_1}, \dots, \zeta_{i_n})$ denotes the Askey-chaos of order n in terms of the multi-dimensional random variables $\zeta = (\zeta_{i_1}, \dots, \zeta_{i_n})$. In the Askey-chaos expansion, the polynomials I_n are not restricted to Hermite polynomials but instead they could be any member of the Askey scheme, as shown in figure 2.1. Again for notational convenience, we rewrite equation (2.22) as

$$X(\omega) = \sum_{j=0}^{\infty} \hat{c}_j \Phi_j(\zeta), \tag{2.23}$$

where there is a one-to-one correspondence between the functions $I_n(\zeta_{i_1}, \dots, \zeta_{i_n})$ and $\Phi_j(\zeta)$, and their coefficients \hat{c}_j and c_{i_1, \dots, i_r} . Since each type of polynomials from the Askey scheme form a complete basis in the Hilbert space determined by their corresponding random vector ζ , we can expect each type of Askey-chaos to converge to any L_2 functional in the L_2 sense in the corresponding Hilbert functional space as a generalized result of Cameron-Martin theorem ([14] and [95]). The orthogonality relation of the Askey-chaos polynomial chaos takes the form

$$\langle \Phi_i \Phi_j \rangle = \langle \Phi_i^2 \rangle \delta_{ij}, \tag{2.24}$$

where δ_{ij} is the Kronecker delta and $\langle \cdot, \cdot \rangle$ denotes the ensemble average which is the inner product in the Hilbert space of the variables ζ

$$\langle f(\zeta)g(\zeta) \rangle = \int f(\zeta)g(\zeta)W(\zeta)d\zeta, \tag{2.25}$$

or

$$\langle f(\zeta)g(\zeta) \rangle = \sum_{\zeta} f(\zeta)g(\zeta)W(\zeta) \quad (2.26)$$

in the discrete case. Here $W(\zeta)$ is the weighting function corresponding to the Askey polynomials chaos basis $\{\Phi_i\}$; see appendix A for detailed formulas. We observe that some types of orthogonal polynomials from the Askey scheme have weighting functions of the same form as the probability function of certain types of random distributions. Subsequently, we choose the type of independent variables ζ in the polynomials $\{\Phi_i(\zeta)\}$ according to the type of random distributions as shown in table 2.1. It is clear that the

	Random variables ζ	Wiener-Askey chaos $\{\Phi_i(\zeta)\}$	Support
Continuous	Gaussian	Hermite-chaos	$(-\infty, \infty)$
	Gamma	Laguerre-chaos	$[0, \infty)$
	Beta	Jacobi-chaos	$[a, b]$
	Uniform	Legendre-chaos	$[a, b]$
Discrete	Poisson	Charlier-chaos	$\{0, 1, 2, \dots\}$
	Binomial	Krawtchouk-chaos	$\{0, 1, \dots, N\}$
	Negative Binomial	Meixner-chaos	$\{0, 1, 2, \dots\}$
	Hypergeometric	Hahn-chaos	$\{0, 1, \dots, N\}$

Table 2.1: The correspondence between the type of generalized polynomial chaos and their underlying random variables ($N \geq 0$ is a finite integer).

original Wiener polynomial chaos corresponds to the Hermite-chaos and is a subset of the Askey-chaos. The Hermite-, Laguerre- and Jacobi-chaos are *continuous chaos*, while Charlier-, Meixner-, Krawtchouk- and Hahn-chaos are *discrete chaos*. It is worth mentioning that the Legendre polynomials, which is a special case of the Jacobi polynomials $P_n^{(\alpha, \beta)}(x)$ with parameters $\alpha = \beta = 0$, correspond to an important distribution — the *uniform distribution*. Due to the importance of the uniform distribution, we list it separately in the table and term the corresponding chaos expansion as Legendre-chaos.

2.3.2 Representation of Random Variables

Each set of generalized polynomial chaos from table 2.1 can be employed to approximate a random variable, as they all form a complete set of bases. However, the convergence

properties of such approximations differ significantly in practice. In this section, we demonstrate the technique to represent a random variable with an arbitrary distribution by a chosen generalized polynomial chaos expansion. Such technique was first introduced in [130].

Suppose $y(\omega)$ is a random variable with continuous distribution function $G(y)$ and probability density function (PDF) $g(y)$ that satisfies $G(y) = \int_{-\infty}^y g(y)dy$. Let $\{\Phi(\xi)\}$ be a set of generalized polynomial chaos whose underlying random variable ξ has distribution function $F(\xi)$ and PDF $f(\xi)$ such that $F(\xi) = \int_{-\infty}^{\xi} f(\xi)d\xi$. The representation of y takes the form

$$y(\omega) = \sum_{k=0}^M y_k \Phi_k(\xi), \quad y_k = \frac{\langle y, \Phi_k(\xi) \rangle}{\langle \Phi_k^2(\xi) \rangle}. \quad (2.27)$$

Evaluation of the inner product $\langle \cdot, \cdot \rangle$ in the numerator needs caution as in most cases y and ξ belong to two different probability spaces. This difficulty can be circumvented by mapping both y and ξ to the space defined by the uniform random variable, i.e.

$$y(\omega) = G^{-1}(u(\omega)), \quad \xi(\omega) = F^{-1}(u(\omega)), \quad (2.28)$$

where $u(\omega) \in U(0, 1)$ is the uniform random variable in $(0, 1)$. Thus,

$$y_k = \frac{\langle y, \Phi_k(\xi) \rangle}{\langle \Phi_k^2(\xi) \rangle} = \frac{1}{\langle \Phi_k^2 \rangle} \int_0^1 G^{-1}(u) \Phi_k(F^{-1}(u)) du. \quad (2.29)$$

This integral is defined the closed domain $[0, 1]$ and can be evaluated by Gaussian quadrature with accuracy. The analytical form of the inversion (2.28) is not known in general, and numerical inversion is needed.

Approximation of Gamma distribution by Hermite-chaos

Let us assume that $y(\omega)$ is a random variable with gamma distribution (A.10). We consider the specific case of $\alpha = 0$. In this case y is an exponential random variable with PDF

$$f(y) = e^{-y}, \quad y > 0. \quad (2.30)$$

The inverse of its distribution function $F(y)$ (equation (2.28)) is known as

$$h(u) \equiv F^{-1}(u) = -\ln(1-u), \quad u \in U(0,1). \quad (2.31)$$

We then use Hermite-chaos to represent y instead of the optimal Laguerre-chaos. The random variable ξ in equation (2.27) is a standard Gaussian variable with PDF $g(\xi) = \frac{1}{\sqrt{2\pi}}e^{-\xi^2/2}$. The inverse of the Gaussian distribution $G(\xi)$ is known as

$$l(u) \equiv G^{-1}(u) = \text{sign}\left(u - \frac{1}{2}\right) \left(t - \frac{c_0 + c_1t + c_2t^2}{1 + d_1t + d_2t^2 + d_3t^3}\right), \quad (2.32)$$

where

$$t = \sqrt{-\ln[\min(u, 1-u)]^2}$$

and

$$\begin{aligned} c_0 &= 2.515517, & c_1 &= 0.802853, & c_2 &= 0.010328, \\ d_1 &= 1.432788, & d_2 &= 0.189269, & d_3 &= 0.001308. \end{aligned}$$

The formula is from Hastings [50] and the numeric values of the constants have absolute error less than 4.5×10^{-4} (also see [30]).

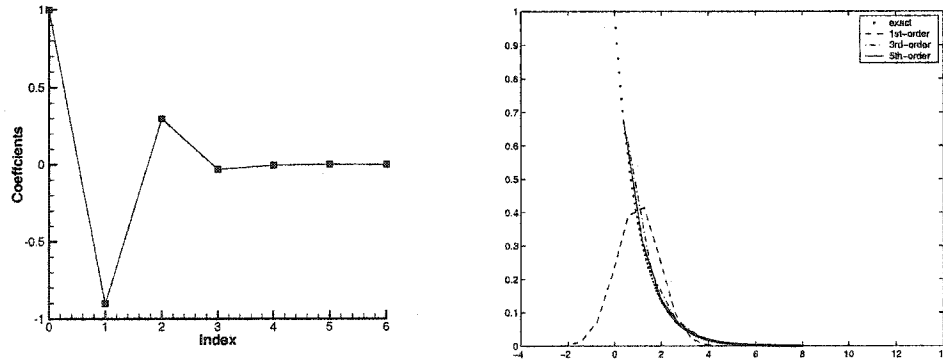


Figure 2.2: Approximation of exponential distribution with Hermite-chaos; Left: The expansion coefficients, Right: The PDF of different orders of approximations.

In figure 2.2 we show the result of the approximation of the exponential distribution by Hermite-chaos. The expansion coefficients y_i are shown on the left, and we see the major contributions of the Hermite-chaos approximation are from the first three terms. The

PDF of different orders of approximations are shown on the right, together with the exact PDF of the exponential distribution. We notice that the third-order approximation gives fairly good result and fifth-order Hermite-chaos is very close to the exact distribution. The Hermite-chaos does not approximate the PDF well at $x \sim 0$ where the PDF reaches its peak at 1. In order to capture this rather sharp region, more Hermite-chaos terms are needed. On the other hand, if we choose the appropriate generalized polynomial chaos, the Laguerre-chaos (see table 2.1), then the first-order expansion can represent the exponential random variable *exactly*.

Approximation of Beta distribution by Hermite-chaos

We now assume the distribution of $y(\omega)$ is a beta distribution (A.17). We return to the more conventional definition of beta distribution in the domain $[0, 1]$

$$f(y) = \frac{1}{B(\alpha + 1, \beta + 1)} y^\alpha (1 - y)^\beta, \quad \alpha, \beta > -1, \quad 0 \leq y \leq 1, \quad (2.33)$$

where $B(p, q) = \Gamma(p)\Gamma(q)/\Gamma(p + q)$ is the beta function. Figure 2.3 shows the PDF of

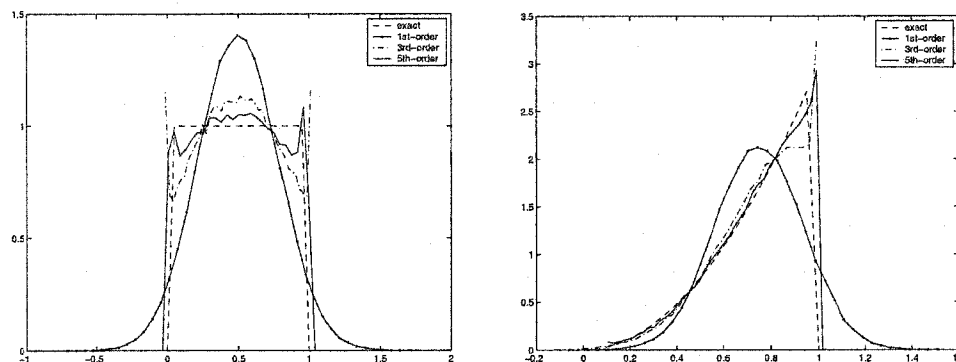


Figure 2.3: PDF of approximations of beta distributions by Hermite-chaos; Left: $\alpha = \beta = 0$, the uniform distribution, Right: $\alpha = 2, \beta = 0$.

first-, third- and fifth-order Hermite-chaos approximations to the beta random variable. The special case of $\alpha = \beta = 0$ is the uniform distribution. It can be seen that the Hermite-chaos approximation converges to the exact solution as the number of expansion terms increases. Oscillations are observed near the corners of the square. This is in analogy with the Gibb's phenomenon which occurs when Fourier expansions are used to

approximate functions with sharp corners. Since generalized polynomial chaos can be considered as spectral expansions in random space, the oscillations here can be regarded as the *stochastic Gibb's phenomenon*. For uniform distribution, Hermite-chaos does not work very well due to the stochastic Gibb's phenomenon even when more higher-order terms are added. On the other hand, the first-order Jacobi-chaos expansion is already *exact*.

These examples illustrate the flexibility of generalized polynomial chaos. With appropriately chosen bases, the generalized polynomial chaos can significantly reduce the number of expansion terms, the approximation errors, and subsequently, the computational effort.

2.3.3 Representation of Random Processes

To represent a stochastic process, the multi-dimensional generalized polynomial chaos expansion is needed. The multi-dimensional chaos expansion $\{\Phi(\boldsymbol{\xi})\}$ takes the tensor product form of its corresponding one-dimensional expansions, with each component ξ_i in the random vector $\boldsymbol{\xi} = (\xi_1, \xi_2, \dots)$ being independent to the rest. (Equations (2.17) and (2.16) demonstrate the two-dimensional expansions for Hermite-chaos.) Thus, in order to represent a random process by generalized polynomial chaos, we need to decompose the process into functions of independent components ξ_i . Since each component defines a dimension in random space, the total number of ξ_i needs to be minimized.

To this end, the Karhunen-Loeve can be employed. Following section 2.2.1, for a given random process $h(\mathbf{x}; \omega)$ with correlation function $R_{hh}(\mathbf{x}, \mathbf{y})$, where \mathbf{x} and \mathbf{y} are the spatial or temporal coordinates, the finite-term KL expansion takes the following form:

$$\hat{h}(\mathbf{x}; \omega) = \bar{h}(\mathbf{x}) + \sum_{i=1}^n \sqrt{\lambda_i} \phi_i(\mathbf{x}) \xi_i(\omega), \quad (2.34)$$

where $\bar{h}(\mathbf{x})$ is the mean of the random process, and $\xi_i(\omega)$ forms a set of *uncorrelated* random variables. $\phi_i(\mathbf{x})$ and λ_i are the solutions of the eigen-problem (2.12).

We further assume that $\xi_i, i = 1, \dots, n$ are *independent*. The generalized polynomial chaos is then a n -dimensional expansion in term of $\boldsymbol{\xi} = (\xi_1, \dots, \xi_n)$. It should be noted

that the ξ_i from KL expansion (2.34) are uncorrelated. Except for the Gaussian distribution, they are not necessarily independent. As a result of the ‘independence assumption’, the model process $\hat{h}(\mathbf{x};\omega)$ may not match the target process $h(\mathbf{x};\omega)$ well. Alternative approaches to decompose an input *non-Gaussian* random process into independent components are required, and more research effort is needed. In this thesis, we will adopt the ‘independence assumption’ for KL decomposition of non-Gaussian processes, similar as in [5, 6, 21]. We note that this assumption does not intervene in our study of the properties of generalized polynomial chaos.

2.3.4 Solutions of Stochastic Equations

Let us consider the stochastic differential equation

$$\mathcal{L}(\mathbf{x}, t, \omega; u) = f(\mathbf{x}, t; \omega), \quad (2.35)$$

where $u := u(\mathbf{x}, t; \omega)$ is the solution and $f(\mathbf{x}, t; \omega)$ is the source term. Operator \mathcal{L} generally involves differentiations in space/time and can be nonlinear. Appropriate initial and boundary conditions are assumed. The existence of random parameter ω is due to the introduction of uncertainty into the system via boundary conditions, initial conditions, material properties, etc. The solution u , which is regarded as a random process, can be expanded by the Wiener-Askey polynomial chaos as

$$u(\mathbf{x}, t; \omega) = \sum_{i=0}^M u_i(\mathbf{x}, t) \Phi_i(\boldsymbol{\xi}(\omega)). \quad (2.36)$$

Note here the infinite summation has been truncated at the finite term M . The total number of expansion terms is $(M + 1)$, and is determined by the dimension (n) of random vector $\boldsymbol{\xi}$ and the highest order (p) of the polynomials $\{\Phi_i\}$;

$$(M + 1) = \frac{(n + p)!}{n!p!} \quad (2.37)$$

Upon substituting equation (2.36) into the governing equation (2.35), we obtain

$$\mathcal{L} \left(\mathbf{x}, t, \omega; \sum_{i=0}^M u_i \Phi_i \right) = f(\mathbf{x}, t; \omega). \quad (2.38)$$

A Galerkin projection of the above equation onto each polynomial basis $\{\Phi_i\}$ is then conducted in order to ensure the error is orthogonal to the functional space spanned by the finite-dimensional basis $\{\Phi_i\}$,

$$\left\langle \mathcal{L} \left(\mathbf{x}, t, \omega; \sum_{i=0}^M u_i \Phi_i \right), \Phi_k \right\rangle = \langle f, \Phi_k \rangle, \quad k = 0, 1, \dots, M. \quad (2.39)$$

By using the orthogonality of the polynomial basis, we can obtain a set of $(M+1)$ coupled equations for each random mode $u_i(\mathbf{x}, t)$ where $i = \{0, 1, \dots, M\}$. It should be noted that by utilizing the Wiener-Askey polynomial chaos expansion (2.36), the randomness is effectively transferred into the basis polynomials. Thus, the governing equations for the expansion coefficients u_i resulted from equation (2.39) are *deterministic*. Discretizations in space \mathbf{x} and time t can be carried out by any conventional deterministic techniques, e.g., Runge-Kutta solvers in time and finite element method in physical space.

2.3.5 Application to Stochastic Ordinary Differential Equations

We consider the ordinary differential equation

$$\frac{dy(t)}{dt} = -ky, \quad y(0) = \hat{y}, \quad (2.40)$$

where the decay rate coefficient k is considered to be a random variable $k(\omega)$ with certain distribution and mean value \bar{k} . The probability function is $f(k)$ for the continuous case or $f(k_i)$ for the discrete case. The *deterministic* solution is

$$y(t) = y_0 e^{-\bar{k}t} \quad (2.41)$$

and the *mean of stochastic* solution is

$$\bar{y}(t) = \hat{y} \int_S e^{-kt} f(k) dk \quad \text{or} \quad \bar{y}(t) = \hat{y} \sum_i e^{-k_i t} f(k_i) \quad (2.42)$$

corresponding to the continuous and discrete distributions, respectively. The integration and summation are taken within the support defined by the corresponding distribution.

By applying the Wiener-Askey polynomial chaos expansion (2.23) to the solution y and random input k

$$y(t) = \sum_{i=0}^M y_i(t) \Phi_i, \quad k = \sum_{i=0}^M k_i \Phi_i \quad (2.43)$$

and substituting the expansions into the governing equation, we obtain

$$\sum_{i=0}^M \frac{dy_i(t)}{dt} \Phi_i = - \sum_{i=0}^M \sum_{j=0}^M \Phi_i \Phi_j k_i y_j(t). \quad (2.44)$$

We then project the above equation onto the random space spanned by the orthogonal polynomial basis $\{\Phi_i\}$ by taking the inner product of the equation with each basis. By taking $\langle \cdot, \Phi_l \rangle$ and utilizing the orthogonality condition (2.24), we obtain the following set of equations:

$$\frac{dy_l(t)}{dt} = - \frac{1}{\langle \Phi_l^2 \rangle} \sum_{i=0}^M \sum_{j=0}^M e_{ijl} k_i y_j(t), \quad l = 0, 1, \dots, M, \quad (2.45)$$

where $e_{ijl} = \langle \Phi_i \Phi_j \Phi_l \rangle$. Note that the coefficients are smooth and thus any standard ODE solver can be employed here. In the following the standard second-order Runge-Kutta scheme is used.

For the purpose of benchmarking, we will arbitrarily assume the type of distributions of the decay parameter k and employ the corresponding Wiener-Askey chaos expansion, although in practice there is certainly more favorable assumptions about k depending on the specific physical background. Since the only random input is k , the one-dimensional chaos expansion is employed, i.e. $n = 1$ in (2.37). Thus, the total number of expansion terms is $(M + 1) = P + 1$, where P is the highest order of polynomials. We define the two

error measures for the mean and variance of the solution

$$\varepsilon_{\text{mean}}(t) = \left| \frac{\bar{y}(t) - \bar{y}_{\text{exact}}(t)}{\bar{y}_{\text{exact}}(t)} \right|, \quad \varepsilon_{\text{var}}(t) = \left| \frac{\sigma(t) - \sigma_{\text{exact}}(t)}{\sigma_{\text{exact}}(t)} \right|, \quad (2.46)$$

where $\bar{y}(t) = E[y(t)]$ is the mean value of $y(t)$ and $\sigma(t) = E[(y(t) - \bar{y}(t))^2]$ is the variance of the solution. The initial condition is fixed to be $\hat{y} = 1$ and the integration is performed up to $t = 1$ (nondimensional time units).

Gaussian Distribution and Hermite-chaos

In this section the distribution of k is assumed to be a Gaussian random variable with probability density function

$$f(k) = \frac{1}{\sqrt{2\pi}} e^{-k^2/2} \quad (2.47)$$

which has zero mean value ($\bar{k} = 0$) and unit variance ($\sigma_k^2 = 1$). The exact stochastic mean solution is

$$\bar{y}(t) = \hat{y} e^{t^2/2}. \quad (2.48)$$

The Hermite-chaos from the Wiener-Askey polynomial chaos family is employed as a natural choice due to the fact that the random input is Gaussian. Figure 2.4 shows the

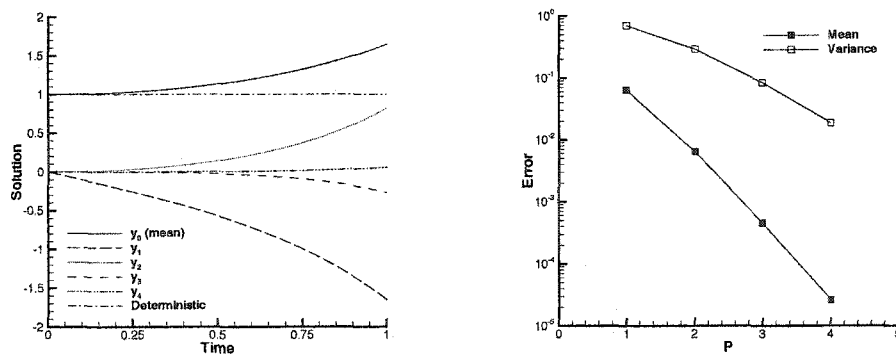


Figure 2.4: Solution with Gaussian random input by 4th-order Hermite-chaos; Left: Solution of each random mode, Right: Error convergence of the mean and the variance.

solution by the Hermite-chaos expansion. The convergence of errors of the mean and variance as the number of expansion terms increases is shown on semi-log plot, and it

is seen that the *exponential* convergence rate is achieved. It is also noticed that the *deterministic* solution remains constant as the mean value of k is zero; however the mean of the stochastic solution (random mode with index 0, y_0) is nonzero and grows with time.

Gamma Distribution and Laguerre-chaos

In this section we assume the distribution of the decay parameter k is the gamma distribution with PDF of the form

$$f(k) = \frac{e^{-k} k^\alpha}{\Gamma(\alpha + 1)}, \quad 0 \leq k < \infty, \quad \alpha > -1. \quad (2.49)$$

The mean and variance of k are: $\mu_k = \bar{k} = \alpha + 1$ and $\sigma_k^2 = \alpha + 1$, respectively. The mean of stochastic solution is

$$\bar{y}(t) = \hat{y} \frac{1}{(1+t)^{\alpha+1}}. \quad (2.50)$$

The special case of $\alpha = 0$ corresponds to another important distribution: the *exponential* distribution. Because the random input has a Gamma distribution, we employ the

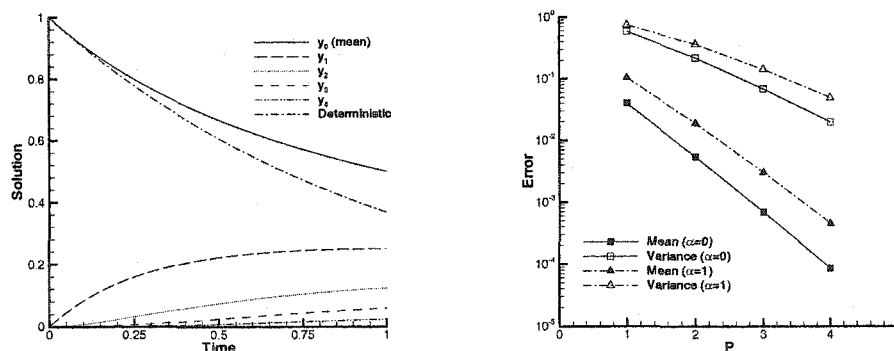


Figure 2.5: Solution with Gamma random input by 4th-order Laguerre-chaos; Left: Solution of each mode ($\alpha = 0$: exponential distribution), Right: Error convergence of the mean and the variance with different α .

Laguerre-chaos as the specific Wiener-Askey chaos (see table 2.1). Figure 2.5 shows the evolution of each solution mode over time, together with the convergence of the errors of the mean and the variance with different values of parameter α . The special case of exponential distribution is included ($\alpha = 0$). Again the mean of stochastic solution

and deterministic solution show significant difference. As α becomes larger, the spread of the Gamma distribution is larger and this leads to larger errors with fixed number of Laguerre-chaos expansion. However, the exponential convergence rate is still realized.

Beta Distribution and Jacobi-chaos

We now assume the distribution of the random variable k to be the beta distribution with probability density function of the form

$$f(k; \alpha, \beta) = \frac{(1-k)^\alpha (1+k)^\beta}{2^{\alpha+\beta+1} B(\alpha+1, \beta+1)}, \quad -1 < k < 1, \quad \alpha, \beta > -1, \quad (2.51)$$

where $B(\alpha, \beta)$ is the Beta function defined as $B(p, q) = \Gamma(p)\Gamma(q)/\Gamma(p+q)$. We then employ the Jacobi-chaos expansion which has the weighting function in the form of the Beta distribution. An important special case is $\alpha = \beta = 0$ when the distribution becomes the uniform distribution and the corresponding Jacobi-chaos becomes the Legendre-chaos.

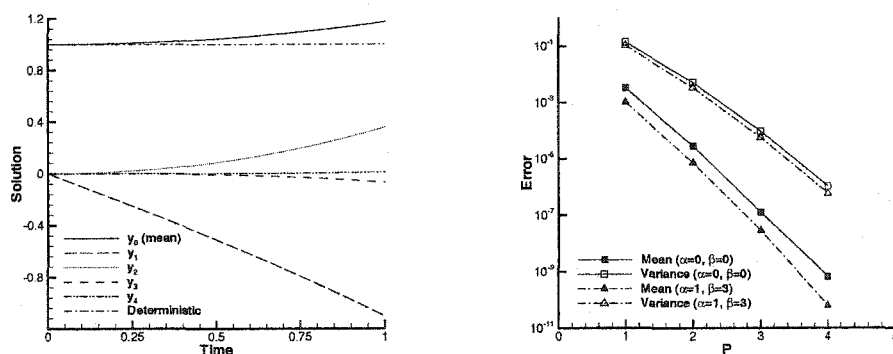


Figure 2.6: Solution with Beta random input by 4th-order Jacobi-chaos; Left: Solution of each mode ($\alpha = \beta = 0$: Legendre-chaos), Right: Error convergence of the mean and the variance with different α and β .

Figure 2.6 shows the solution by the Jacobi-chaos. On the left is the evolution of all random modes of the Legendre-chaos ($\alpha = \beta = 0$) with uniformly distributed random input. In this case, k has zero mean value and the deterministic solution remains constant, but the mean of stochastic solution grows over time. The convergence of errors of the

mean and the variance of the solution with respect to the order of Jacobi-chaos expansion is shown on the semi-log scale, and the exponential convergence rate is obtained with different sets of parameter values α and β .

Poisson Distribution and Charlier-chaos

We now assume the distribution of the decay parameter k to be Poisson of the form

$$f(k; \lambda) = e^{-\lambda} \frac{\lambda^k}{k!}, \quad k = 0, 1, 2, \dots, \lambda > 0. \quad (2.52)$$

The mean and variance of k are: $\mu_k = \bar{k} = \lambda$ and $\sigma_k^2 = \lambda$, respectively. The analytic solution of the mean stochastic solution is

$$\bar{y}(t) = \hat{y} e^{-\lambda + \lambda e^{-t}}. \quad (2.53)$$

The Charlier-chaos expansion is employed to represent the solution process and the re-

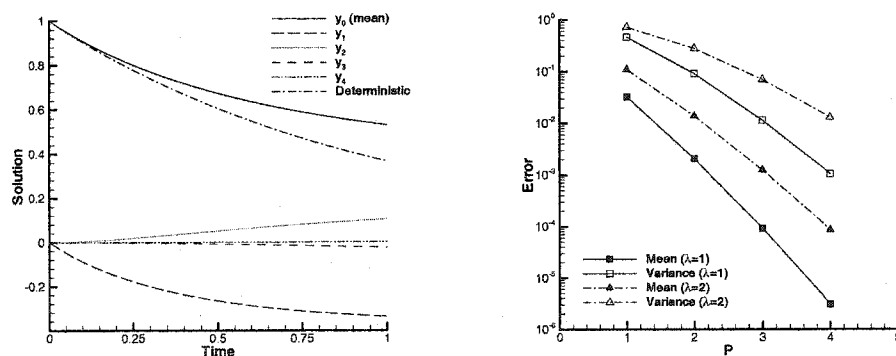


Figure 2.7: Solution with Poisson random input by 4th-order Charlier-chaos; Left: Solution of each mode ($\lambda = 1$), Right: Error convergence of the mean and the variance with different λ .

sults with fourth-order expansion are shown in figure 2.7. Once again we see the noticeable difference between the deterministic solution and the mean of stochastic solution. Exponential convergence rate is obtained for different values of parameter λ .

Binomial Distribution and Krawtchouk-chaos

In this section the distribution of the random input k is assumed to be binomial

$$f(k; p, N) = \binom{N}{k} p^k (1-p)^{N-k}, \quad 0 \leq p \leq 1, \quad k = 0, 1, \dots, N. \quad (2.54)$$

The exact mean solution of (2.40) is

$$\bar{y}(t) = \hat{y} [1 - (1 - e^{-t}) p]^N. \quad (2.55)$$

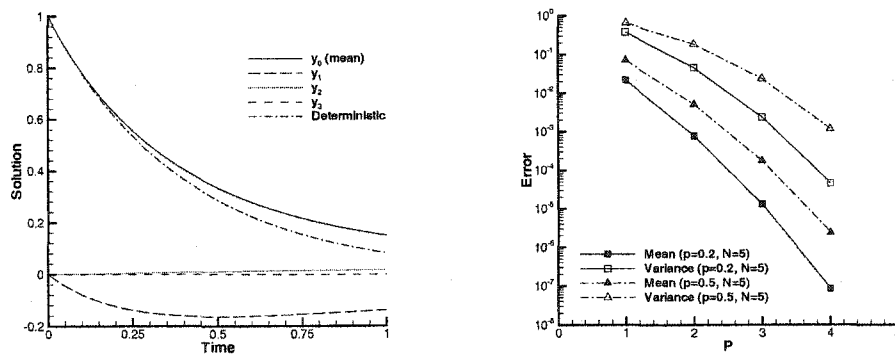


Figure 2.8: Solution with binomial random input by 4th-order Krawtchouk-chaos; Left: Solution of each mode ($p = 0.5, N = 5$), Right: Error convergence of the mean and the variance with different p and N .

Figure 2.8 shows the solution with 4th-order Krawtchouk-chaos. With different parameter sets, Krawtchouk-chaos expansion correctly approximates the exact solution, and the convergence rate with respect to the order of expansion is exponential.

Negative Binomial Distribution and Meixner-chaos

In this section we assume the distribution of the random input of k is the negative binomial distribution

$$f(k; \beta, c) = \frac{(\beta)_k}{k!} (1-c)^\beta c^k, \quad 0 \leq c \leq 1, \quad \beta > 0, \quad k = 0, 1, \dots \quad (2.56)$$

In case of β being integer, it is often called the Pascal distribution. The exact mean solution of (2.40) is

$$\bar{y}(t) = \hat{y} \left(\frac{1 - ce^{-t}}{1 - c} \right)^{-\beta}. \quad (2.57)$$

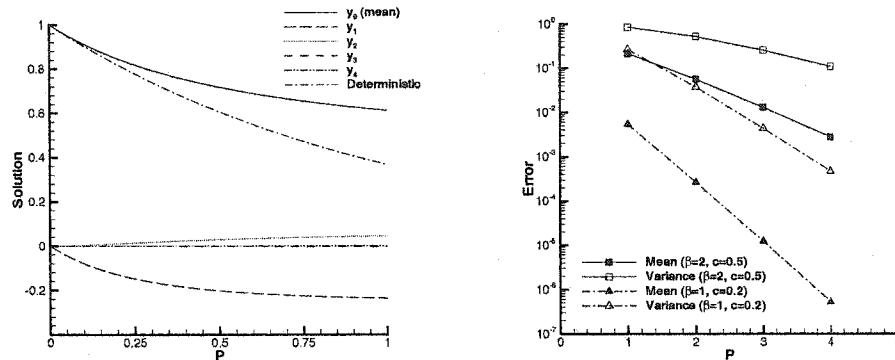


Figure 2.9: Solution with negative binomial random input by 4th-order Meixner-chaos; Left: Solution of each mode ($\beta = 1, c = 0.5$), Right: Error convergence of the mean and the variance with different β and c .

The Meixner-chaos is chosen since the random input is negative binomial (see table 2.1). Figure 2.9 shows the solution with 4th-order Meixner-chaos. Exponential convergence rate is observed by the Meixner-chaos approximation with different sets of parameter values.

Hypergeometric Distribution and Hahn-chaos

We now assume the distribution of the random input k is hypergeometric

$$f(k; \alpha, \beta, N) = \frac{\binom{\alpha}{k} \binom{\beta}{N-k}}{\binom{\alpha+\beta}{N}}, \quad k = 0, 1, \dots, N, \quad \alpha, \beta > N. \quad (2.58)$$

In this case, the optimal Wiener-Askey polynomial chaos is the Hahn-chaos (table 2.1). Figure 2.10 shows the solution by 4th-order Hahn-chaos. It can be seen from the semi-log plot of the errors of the mean and variance of the solution that exponential convergence rate is obtained with respect to the order of Hahn-chaos expansion for different sets of parameter values.

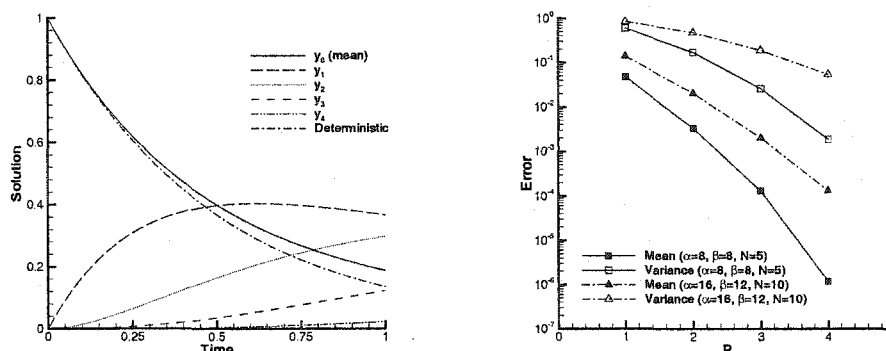


Figure 2.10: Solution with hypergeometric random input by 4th-order Hahn-chaos; Left: Solution of each mode ($\alpha = \beta = 5, N = 4$), Right: Error convergence of the mean and the variance with different α, β and N .

Effect of Non-optimal Basis

The flexibility of generalized polynomial chaos is demonstrated in section 2.3.2 for the approximation of an arbitrary random variable. Here we further stress this point by solving stochastic equations. We return to the stochastic ODE problem (2.40) with exponential random parameter k (2.49). If the optimal generalized polynomial chaos is chosen, in this case the Laguerre-chaos, only one term is needed to represent k *exactly*, and the errors in numerical solutions decay exponentially fast as the order of expansion increases (see figure 2.5). We can expect if the Hermite-chaos is used to solve the differential equation in this case, the solution would not retain the exponential convergence as realized by the Laguerre-chaos.

In figure 2.11 the errors of mean solution defined by equation (2.46) with Laguerre-chaos and Hermite-chaos to the ODE of equation (2.40) are shown. The random input of k has exponential distribution which implies that the Laguerre-chaos is the optimal Wiener-Askey polynomial chaos. It is seen from the result that the exponential convergence rate is not obtained by the Hermite-chaos as opposed to the Laguerre-chaos.

Efficiency of Generalized Polynomial Chaos

We have demonstrated the exponential convergence of the generalized polynomial chaos expansion. From the results above, we notice that it normally takes an expansion order

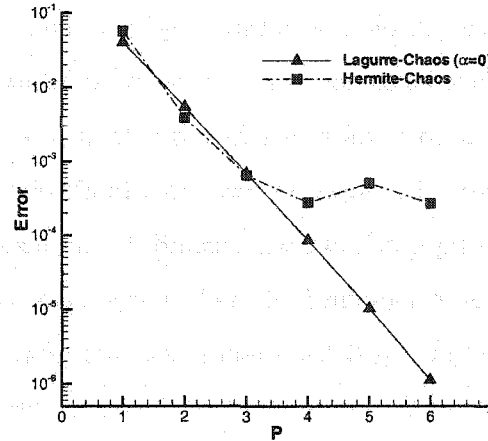


Figure 2.11: Error convergence of the mean solution of the Laguerre-chaos and Hermite-chaos to stochastic ODE with random input of the exponential distribution

$P = 2 \sim 4$ for the error of the mean solution to reach the order of $O(10^{-3})$. Equation (2.45) shows that the Wiener-Askey chaos expansion with highest order of P results in a set of $(P + 1)$ coupled ODEs. Thus, the computational cost is slightly more than $(P + 1)$ times of that of a single realization of the deterministic integration. On the other hand, if the Monte-Carlo simulation is used, it normally requires $O(10^4) \sim O(10^5)$ number of realizations to reduce the error of the *mean* solution to $O(10^{-3})$. For example, if k is an exponentially distributed random variable, the error convergence of the mean solution of the Monte-Carlo simulation is shown in table 2.2.

N	1×10^2	1×10^3	1×10^4	1×10^5
$\varepsilon_{\text{mean}}$	4.0×10^{-2}	1.1×10^{-2}	5.1×10^{-3}	6.5×10^{-4}

Table 2.2: Error convergence of the mean solution by Monte-Carlo simulation: N is the number of realizations and $\varepsilon_{\text{mean}}$ is the error of mean solution defined in (2.46); Random input has exponential distribution.

Monte-Carlo simulations with other types of random inputs as discussed in this paper have also been conducted and the results are similar. The actual numerical values of the errors with given number of realizations may vary depending on the property of random number generators used, but the order of magnitude should be the same. Techniques such

as variance reduction are not used. Although such techniques, if applicable, can greatly speed up Monte-Carlo simulation by an order or more depending on the specific problem, the advantage of generalized polynomial chaos expansion is obvious. For the ordinary differential equation discussed in this paper, speed-up of order $O(10^3) \sim O(10^4)$ compared with straight Monte-Carlo simulations can be expected. However, for more complicated problems where there exist multi-dimensional random inputs, the multi-dimensional generalized polynomial chaos is needed. The total number of expansion terms increases fast for large dimensional problems (see equation(2.37)). Thus the efficiency of the chaos expansion can be reduced.

Chapter 3

Elliptic Equations

The objective of this chapter is to give a broad algorithmic framework to solve stochastic elliptic partial differential equations based on the generalized polynomial chaos expansion.

The class of problems we solve has the form

$$\begin{cases} \nabla \cdot [\kappa(x; \omega) \nabla u(x; \omega)] = f(x; \omega), & (x; \omega) \in D \times \Omega \\ u(x; \omega) = g(x; \omega), & (x; \omega) \in \partial D \times \Omega \end{cases} \quad (3.1)$$

where D is a bounded domain in \mathbb{R}^d ($d = 1, 2, 3$) and Ω is a probability space. f , g and κ are \mathbb{R} -values functions on $D \times \Omega$. This can be considered as a model of steady state diffusion problems subject to internal (diffusivity κ) and/or external (source term f and/or Dirichlet boundary condition g) uncertainties. Babuška was among the first to study rigorously *existence* of solutions of the random Dirichlet problem [4]. Bécus & Cozzarelli studied the existence and properties of the general solution to (3.1), see [7, 8, 9]. Also, in [5, 6, 21] the problem subject to random diffusivity and/or random source terms was studied and existence and uniqueness of the solution in the finite element concept, both in physical space and random space, were addressed. Equation (3.1) is also the model used for flow in porous media, and a large quantity of literature exist on its probabilistic solutions. Most work, however, is based on perturbation methods or moment equations approach (cf. [18, 19, 90, 127, 126, 137]). Extensive research efforts have also be devoted to the evaluation of the ‘effective diffusivity’ or ‘effective permeability’ of the media [100, 101].

In this chapter, we solve the steady state diffusion problem (3.1) by generalized polynomial chaos expansion, where the uncertainties can be introduced through κ , f , or g , or some combinations. It is worth noting that when both κ and u are random, it is not obvious how to give a mathematical meaning or justification to the product of two stochastic processes if they are not smooth. However, the product is well defined in terms of the chaos expansion by using the concept of Wick product and Kondratiev space [54, 85].

3.1 Stochastic Formulations and a Block-Jacobi Iterative Algorithm

In this section we present the detailed algorithm for the application of the generalized polynomial chaos expansion to equation (3.1). By applying the chaos expansion, we expand the variables as

$$\kappa(x; \omega) = \sum_{i=0}^M \kappa_i(x) \Phi_i(\boldsymbol{\xi}), \quad u(x; \omega) = \sum_{i=0}^M u_i(x) \Phi_i(\boldsymbol{\xi}), \quad f(x; \omega) = \sum_{i=0}^M f_i(x) \Phi_i(\boldsymbol{\xi}), \quad (3.2)$$

where we have replaced the infinite summation of $\boldsymbol{\xi}$ in infinite dimensions in equation (2.23) by a truncated finite-term summation of $\{\Phi\}$ in the finite dimensions of $\boldsymbol{\xi} = (\xi_1, \dots, \xi_n)$. The dimensionality n of $\boldsymbol{\xi}$ is determined by the random inputs. The random parameter ω is absorbed into the polynomial basis $\Phi(\boldsymbol{\xi})$, thus the expansion coefficients k_i and u_i are deterministic. By substituting the expansion into governing equation (3.1), we obtain

$$\nabla \cdot \left[\sum_{i=0}^M \kappa_i(x) \Phi_i \nabla \left(\sum_{j=0}^M u_j(x) \Phi_j \right) \right] = \sum_{i=0}^M f_i(x) \Phi_i. \quad (3.3)$$

Upon simplification, it can be written as

$$\sum_{i=0}^M \sum_{j=0}^M [\kappa_i(x) \nabla^2 u_j(x) + \nabla \kappa_i(x) \cdot \nabla u_j(x)] \Phi_i \Phi_j = \sum_{i=0}^M f_i(x) \Phi_i. \quad (3.4)$$

A Galerkin projection of the above equation onto each polynomial basis $\{\Phi_i\}$ is then conducted in order to ensure that the error is orthogonal to the functional space spanned

by the finite-dimensional basis $\{\Phi_i\}$. By projecting with Φ_k for each $k = \{0, \dots, M\}$ and employing the orthogonality relation (2.24), we obtain for each $k = 0, \dots, M$,

$$\sum_{i=0}^M \sum_{j=0}^M [\kappa_i(x) \nabla^2 u_j(x) + \nabla \kappa_i(x) \cdot \nabla u_j(x)] e_{ijk} = f_k(x) \langle \Phi_k^2 \rangle, \quad (3.5)$$

where $e_{ijk} = \langle \Phi_i \Phi_j \Phi_k \rangle$. By defining

$$b_{jk}(x) = \sum_{i=0}^M \kappa_i(x) e_{ijk}, \quad h_{jk}(x) = \sum_{i=0}^M \nabla \kappa_i(x) e_{ijk} = \nabla b_{jk}(x),$$

we can rewrite the above equation as

$$\sum_{j=0}^M [b_{jk}(x) \nabla^2 u_j(x) + h_{jk}(x) \cdot \nabla u_j(x)] = f_k(x) \langle \Phi_k^2 \rangle, \quad \forall k \in [0, M]. \quad (3.6)$$

Equation (3.6) is a set of $(M + 1)$ coupled elliptic partial differential equations. These equations are *deterministic* and can be solved by any conventional method, e.g. finite elements. In this paper we employ the spectral/*hp* element method [63]. The total number of equations $(M + 1)$ is determined by the dimensionality of the chaos expansion (n) and the highest order (p) of the polynomials $\{\Phi\}$, i.e. $(M + 1) = (n + p)! / (n! p!)$ from equation (2.37).

While it is possible to solve equation (3.6) via a direct solver, we choose to use an iterative method to take advantage of the diagonal dominance of the block matrix $B = \{b_{jk}\}$. In particular, we employ a block Gauss-Seidel iteration in the following form: for all $k = 0, \dots, M$,

$$\begin{aligned} b_{kk}(x) \nabla^2 u_k^{n+1}(x) + h_{kk}(x) \cdot \nabla u_k^{n+1}(x) &= f_k(x) \langle \Phi_k^2 \rangle \\ &- \sum_{j=0}^{k-1} [b_{jk}(x) \nabla^2 u_j^{n+1}(x) + h_{jk}(x) \cdot \nabla u_j^{n+1}(x)] \\ &- \sum_{j=k+1}^M [b_{jk}(x) \nabla^2 u_j^n(x) + h_{jk}(x) \cdot \nabla u_j^n(x)], \end{aligned} \quad (3.7)$$

where the superscript n denotes the iteration number. The convergence criterion is defined

as

$$\frac{\|u_k^{n+1}(x) - u_k^n(x)\|}{\|u_k^1(x) - u_k^0(x)\|} \leq \varepsilon, \quad \forall k \in [0, M], \quad (3.8)$$

where ε is a small positive number and different types of norm $\|\cdot\|$ can be used. Here the L_∞ norm is used and ε is set to be $10^{-5} \sim 10^{-7}$. For all the results we present here, the block Gauss-Seidel iteration normally converges within about 10 steps. A similar iteration technique was used in [2] for stochastic modeling of elasto-plastic body problems with the Hermite-chaos and fast convergence was reported too.

3.2 Numerical Examples

In this section we present numerical results of the proposed generalized polynomial chaos expansion to stochastic diffusion problem. We first consider an one-dimensional model problem where the exact solution is available; then a more complicated two-dimensional problem where we use Monte Carlo simulation to validate the chaos solution. Among the types of chaos expansions listed in table 2.1, we choose two continuous chaos: Hermite-chaos and Jacobi-chaos; and two discrete chaos: Charlier-chaos and Krawtchouk-chaos for demonstration purposes. Finally, we solve the random heat conduction problem in a grooved channel as an example of a more practical application.

3.2.1 One-Dimensional Model Problem

Consider the following problem

$$\frac{d}{dx} \left[\kappa(x; \omega) \frac{du}{dx}(x; \omega) \right] = 0, \quad x \in [0, 1], \quad (3.9)$$

with boundary conditions

$$u(0; \omega) = 0, \quad u(1; \omega) = 1.$$

The random diffusivity has the form

$$\kappa(x; \omega) = 1 + \varepsilon(\omega)x, \quad (3.10)$$

where $\epsilon(\omega)$ is a random variable, and $\kappa(x; \omega) > 0$. The exact solution to this problem is

$$u_e(x; \omega) = \begin{cases} \ln[1 + \epsilon(\omega)x] / \ln[1 + \epsilon(\omega)], & \text{for } \epsilon(\omega) \neq 0; \\ x, & \text{for } \epsilon(\omega) = 0. \end{cases} \quad (3.11)$$

The ‘mean-square’ error of the numerical solution from the generalized chaos expansion $u_p(x, \omega)$ is computed

$$e_2(x) = \left(\mathbb{E} [u_p(x, \omega) - u_e(x, \omega)]^2 \right)^{\frac{1}{2}},$$

where \mathbb{E} denotes the ‘expectation’ operator and p is the order of the chaos expansion. Specifically, we examine the ‘mean-square’ convergence (L_2 convergence in random space) of the L_∞ norm (in physical space) of $e_2(x)$ as p increases.

Jacobi-chaos and Beta Distribution

We assume $\epsilon(\omega) = \sigma\xi(\omega)$ in equation (3.10) is a *beta* random variable, where $\sigma > 0$ measures the magnitude of input uncertainty and $\xi(\omega)$ is a standard beta random variable in $(-1, 1)$ with PDF (A.17)

$$f(\xi; \alpha, \beta) = \frac{(1 - \xi)^\alpha (1 + \xi)^\beta}{2^{\alpha+\beta+1} B(\alpha + 1, \beta + 1)}, \quad \xi \in [-1, 1], \quad \alpha, \beta > -1,$$

where $B(\alpha, \beta)$ is the Beta function defined as $B(p, q) = \Gamma(p)\Gamma(q)/\Gamma(p + q)$. The corresponding generalized polynomial chaos, according to table 2.1, is the Jacobi-chaos. An important special case is when $\alpha = \beta = 0$, then $\epsilon(\omega)$ becomes an *uniform* random variable and the corresponding chaos becomes the Legendre-chaos (see table 2.1).

In figure 3.1 the mean-square convergence of the Jacobi-chaos solution is shown with different values of σ . It can be seen on the semi-log scale that the Jacobi-chaos solution, including the Legendre-chaos for uniform random variables, converges exponentially fast as the expansion order p increases. The exponential convergence rate is retained for large input uncertainty such as $\sigma = 0.9$, which is close to the limit of the existence of the solution ($\sigma < 1$). This is in contrast to the perturbation-based method which normally works for $\sigma < 0.1$.

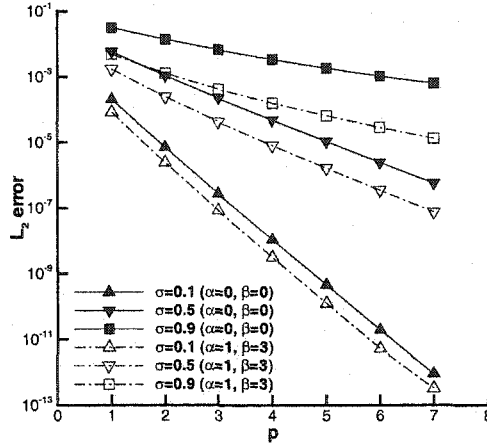


Figure 3.1: Convergence of Jacobi-chaos for the one-dimensional model problem.

Hermite-chaos and Gaussian Distribution

We now assume $\epsilon(\omega) = \sigma\xi(\omega)$ in equation (3.10), where $\xi(\omega)$ is a standard Gaussian random variable with zero mean and unit variance. The corresponding generalized polynomial chaos is the Hermite-chaos (table 2.1).

While the random input has infinite support and rigorous analysis of the existence and uniqueness of the solution is lacking to ensure $\kappa(x, \omega) > 0$ in equation (3.10) in some stochastic sense, it is intuitive to assume that the solution exists for random input with small deviation σ . In this paper, we assume $\sigma = 0.1$ and the mean-square convergence of the Hermite-chaos solution is shown in figure 3.2. Again, exponential convergence rate is achieved.

Charlier-chaos and Poisson Distribution

We now assume $\epsilon(\omega) = \sigma\xi(\omega)$ in equation (3.10) is a discrete random variable, where $\xi(\omega)$ has a Poisson distribution

$$f(\xi; \lambda) = e^{-\lambda} \frac{\lambda^\xi}{\xi!}, \quad \xi = 0, 1, 2, \dots, \lambda > 0. \quad (3.12)$$

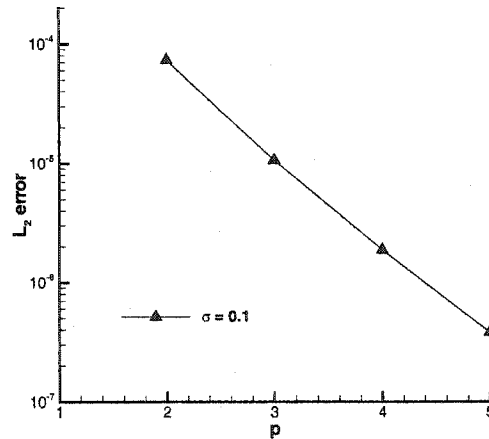


Figure 3.2: Convergence of Hermite-chaos for the one-dimensional model problem.

The corresponding generalized polynomial chaos is the Charlier-chaos (table 2.1). The exponential convergence of the Charlier-chaos expansion is shown in figure 3.3 for two different values of the parameter λ .

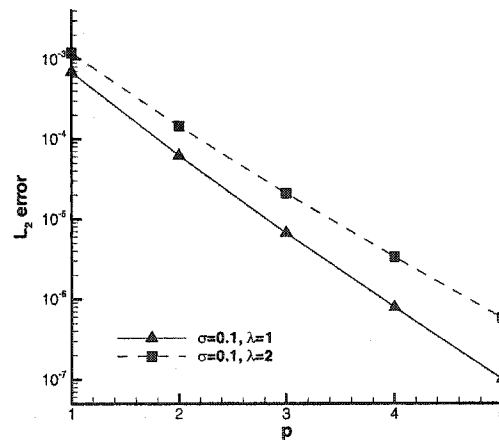


Figure 3.3: Convergence of Charlier-chaos for the one-dimensional model problem.

Krawtchouk-chaos and Binomial Distribution

In this section $\epsilon(\omega) = \sigma\xi(\omega)$ in equation (3.10) is assumed to be a discrete random variable with binomial distribution, i.e. $\xi(\omega)$ has PDF

$$f(\xi; p, N) = \binom{N}{\xi} q^\xi (1-q)^{N-\xi}, \quad 0 \leq q \leq 1, \quad \xi = 0, 1, \dots, N. \quad (3.13)$$

The corresponding generalized polynomial chaos is the Krawtchouk-chaos (table 2.1). Exponential convergence of the Krawtchouk-chaos expansion can be seen in figure 3.4 with different values of the parameters (N, q).

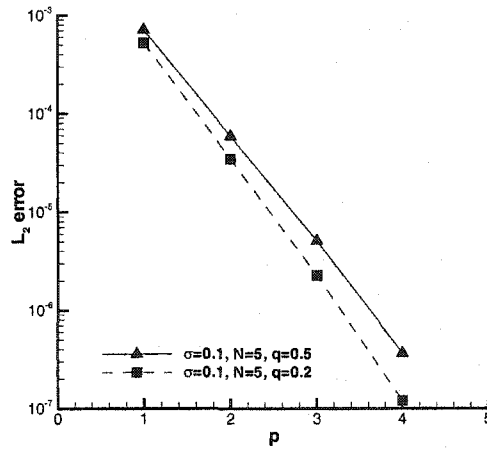


Figure 3.4: Convergence of Krawtchouk-chaos for the one-dimensional model problem.

3.2.2 Two-Dimensional Model Problem

In this section we consider the two-dimensional problem

$$\nabla \cdot [\kappa(x, y; \omega) \nabla u(x, y; \omega)] = f(x, y; \omega), \quad (x, y) \in [-1, 1] \times [-1, 1] \quad (3.14)$$

with boundary conditions

$$u(-1, y; \omega) = 1, \quad \frac{\partial u}{\partial x}(1, y; \omega) = 0, \quad u(x, -1; \omega) = 0, \quad \frac{\partial u}{\partial y}(x, 1; \omega) = 0.$$

The diffusivity $\kappa(x, y; \omega)$ and source term $f(x, y; \omega)$ are stochastic processes with certain distribution and given correlation function $C(x_1, y_1; x_2, y_2)$. The mean fields are: $\bar{\kappa}(x, y; \omega) = 1$ and $\bar{f}(x, y; \omega) = 0$. The Karhunen-Loeve decomposition is applied to the correlation function to reduce the dimensionality in the random space; the generalized polynomial chaos expansion is then applied to the solution.

The Bessel Correlation Function

The most commonly used correlation function for stochastic processes is the *exponential* function. In the one-dimensional case, it takes the form

$$C(x_1, x_2) = e^{-|x_1 - x_2|/b}, \quad (3.15)$$

where b is the correlation length. This correlation function is the result of first-order autoregression

$$\xi_t = a\xi_{t-1} + \epsilon_t, \quad a > 0, \quad (3.16)$$

where ξ_t is the random series at $t = \dots, -2, -1, 0, 1, 2, \dots$ and ϵ_t is an independent identically distributed random series. This is a *unilateral* type of scheme where the dependence is extended only in one direction, and it is the simplest realistic *time series*. For *space series*, a *bilateral* autoregression is more realistic

$$\xi_t = a\xi_{t-1} + b\xi_{t+1} + \epsilon_t, \quad (3.17)$$

where it is intuitively clear that a and b cannot be too large. It is shown that the bilateral type of scheme is not necessary in *one dimension* as it can be effectively reduced to a unilateral one [123]. Thus the exponential correlation function can be considered as the ‘elementary’ correlation in one dimension. It has been used extensively in the literature and its Karhunen-Loeve decomposition can be solved analytically [43].

In two dimensions, the exponential correlation function can be written as $C(r) = e^{-r/b}$ where r is the distance between two spatial points. This function has been also used in the literature. However, as Whittle pointed out in [123], it is necessary to introduce au-

toregression schemes with dependence in all directions for more realistic models of random series in *space*. The simplest such model is

$$\xi_{st} = a(\xi_{s+1,t} + \xi_{s-1,t} + \xi_{s,t+1} + \xi_{s,t-1}) + \epsilon_{st}, \quad (3.18)$$

where ξ_{st} is random field at grid (s, t) and ϵ_{st} is independent identically distributed random field. This model corresponds to a stochastic Laplace equation in the continuous case:

$$\left[\left(\frac{\partial}{\partial x} \right)^2 + \left(\frac{\partial}{\partial y} \right)^2 - \frac{1}{b^2} \right] \xi(x, y) = \epsilon(x, y), \quad (3.19)$$

where $\frac{1}{b^2} = 1/a - 4$. The ‘elementary’ correlation function in *two dimensions* can be solved from the above equation:

$$C(r) = \frac{r}{b} K_1 \left(\frac{r}{b} \right), \quad (3.20)$$

where K_1 is the modified Bessel function of the second kind with order 1, b scales as the correlation length and r is the distance between two points. On the other hand, the exponential correlation function $C(r) = e^{-r/b}$ in two dimensions corresponds to a rather artificial system

$$\left[\left(\frac{\partial}{\partial x} \right)^2 + \left(\frac{\partial}{\partial y} \right)^2 - \frac{1}{b^2} \right]^{\frac{3}{4}} \xi(x, y) = \epsilon(x, y). \quad (3.21)$$

It is difficult to visualize a physical mechanism which would lead to such a relation. For a detailed discussion on this subject, see [123].

In this paper, we employ (3.20) as the correlation function of κ and f . Since no analytical solution is available for the eigenvalue problem (2.12) of the Karhunen-Loeve decomposition for this correlation function, a numerical eigenvalue solver is employed. Figure 3.5 shows the distribution of the first twenty eigenvalues. Here the parameter b is set to $b = 20$. In figure 3.6 and 3.7 the eigenfunctions corresponding to the first four eigenvalues are plotted.

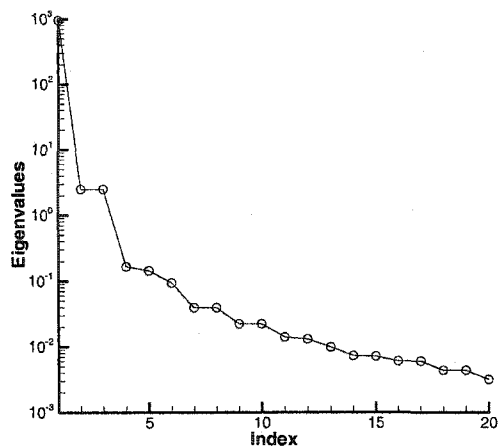


Figure 3.5: Eigenvalues of KL decomposition with Bessel correlation function (3.20), $b = 20$.

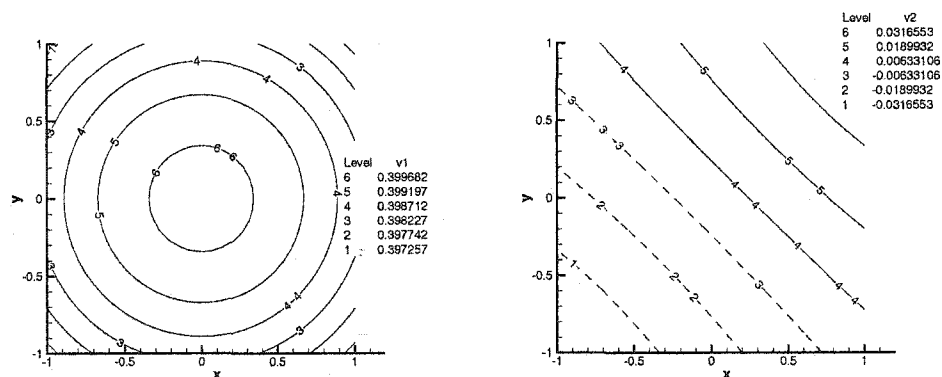


Figure 3.6: Eigenfunctions of the KL decomposition with the Bessel correlation function (3.20), $b = 20$; Left: first eigenfunction, Right: second eigenfunction. (Dashed lines denote negative values.)

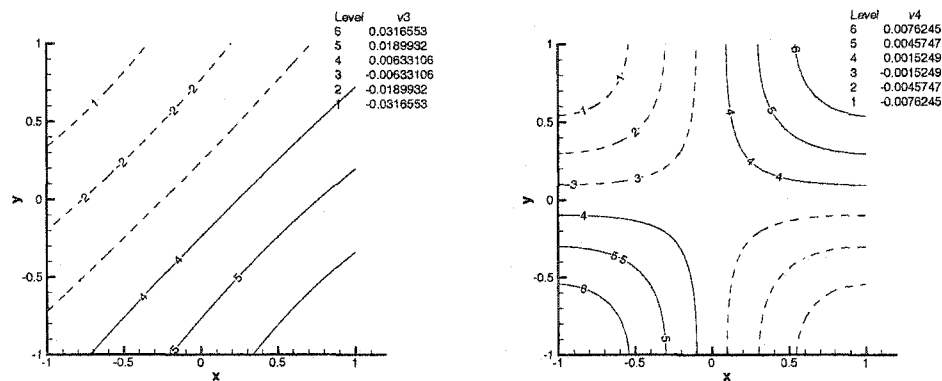


Figure 3.7: Eigenfunctions of the KL decomposition with the Bessel correlation function (3.20), $b = 20$; Left: third eigenfunction, Right: fourth eigenfunction. (Dashed lines denote negative values.)

Legendre-chaos and Uniform Distribution

In this section we assume $\kappa(x, y; \omega)$ and $f(x, y; \omega)$ are random fields resulted from the Karhunen-Loeve decomposition (2.11) of the Bessel correlation function (3.20), and with the underlying random variables having uniform distributions. For computational simplicity, we further assume k and f are fully cross-correlated. Due to the fast decay of eigenvalues as shown in figure 3.5, we choose the first four eigenmodes from the Karhunen-Loeve decomposition. This results in a four-dimensional (in random space) chaos expansion. The corresponding chaos in this case is the Legendre-chaos (table 2.1).

The spectral/ hp element method is used for spatial discretization. Specifically, an array of 5×5 elements are used in the domain and sixth-order polynomials are employed as the (spatial) expansion basis in each element. Numerical tests show that this is sufficient to resolve the solution in space. The standard deviations of the random inputs are $\sigma_\kappa = \sigma_f = 0.4$. Resolution checks in random space were conducted, and it was shown that third-order ($p = 3$) Legendre-chaos results in converged solution. For 4-dimensional chaos ($n = 4$), the total number of expansion terms is 35 (see equation (2.37)).

Since no analytical solution is available, we employ Monte Carlo simulations to validate the chaos solution. Here we conduct the Monte Carlo computation *after* the Karhunen-Loeve decomposition, i.e., we generate the random number ensemble on the reduced basis from the Karhunen-Loeve decomposition. In this way the error from generalized polyno-

mial chaos expansion is isolated, while the error introduced by the finite-term truncation of KL decomposition, which is well-understood, is excluded.

The solution profile along the horizontal centerline through the domain is considered in figure 3.8. The mean solution of Legendre-chaos and Monte Carlo simulation with different number of realizations are shown, together with the corresponding deterministic solution. A noticeable difference between the stochastic mean profile and the deterministic profile is observed. In figure 3.9 the variance of the stochastic solution along the horizontal centerline is shown. It is seen that the Monte Carlo solution converges to the chaos solution as the number of realizations increases. Good agreement is obtained with 50,000 realizations.

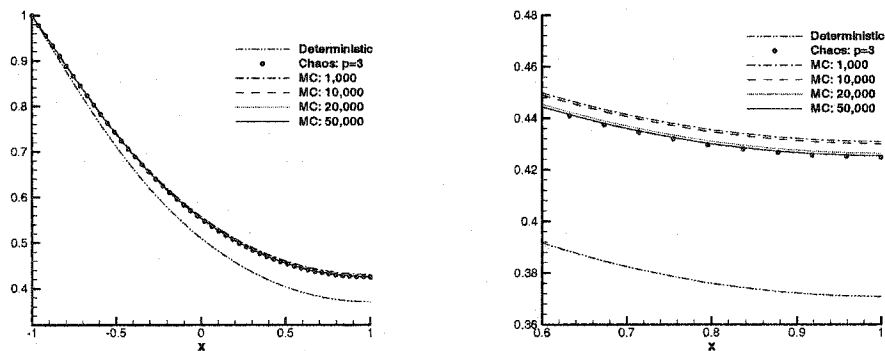


Figure 3.8: Two-dimensional model problem: uniform random distribution and Legendre-chaos; Left: Mean solution along the horizontal centerline, Right: Close-up view.

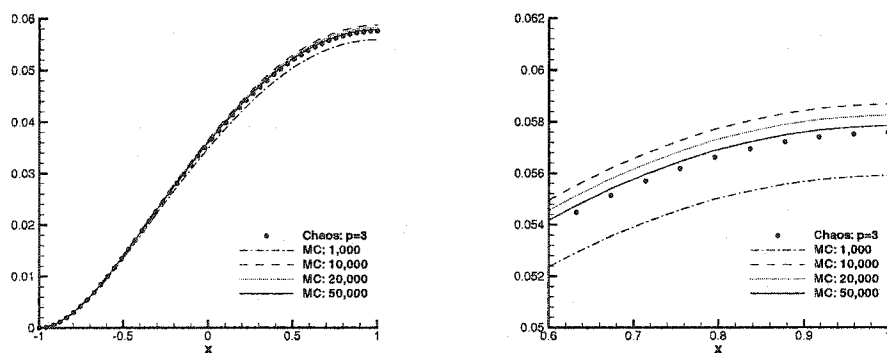


Figure 3.9: Two-dimensional model problem: uniform random distribution and Legendre-chaos; Left: Variance along the horizontal centerline, Right: Close-up view.

Similar results are obtained for other solution profiles in the domain, for example, the vertical centerline.

Hermite-chaos and Gaussian Distribution

We now assume the random field $\kappa(x, y; \omega)$ and $f(x, y; \omega)$ are Gaussian processes with $\sigma_\kappa = \sigma_f = 0.2$. All the remaining parameters are the same as the above example. The corresponding generalized polynomial chaos is the Hermite-chaos.

The same solution profiles along the horizontal centerline of the domain are shown in figure 3.10 and 3.11, for the mean solution and the variance, respectively. In this case, a fourth-order Hermite-chaos ($p = 4$) is required to obtain converged result in random space. This corresponds to a 70-term expansion from formula (2.37) for $n = 4, p = 4$. The corresponding solution of the Monte Carlo simulation converges relatively fast in this case, and for 20,000 realizations it converges to the Hermite-chaos solution.

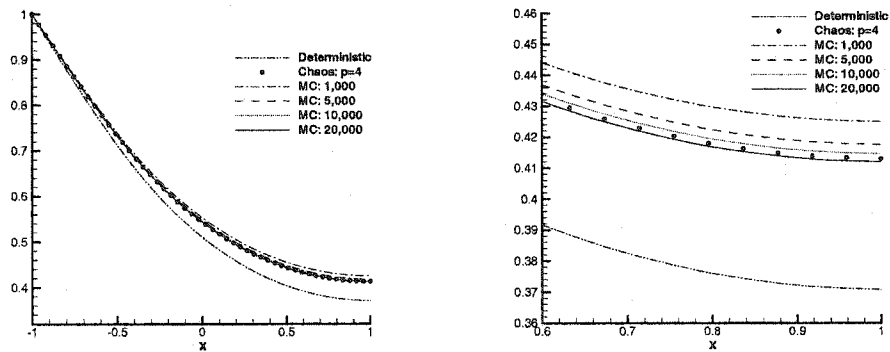


Figure 3.10: Two-dimensional model problem: Gaussian random distribution and Hermite-chaos; Left: Mean solution along the horizontal centerline, Right: Close-up view.

Charlier-chaos and Poisson Distribution

As an example of the discretely distributed random fields, we now assume the diffusivity $\kappa(x, y; \omega)$ and source term $f(x, y; \omega)$ are processes resulted from Poisson random variables in the Karhunen-Loeve decomposition (2.11), with $\sigma_\kappa = \sigma_f = 0.2$. The parameter $\lambda = 1$ as in equation (3.12).

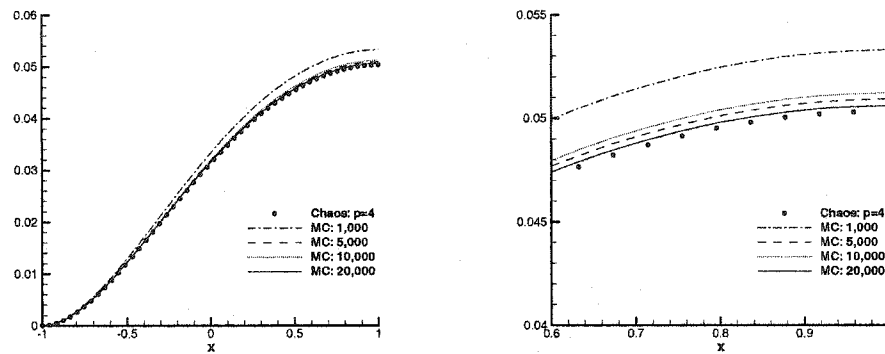


Figure 3.11: Two-dimensional model problem: Gaussian random distribution and Hermite-chaos; Left: Variance along the horizontal centerline, Right: Close-up view.

The third-order ($p = 3$) corresponding generalized chaos, the Charlier-chaos, results in resolution-independent solution in random space. The Monte Carlo solution converges to the solution of Charlier-chaos; with 100,000 realizations we obtain good agreement. The solution profiles of the mean and variance along the horizontal centerline are shown in figure 3.12 and 3.13, respectively.

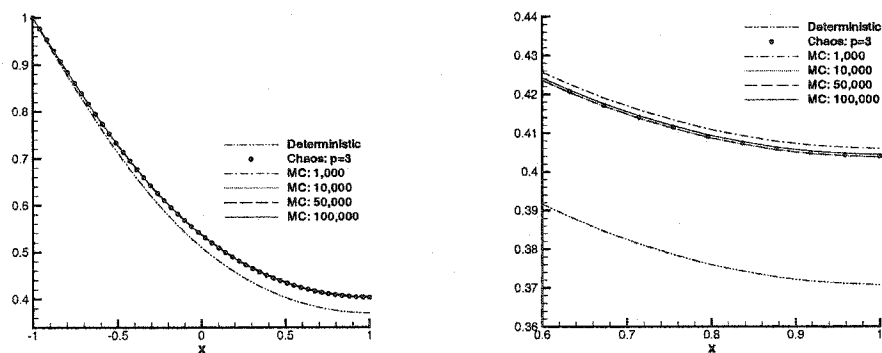


Figure 3.12: Two-dimensional model problem: Poisson random distribution and Charlier-chaos; Left: Mean solution along the horizontal centerline, Right: Close-up view.

Krawtchouk-chaos and Binomial Distribution

Finally, the random field of $\kappa(x, y; \omega)$ and $f(x, y; \omega)$ are assumed to have the binomial distributed random variables with ($N = 5, q = 0.5$) from equation (3.13) in their Karhunen-

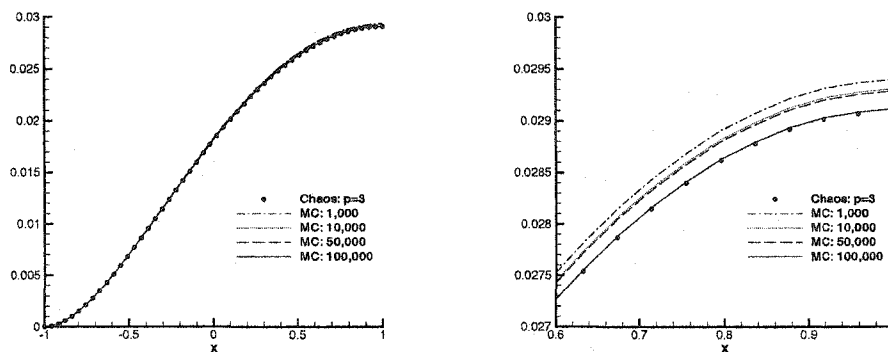


Figure 3.13: Two-dimensional model problem: Poisson random distribution and Charlier-chaos; Left: Variance along the horizontal centerline, Right: Close-up view.

Loeve expansion. The standard deviations are $\sigma_\kappa = \sigma_f = 0.2$.

Figure 3.14 shows the mean solution along the horizontal centerline of the domain, while figure 3.15 shows the variance profile. The third-order ($p = 3$) Krawtchouk-chaos is sufficient to resolve the problem in random space. On the other hand, the solution of Monte Carlo simulation converges to the chaos solution with 50,000 realizations.

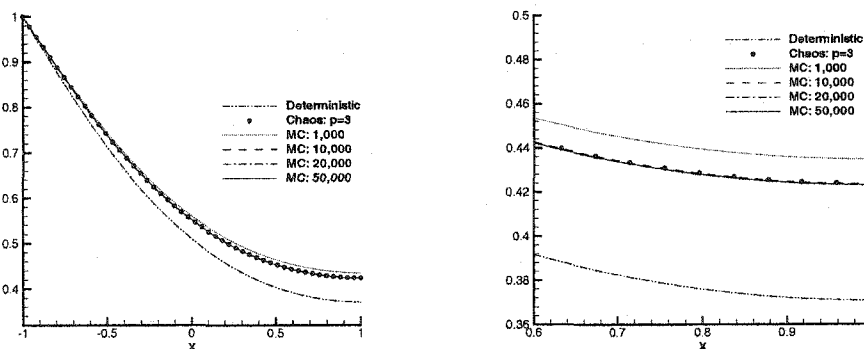


Figure 3.14: Two-dimensional model problem: binomial random distribution and Krawtchouk-chaos; Left: Mean solution along the horizontal centerline, Right: Close-up view.

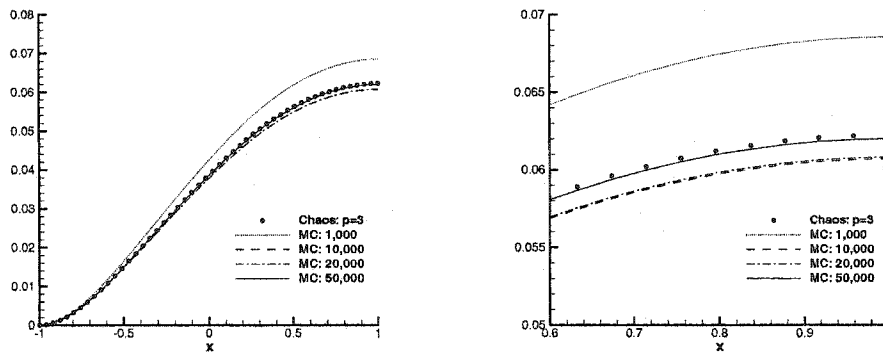


Figure 3.15: Two-dimensional model problem: binomial random distribution and Krawtchouk-chaos; Left: Variance along the horizontal centerline, Right: Close-up view.

3.2.3 Random Heat Conduction in a Grooved Channel

In this section we consider the steady state heat conduction in a grooved channel subject to uncertainties in boundary conditions and diffusivity.

$$\nabla \cdot [\kappa(x, y; \omega) \nabla u(x, y; \omega)] = 0, \quad (x, y) \in D, \quad (3.22)$$

where the computational domain D is shown in figure 3.16. The boundary of the domain consists of four segments: the top of the channel Γ_T , the bottom of the channel Γ_B , the two sides of the channel Γ_S and the boundaries of the cavity Γ_C . The diffusivity $\kappa(x, y; \omega)$ is a random field with uniformly distributed random variables in its Karhunen-Loeve decomposition, with mean field $\bar{\kappa}(x, y; \omega) = 1$ and the same Bessel correlation function as in section 3.2.2. The boundary conditions are

$$u|_{\Gamma_T} = 0, \quad u|_{\Gamma_B} = 1, \quad \left. \frac{\partial u}{\partial x} \right|_{\Gamma_S} = 0, \quad u|_{\Gamma_C} = 1 + \xi, \quad (3.23)$$

where ξ is a random variable with uniform distribution. For the spectral/ hp element solver in space, four elements are used in the domain, as shown in figure 3.16. Within each mesh, 10^{th} -order (Jacobi) polynomials are employed. In the random space, the third-order Legendre-chaos, corresponding to the uniformly distributed random inputs, is used. Resolution checks indicate that the above discretization is sufficient to resolve the problem,

both in physical and random spaces.

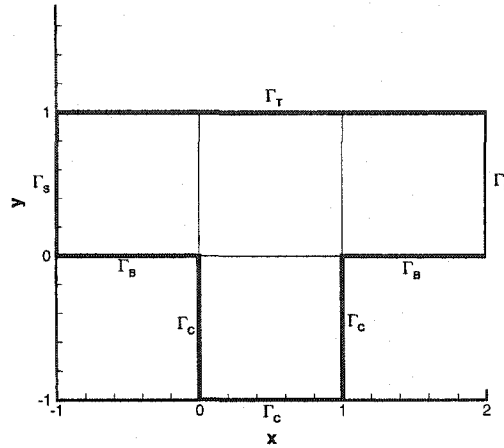


Figure 3.16: Schematic of the domain of the grooved channel

We consider two cases: the first case is when only the diffusivity κ is random, while the boundary condition along Γ_C is deterministic, i.e. $u|_{\Gamma_C} = 1$. Same as in section 3.2.2, the first four eigenmodes of the Karhunen-Loeve decomposition are employed to represent κ . This results in a four-dimensional ($n = 4$) chaos expansion. For third-order chaos ($p = 3$), a total of 35 expansion terms are needed from (2.37). In the second case, we further assume the boundary condition along the wall of cavity Γ_C is random as in (3.23), and is independent of the random field κ . This introduces one more dimension in the random space and a total of 56 expansion terms are needed for third-order chaos expansion; $n = 5$, $p = 3$ from (2.37).

In figure 3.17, the contours of the standard deviations of the solution are plotted. The solution of the first case is shown on the left, while solution of the second case on the right. In both cases, the standard deviations of the random inputs are $\sigma = 0.2$. No noticeable difference is observed between the mean solutions of the two cases, and that of the corresponding deterministic case. However, the standard deviations of the solutions are very different for the two cases. From figure 3.17, we can see that the effect of uncertainty in the diffusivity is subdominant (maximum deviation about only 0.15%). By introducing the uncertainty in boundary condition along the walls of the cavity, the

output uncertainty is greatly enhanced in the entire domain (maximum deviation about 12%), and its structure is changed; the maximum of the output uncertainty moves from the center of the channel to the lower wall of the cavity.

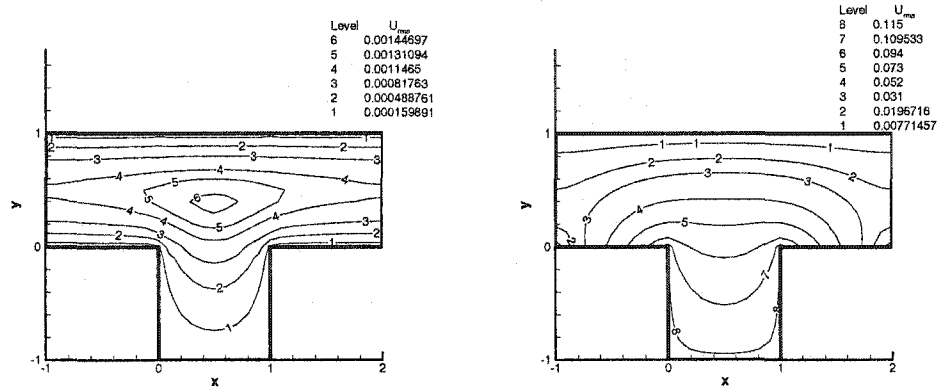


Figure 3.17: Standard deviations of heat conduction in the grooved channel; Left: solution subject to random diffusivity only; Right: solution subject to random diffusivity and random boundary conditions.

3.3 Problems with Random Boundary: Roughness

In this section we consider problems with random boundary. Such problems are important subjects in wave scattering theory, flow drag reduction, etc., where the roughness of the boundary has non-negligible effect. Here, we propose an approach based on a mapping technique that transforms the problem in a random domain to a problem with random coefficients in a fixed deterministic domain. We illustrate the method via a model elliptic problem.

Consider a two-dimensional elliptic equation in a domain with random boundary,

$$\begin{cases} \nabla^2 u(x, y; \omega) = f(x, y), & (x, y) \in \Omega(\omega) \\ u(x, y; \omega) = g(x), & (x, y) \in \partial\Omega(\omega). \end{cases} \quad (3.24)$$

Here for simplicity, we assume the source term and boundary condition are deterministic. In the previous sections, randomness in such terms has been dealt with. The physical domain $\Omega(\omega)$ is random due to the uncertainty in the location of boundary $\partial\Omega(\omega)$.

Our approach is to define a random mapping $H(\omega)$ between the random domain $\Omega(\omega)$ and a *deterministic* domain Ω' whose boundary is at the mean location of the original random domain, i.e., $\partial\Omega' = \langle \partial\Omega(\omega) \rangle$. The map takes the form

$$H(\omega) := \{\Omega(\omega) \rightarrow \Omega', \text{ s.t. } \partial\Omega' = \langle \partial\Omega(\omega) \rangle\}. \quad (3.25)$$

Correspondingly, the original governing differential equation is transformed, with its Jacobians being functions of the mapping $H(\omega)$. Hence, the uncertainty in the random domain is translated into the Jacobians of the governing equation, which is now in a fixed domain. The generalized polynomial chaos can be readily applied to solve the transformed problem.

To illustrate the approach, we employ the domain in figure 3.18, where only one boundary (y_b) is uncertain. We denote (x', y') the coordinates in the transformed domain Ω' whose boundary (y'_b) is at the mean location of y_b . The mapping $H(\omega)$ then takes the form

$$x' = x, \quad y' = h(y(\omega)), \quad (3.26)$$

where the function $h(y)$ depends on the specific form of $y_b(\omega)$ to ensure $y'_b = \langle y_b \rangle$. The governing equation (3.24) is transformed to

$$\frac{\partial^2 u}{\partial x'^2} + J^2(\omega) \frac{\partial^2 u}{\partial y'^2} = f, \quad (3.27)$$

where the Jacobian $J(\omega) = dy'/dy$.

Equation (3.27) is an elliptic equation with uncertain coefficient $J(\omega)$. Similar procedure as in section 3.1 can be applied. As an illustrative example, here we assume the domain is $(x, y) \in [0, 1] \times [0, 1 + \sigma\xi]$, where $\xi \sim U(-1, 1)$ is a uniform random variable. The boundary conditions are $u(x, 0) = 0$, $u(x, 1 + \sigma\xi) = 1$, and periodic in x -direction. In figure 3.19, the mean-square error of the Legendre-chaos solution is shown with $\sigma = 0.1$, and we observe exponential convergence of the error as the order of expansion increases.

Further research based on this preliminary example is currently ongoing, where more realistic models for rough surfaces, i.e., stochastic processes with short correlation length, are considered.

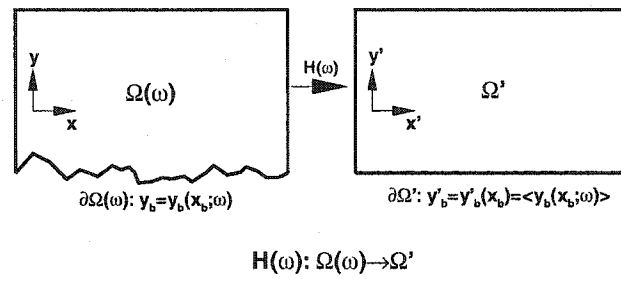


Figure 3.18: Schematic of the mapping of a uncertain domain.

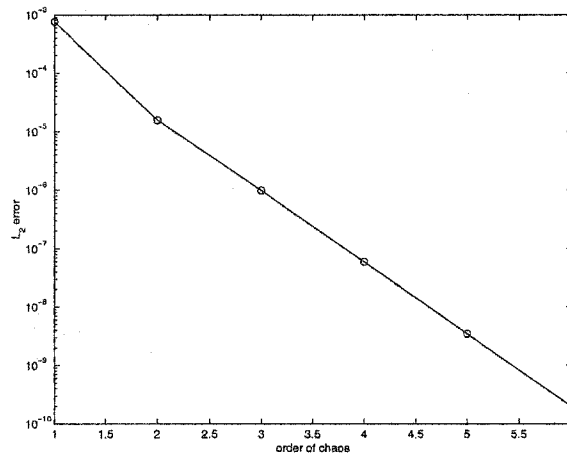


Figure 3.19: Mean square error convergence for a model problem with uncertain boundary.

Chapter 4

Parabolic Equations

In this chapter we consider parabolic equations subject to uncertain inputs. We first focus on a simplified system with constant random diffusivity, and study the well-posedness of the semi-discrete system resulted from generalized polynomial chaos expansion (section 5.1 and 5.2). In section 5.3, we demonstrate the applications to unsteady heat transfer problems where the heat capacity and media conductivity are modeled as random processes. A number of papers have addressed this problem, using perturbation methods [28, 51, 52, 60] and the classical Hermite polynomial chaos in one physical dimension [40].

4.1 Stochastic Formulation with Uncertain Diffusivity

We consider the time-dependent diffusion problem with constant diffusivity

$$\frac{\partial u(x, t)}{\partial t} = \kappa \nabla^2 u(x, t), \quad u(x, t_0) = f(x), \quad (4.1)$$

where $(x, t) \in R^d \times R$ with $d = 1, 2, 3$ and $t \geq t_0$.

We define the well-posedness of problem (4.1) following the classical deterministic analysis (cf. [48]).

Definition 4.1 (Deterministic well-posedness). *The problem (4.1) is well-posed if, for every t_0 and every $f \in C^\infty(x)$:*

- *There exists a unique solution $u(x, t) \in C^\infty(x, t)$, which is 2π -periodic in every space*

dimension, and

- There are constants α and K , independent of $f(x)$ and t_0 , such that $\|u(x, t)\| \leq Ke^{\alpha(t-t_0)}\|u(x, t_0)\|$, where $\|\cdot\|$ denotes certain norm in space.

It is easy to show that (4.1) is well-posed if and only if $\kappa \geq 0$.

Hereafter, we will assume κ is a random variable and is the only random input in problem (4.1):

$$\kappa(\omega) = \mu + \sigma\xi, \quad \mu, \sigma > 0, \quad (4.2)$$

where μ is the mean value of κ . Also, ξ is a random variable with zero mean and certain probability density function (PDF), and σ scales as its corresponding standard deviation.

The problem (4.1) becomes stochastic, i.e.,

$$\frac{\partial u(x, t; \omega)}{\partial t} = \kappa(\omega)\nabla^2 u(x, t; \omega), \quad u(x, t_0; \omega) = f(x), \quad (4.3)$$

with $(x, t) \in \mathbb{R}^d \times \mathbb{R}$ ($d = 1, 2, 3$) and $\omega \in \Omega$ where Ω is a properly defined probability space. We call this problem well-posed if its every realizations is well-posed in the deterministic sense.

Definition 4.2 (Stochastic well-posedness). *Problem (4.3) is (strongly) well-posed if, for every $\omega \in \Omega$, it is well-posed according to definition (4.1).*

Based on this definition, it is obvious that problem (4.3) is well-posed if $\kappa(\omega) \geq 0$ for all $\omega \in \Omega$.

4.2 Well-posedness of Generalized Polynomial Chaos Expansion

To solve (4.3) via generalized polynomial chaos, the random quantities are expanded as

$$u(x, t; \omega) = \sum_{k=0}^M u_k(x, t)\Phi_k(\xi(\omega)), \quad \kappa(\omega) = \sum_{k=0}^M \kappa_k\Phi_k(\xi(\omega)). \quad (4.4)$$

Since the only random input is the random variable ξ from κ , the polynomial chaos expansion is one-dimensional, and M is the highest order of the expansion. The type of generalized polynomial chaos $\{\Phi_k(\xi(\omega))\}$ will be specified according to the random input $\kappa(\omega)$. Upon substituting into (4.3), we obtain

$$\sum_{k=0}^M \frac{\partial u_k(x, t)}{\partial t} \Phi_k(\xi) = \sum_{i=0}^M \sum_{j=0}^M \kappa_i \nabla^2 u_j(x, t) \Phi_i(\xi) \Phi_j(\xi). \quad (4.5)$$

A Galerkin projection is employed to ensure the truncation error due to the finite-term expansion is orthogonal to the finite-dimensional space spanned by the bases $\{\Phi_k(\xi), k = 0, \dots, M\}$, thus

$$\frac{\partial u_k(x, t)}{\partial t} = \frac{1}{\langle \Phi_k^2 \rangle} \sum_{i=0}^M \sum_{j=0}^M \kappa_i \nabla^2 u_j(x, t) e_{ijk}, \quad k = 0, 1, \dots, M, \quad (4.6)$$

where $e_{ijk} = \langle \Phi_i \Phi_j \Phi_k \rangle$.

The system of the coupled partial differential equations (4.6) can be rewritten as

$$\frac{\partial u_k(x, t)}{\partial t} = \sum_{j=0}^M b_{jk} \nabla^2 u_j(x, t), \quad \forall k = 0, 1, \dots, M, \quad (4.7)$$

where

$$b_{jk} = \frac{1}{\langle \Phi_k^2 \rangle} \sum_{i=0}^M \kappa_i e_{ijk}. \quad (4.8)$$

This equation can also be written in matrix form

$$\frac{\partial U(x, t)}{\partial t} = B_{M+1}^T \nabla^2 U(x, t), \quad (4.9)$$

where

$$U(x, t) = [u_0, u_1, \dots, u_M]^T, \quad B_{M+1} = [b_{jk}]_{(M+1) \times (M+1)}. \quad (4.10)$$

Here the superscript T denotes the matrix transpose.

We further assume that the random diffusivity (4.2) is a continuous random variable

whose generalized polynomial chaos expansion takes the simple form

$$\kappa_0 = \mu, \quad \kappa_1 = \sigma, \quad \kappa_k = 0, \quad \text{for } 2 \leq k \leq M. \quad (4.11)$$

This expansion can be realized if κ is a Gaussian, beta, or gamma random variable, and the corresponding Hermite-chaos, Jacobi-chaos, or Laguerre-chaos is employed, respectively.

Lemma 4.1. *Assume the random diffusivity (4.2) has the generalized polynomial chaos expansion in the form of (4.11), then the $(M+1) \times (M+1)$ matrix B_{M+1}^T defined in (4.10) has $(M+1)$ real and distinct eigenvalues.*

Proof. Since the eigenvalues of a square matrix are the same as those of its transpose, it suffices to study the eigenvalues of B_{M+1} . Given the form of expansion of κ (4.11), the entries of matrix B_{M+1} are, according to (4.8),

$$b_{jk} = \frac{1}{\langle \Phi_k^2 \rangle} \sum_{i=0}^M \kappa_i e_{ijk} = \frac{1}{\langle \Phi_k^2 \rangle} (\mu \cdot e_{0jk} + \sigma \cdot e_{1jk}). \quad (4.12)$$

From the definition of polynomial chaos, $e_{0jk} = \langle \Phi_0 \Phi_j \Phi_k \rangle = \langle \Phi_j^2 \rangle \delta_{jk}$, and

$$e_{1jk} = \langle \Phi_1 \Phi_j \Phi_k \rangle = \int \xi \Phi_j(\xi) \Phi_k(\xi) w(\xi) d\xi.$$

By using the three-term recurrence relation (2.5), this integral can be evaluated as

$$\begin{aligned} e_{1jk} &= - \int (b_j \Phi_{j+1}(\xi) + \gamma_j Q_j(\xi) + c_j Q_{j-1}(\xi)) Q_k(\xi) w(\xi) d\xi \\ &= -(b_j \delta_{j+1,k} + \gamma_j \delta_{j,k} + c_j \delta_{j-1,k}) \langle \Phi_k^2 \rangle. \end{aligned}$$

Substituting these results back in (4.12), we obtain

$$b_{jk} = (\mu - \sigma \gamma_j) \delta_{j,k} - \sigma b_j \delta_{j+1,k} - \sigma c_j \delta_{j-1,k}. \quad (4.13)$$

Hence the $(M + 1) \times (M + 1)$ matrix B_{M+1} is a tridiagonal matrix

$$B_{M+1} = \begin{bmatrix} \mu - \sigma\gamma_0 & -\sigma b_0 & 0 & \cdots & \cdots & \cdots & 0 \\ -\sigma c_1 & \mu - \sigma\gamma_1 & -\sigma b_1 & \cdots & \cdots & \cdots & 0 \\ \vdots & \ddots & \ddots & \ddots & \vdots & \vdots & \vdots \\ 0 & \cdots & -\sigma c_j & \mu - \sigma\gamma_j & -\sigma b_j & \cdots & 0 \\ \vdots & \cdots & \cdots & \ddots & \ddots & \ddots & \vdots \\ \vdots & \cdots & \cdots & \cdots & \ddots & \ddots & \vdots \\ 0 & \cdots & \cdots & \cdots & 0 & -\sigma c_M & \mu - \sigma\gamma_M \end{bmatrix}.$$

The eigenvalues of this matrix are determined by solving its determinant equation

$$S_{M+1} := \det(B_{M+1} - \lambda I) = 0, \quad (4.14)$$

where I is the $(M + 1) \times (M + 1)$ identity matrix and λ is the eigenvalue. Upon expanding S_{M+1} , we obtain

$$S_{M+1} = [(\mu - \lambda) - \sigma\gamma_M] S_M - \sigma^2 c_M b_{M-1} S_{M-1}, \quad M \geq 0. \quad (4.15)$$

This defines a three-term recurrence formula for $\{S_M\}$. By letting $\mu - \lambda = x$, $A_M = 1$, $B_M = -\sigma\gamma_M$, and $C_M = \sigma^2 c_M b_{M-1}$, this recurrence relation takes the same form as (2.4). By defining $S_0 = 1$ and $S_{-1} = 0$, all the conditions in Favard's theorem (2.1) are satisfied when $\sigma > 0$. Hence $\{S_M\}$ is an orthogonal polynomial system in terms of $(\mu - \lambda)$. From the well-known theory of orthogonal polynomials, $S_{M+1}(\mu - \lambda)$ has $(M + 1)$ real and distinct zeros at $\{z_i, i = 0, \dots, M\}$, i.e. (4.14) has $(M + 1)$ real and distinct roots at $\mu - \lambda = z_i, i = 0, \dots, M$. Thus, matrix B_{M+1} has $(M + 1)$ real and distinct eigenvalues

$$\lambda_i = \mu - z_i, i = 0, \dots, M. \quad \square$$

Because the matrix B_{M+1}^T has $(M+1)$ real and distinct eigenvalues, it has a full set of independent eigenvectors. We can diagonalize this matrix $S^{-1}B_{M+1}^T S = \Lambda_{M+1}$, where S is the eigenvector matrix of B_{M+1}^T and Λ_{M+1} is the diagonal matrix whose entries are the eigenvalues of B_{M+1}^T . (All matrices here are of size $(M+1) \times (M+1)$.) Equation (4.9) can be decoupled as

$$\frac{\partial W(x, t)}{\partial t} = \Lambda_{M+1} \nabla^2 W(x, t), \quad W(x, t) = S^{-1}U(x, t), \quad (4.16)$$

or, in index form

$$\frac{\partial w_k(x, t)}{\partial t} = \lambda_k \nabla^2 w_k(x, t), \quad k = 0, \dots, M, \quad (4.17)$$

where $W(x, t) = [w_0, w_1, \dots, w_M]^T = S^{-1}U(x, t)$.

Equations (4.17) are a set of decoupled deterministic equations. This system is well-posed if $\lambda_k \geq 0$, for all $k = 0, 1, \dots, M$, i.e. (4.9) is well-posed if all the eigenvalues of B_{M+1}^T are non-negative.

Now we examine the well-posedness of different generalized polynomial chaos expansions.

4.2.1 Gaussian Input and Hermite-chaos

Theorem 4.1 (Hermite-chaos). *Let the M^{th} -order Hermite-chaos be employed to derive the system (4.9), and assume that diffusivity $\kappa = \mu + \sigma\xi$ is a Gaussian random variable and has its Hermite-chaos expansion of the form (4.11), where ξ is a standard Gaussian random variable with zero mean and unit variance. Then for any given $\mu, \sigma > 0$, there exists an integer $N > 0$ such that for expansion order $M \geq N$, at least one of the eigenvalues of B_{M+1}^T is negative.*

Proof. By using the recurrence relation of Hermite polynomials, the S_{M+1} in (4.15) takes the form

$$S_{M+1} = (\mu - \lambda)S_M - \sigma^2(M-1)S_{M-1}, \quad M \geq 0. \quad (4.18)$$

Together with $S_{-1} = 0, S_0 = 1$, this three-term recurrence relation defines a system of

scaled Hermite orthogonal polynomials

$$S_M(\lambda) = \sigma^M H_M \left(\frac{\mu - \lambda}{\sigma} \right), \quad M \geq 0,$$

where $\{H_M(x)\}$ are the regular Hermite polynomials defined in (A.1.1) with recurrence relation (A.6) (see Appendix A). As shown in Appendix B, the largest zero of $H_n(x)$, denoted as z_{\max} , satisfies $z_{\max} > \sqrt{n-1}$ (see (B.3)). Thus, the largest root of $S_{M+1} = 0$ satisfies

$$\frac{\mu - \lambda_{\min}}{\sigma} > \sqrt{M}.$$

It follows that the smallest eigenvalue satisfies $\lambda_{\min} < \mu - \sigma\sqrt{M}$. Let $N = \text{ceil}(\mu/\sigma)^2$ where $\text{ceil}(x)$ is the ceiling function, then for $M \geq N$, $\lambda_{\min} < 0$, i.e. at least one of the eigenvalues of B_{M+1}^T is negative. \square

This theorem indicates that, for given $\mu, \sigma > 0$, there exists a ‘critical order’ N , such that for Hermite-chaos expansion of orders higher than N , the system (4.9) becomes ill-posed; for orders lower than N , it is well-posed. The proof of Theorem 4.1 gives us directly the following corollary on the upper bound of this critical order.

Corollary 4.1 (Upper bound). *Under the same assumptions of Theorem 4.1, for any given $\mu, \sigma > 0$, there exists a critical expansion order*

$$N^c = \text{ceil} \left[\left(\frac{\mu}{\sigma} \right)^2 \right], \quad (4.19)$$

such that for expansion order $M \geq N^c$, at least one eigenvalue of the matrix B_{M+1}^T is negative.

We now estimate the lower bound of the critical order N .

Corollary 4.2 (Lower bound). *Under the same assumptions of Theorem 4.1, for any given $\mu, \sigma > 0$, there exists a critical expansion order*

$$N_c = \text{floor} \left[\frac{\mu^2}{8\sigma^2} \left(1 + \sqrt{1 - 16 \frac{\sigma^2}{\mu^2}} \right) \right], \quad (4.20)$$

such that for expansion order $M \leq N_c$, all eigenvalues of the matrix B_{M+1}^T are non-negative.

Proof. For Hermite polynomial $H_n(x)$, the largest zero satisfies $z \leq 2(n-1)/\sqrt{n-2}$ (see B.4). Correspondingly, the largest root of $S_{M+1} = 0$ satisfies

$$\frac{\mu - \lambda_{\min}}{\sigma} \leq \frac{2M}{\sqrt{M-1}}.$$

Thus, the smallest eigenvalue satisfies $\lambda_{\min} \geq \mu - 2\sigma M/\sqrt{M-1}$. The condition $\lambda_{\min} \geq 0$ defines a quadratic inequality in term of M . It is easy to show that for $M \leq N_c$ where N_c is defined in (4.20), the inequality is always satisfied. Hence $\lambda_{\min} \geq 0$, and all the eigenvalues of B_{M+1}^T are non-negative. \square

A numerical experiment is conducted to validate these two estimates. Specifically, the mean value is fixed at $\mu = 1$. The order of Hermite-chaos expansion M is increased and the eigenvalues of B_{M+1}^T are evaluated. The numerical critical expansion order is obtained once the smallest eigenvalue of B_{M+1}^T is negative. In figure 4.1, this critical order is plotted, together with the upper and lower bound estimates, for various values of σ . It is seen that the numerical critical order stays within the two bounds as expected. Note that in deriving the lower bound (4.20), a sharp estimate for the largest zero of Hermite polynomials was employed. Hence, the lower bound of the critical order is a sharp estimate, and the numerical estimate approaches it quickly for $N \gg 1$.

4.2.2 Beta Input and Jacobi-chaos

Theorem 4.2 (Jacobi-chaos). *Let the M^{th} -order Jacobi-chaos with parameter $\alpha, \beta > -1$ be employed to derive the system (4.9), and assume that diffusivity $\kappa = \mu + \sigma\xi$ is a beta random variable and has its Jacobi-chaos expansion in the form of (4.11), where $\xi \sim Be(\alpha, \beta)$ is a beta random variable defined in domain $(-1, 1)$ with probability density function (A.17). Then all the eigenvalues of B_{M+1}^T are non-negative if $\sigma \leq \mu$.*

Proof. Upon using the coefficients of the recurrence relation for Jacobi polynomials (A.18),

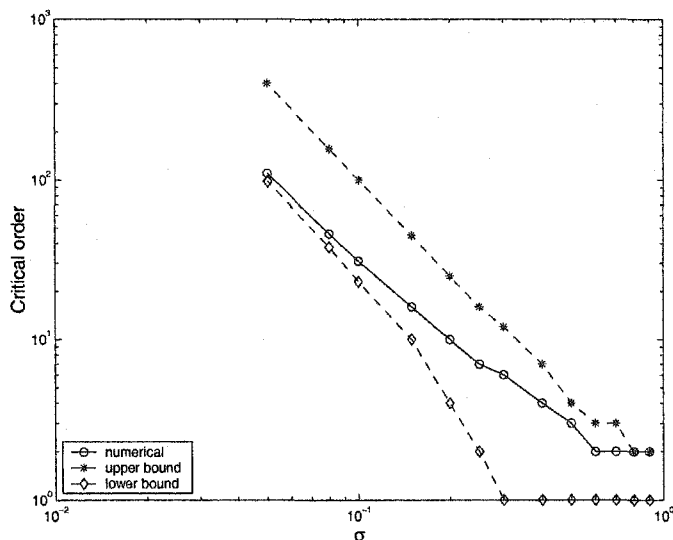


Figure 4.1: Critical expansion order (N) versus σ for the well-posedness of Hermite-chaos ($\mu = 1$).

equation (4.15) becomes, for $M \geq 0$,

$$S_{M+1} = \left[(\mu - \lambda) - \sigma \frac{\beta^2 - \alpha^2}{(2M + \alpha + \beta)(2M + \alpha + \beta + 2)} \right] S_M - \sigma^2 \frac{4M(M + \alpha)(M + \beta)(M + \alpha + \beta)}{(2M + \alpha + \beta - 1)(2M + \alpha + \beta)^2(2M + \alpha + \beta + 1)} S_{M-1}.$$

By comparing with the normalized recurrence relation of Jacobi polynomials (A.19), we observe that the above recurrence relation defines a set of scaled Jacobi polynomials, i.e.

$$S_M(\lambda) = \sigma^M p_M \left(\frac{\mu - \lambda}{\sigma} \right),$$

where $\{p_M(x)\}$ are the normalized Jacobi polynomials defined in (A.19). Since the zeros of the Jacobi polynomials as defined in this paper are in $[-1, 1]$, the roots of $S_{M+1} = 0$ (4.14) satisfy,

$$\left| \frac{\mu - \lambda}{\sigma} \right| \leq 1$$

It is easy to show that for $\sigma \leq \mu$, all eigenvalues satisfy $\lambda \geq 0$. \square

4.2.3 Gamma Input and Laguerre-chaos

Theorem 4.3 (Laguerre-chaos). *Let the M^{th} -order Laguerre-chaos with parameter $\alpha > -1$ be employed to derive the system (4.9), and assume that diffusivity $\kappa = \mu \pm \sigma\xi$ is a gamma random variable and has its Laguerre-chaos expansion in form of*

$$\kappa_0 = \mu, \quad \kappa_1 = \mp\sigma, \quad \kappa_k = 0, \quad \text{for } 2 \leq k \leq M, \quad (4.21)$$

where ξ is a gamma random variable with zero mean and probability density function (A.10). Then,

- if $\kappa = \mu + \sigma\xi$, all the eigenvalues of B_{M+1}^T are positive;
- if $\kappa = \mu - \sigma\xi$, there exists an integer $N > 0$ such that for expansion order $M \geq N$, at least one of the eigenvalues of B_{M+1}^T is negative.

Proof. First note that the switch of sign in the expansion of κ in (4.21) is due to the definition of Laguerre polynomials, i.e. the leading coefficients of the odd order polynomials are negative. For $\kappa = \mu \pm \sigma\xi$, the recurrence relation (4.15) for S_{M+1} becomes

$$S_{M+1} = [(\mu - \lambda) \mp \sigma(2M + \alpha + 1)] S_M - \sigma^2 M(M + \alpha) S_{M-1}, \quad M \geq 0.$$

Comparing with the normalized recurrence relation for Laguerre polynomials (A.12), we observe that the above recurrence relation defines a set of scaled Laguerre polynomials, i.e.

$$S_M(\lambda) = (\mp\sigma)^M q_M \left(\frac{\mu - \lambda}{\mp\sigma} \right),$$

where $\{q_M(x)\}$ are the normalized Laguerre polynomials defined in (A.12). The zeros of Laguerre polynomials are non-negative. Thus

$$\frac{\mu - \lambda}{\mp\sigma} \geq 0.$$

- If $\kappa = \mu + \sigma\xi$, then $(\mu - \lambda_{\min})/(-\sigma) \geq 0$. It follows immediately that $\lambda_{\min} \geq \mu > 0$. Hence all $\lambda \geq 0$.

- If $\kappa = \mu - \sigma\xi$, then $(\mu - \lambda)/\sigma \geq 0$. It is obvious that λ cannot be bounded from below since the largest zero of Laguerre polynomial z_{\max} grows unbounded as the order increases. Specifically, $z_{\max} > n + \alpha + 1$, where n is the order of the Laguerre polynomial (cf. [117]). Thus

$$\frac{\mu - \lambda_{\min}}{\sigma} > 2M + \alpha - 1.$$

Let $N = \text{ceil}[(\mu/\sigma - \alpha + 1)/2]$, then for $M \geq N$, $\lambda_{\min} < 0$, i.e. at least one eigenvalue of B_{M+1}^T is negative.

□

Similarly as the Hermite-chaos expansion under Gaussian assumption, there exists a critical order for Laguerre-chaos expansion when the random input takes the form $\kappa = \mu - \sigma\xi$. Above this critical order, the expanded system is ill-posed; and below it, the system is well-posed.

Corollary 4.3 (Upper and lower bounds for Laguerre-chaos). *Let the M^{th} -order Laguerre-chaos with parameter $\alpha > -1$ be employed to derive the system (4.9), and assume the diffusivity $\kappa = \mu - \sigma\xi$ is a gamma random variable and has its Laguerre-chaos expansion in form of*

$$\kappa_0 = \mu, \quad \kappa_1 = \sigma, \quad \kappa_k = 0, \quad \text{for } 2 \leq k \leq M, \quad (4.22)$$

where ξ is a gamma random variable with zero mean. Then, for any given $\mu, \sigma > 0$,

- there exists a critical expansion order

$$N^c = \text{ceil} \left[\frac{1}{2} \left(\frac{\mu}{\sigma} - \alpha + 1 \right) \right] \quad (4.23)$$

such that for expansion order $M \geq N^c$, at least one eigenvalue of the matrix B_{M+1}^T is negative.

- there exists another critical expansion order

$$N_c = \text{floor} \left[\frac{1}{2} \left(\frac{s^2 + \alpha^2 - 1/4}{2s} - \alpha - 1 \right) \right], \quad (4.24)$$

where $s = \mu/\sigma$, such that for expansion order $M \leq N_c$, all eigenvalues of the matrix B_{M+1}^T are non-negative.

Proof. The proof for the upper bound (4.23) follows immediately from the proof of Theorem 4.3. For the lower bound, we use the classical analysis on the estimate of the largest root of Laguerre polynomial (cf. [117])

$$z_{\max} < 2n + \alpha + 1 + \left[(2n + \alpha + 1)^2 - \alpha^2 + \frac{1}{4} \right]^{1/2}$$

By substituting $(\mu - \lambda_{\min})/\sigma$ for z_{\max} and setting $\lambda_{\min} \geq 0$, one obtains (4.24) from the resulting inequality. \square

Again we examine the two estimates of the upper and lower bounds by numerical experiment. In figure 4.2, the numerical critical expansion order is plotted, together with the upper and lower bounds from (4.23) and (4.24). It is seen that the numerical result stays within the two bounds, and approaches the lower bound for large N as the lower bound is the result of a sharper estimate of the largest zero of Laguerre polynomials.

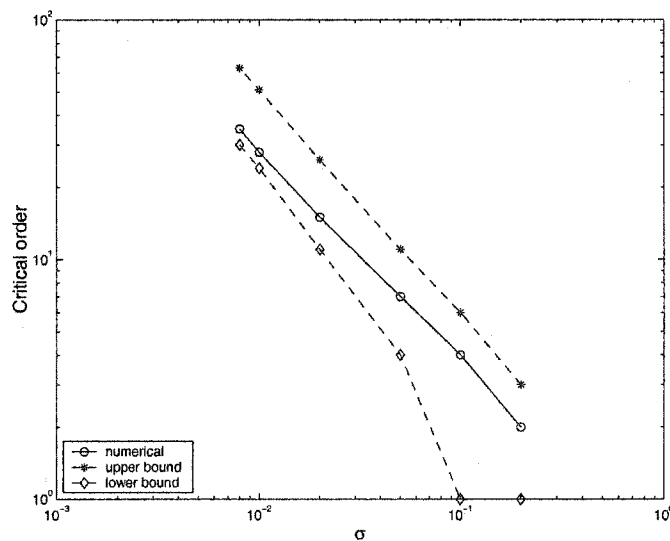


Figure 4.2: Critical expansion order (N) versus σ for the well-posedness of Laguerre-chaos ($\mu = 1, \alpha = 0$).

4.2.4 Discussion

The diffusivity κ in our model problem (4.3) is a physical quantity. For any realistic material, it is strictly non-negative. The mathematical requirement for well-posedness, i.e. $\kappa \geq 0$, is merely a manifestation of the physics. When κ is assumed to be random, the condition has to be satisfied for all realizations, i.e. $\kappa(\omega) \geq 0$ for all $\omega \in \Omega$.

For many applications in practice, when the actual distribution of a random quantity is unclear, a Gaussian distribution is often employed. This, however, may pose a mathematical challenge if the underlying physical quantities are ‘bounded’. For example, in the diffusion problem with random diffusivity considered here, if one assumes $\kappa \sim N(\mu, \sigma^2)$ is a Gaussian random variable with certain mean value μ and standard deviation σ , then it allows $\kappa < 0$ with non-zero probability for any $\mu, \sigma > 0$. This contradicts the condition on well-posedness for the diffusion problem and renders the problem unsolvable mathematically. Consequently, the Hermite-chaos expansion becomes ill-posed for expansion order higher than a critical value which depends on μ and σ . In other words, under the assumption of $\kappa \sim N(\mu, \sigma^2)$, one cannot completely resolve problem (4.3) by using Hermite-chaos with arbitrarily high order expansions. This difficulty due to Gaussian assumption has been realized for the diffusion problem and in practice the lognormal distribution is often employed to avoid the negative tail.

It should be emphasized that the ill-posedness is *not* an intrinsic drawback of the Hermite-chaos. It is a direct result of the inappropriate Gaussian assumption made on κ . In fact, in this case, the Hermite-chaos accurately models the problem (4.3), which employs the inaccurate assumption on κ . The difficulty arises from the fact that Gaussian has a long tail on the negative side which allows negative values of κ with non-zero probability. Similarly, if κ is modeled as a gamma random variable with the tail on the negative side, the corresponding Laguerre-chaos becomes ill-posed above the critical expansion order, as shown in Theorem 4.3.

In practice, observation data or experimental measurements often suggest that the distribution of a random input resembles Gaussian, but physical consideration or mathematical assumption requires that it has bounded support, i.e. no long tails. In this case, the common approach is to simply ‘truncate’ the support of a Gaussian distribution and

re-normalize it to ensure the total probability is unity. An alternative is to use a finite-term Jacobi-chaos expansion to approximate Gaussian distribution. This approach was first proposed in [133], and is included in Appendix C of this thesis.

4.3 Applications to Transient Heat Conduction

The objective of this section is to model transient heat conduction with uncertain inputs by the generalized polynomial chaos expansion. In particular, we focus on media with random heat conductivity and capacity.

4.3.1 Algorithm

The unsteady stochastic heat equation for a spatially varying medium, in the absence of convection, is

$$c(x; \omega) \frac{\partial T}{\partial t} = \nabla \cdot [\mathbf{k}(x; \omega) \nabla T] + f(t, x; \omega) \quad (x, \omega) \in D \times \Omega \quad (4.25)$$

subjected to the following initial and boundary conditions

$$T(0, x; \omega) = T_0(x, \omega), \quad (4.26)$$

$$T(t, x; \omega) = T_b, \quad x \in \partial D_1; \quad -\mathbf{k} \frac{\partial T}{\partial n}(t, x; \omega) = q_b, \quad x \in \partial D_2, \quad (4.27)$$

where D is a bounded domain in \mathbb{R}^d ($d = 1, 2, 3$) and Ω is a probability space. The temperature $T \equiv T(t, x; \omega)$ and heat source $f(t, x; \omega)$ are \mathbb{R} -valued functions on $[0, \infty] \times D \times \Omega$. The initial condition T_0 and the volumetric heat capacity of the medium c are \mathbb{R} -valued functions on $D \times \Omega$, and $\mathbf{k}(\mathbf{x}; \omega) = [k_{ij}(x, \omega)]$ is the conductivity tensor defined on $D^{d \times d} \times \Omega$. ∂D_1 and ∂D_2 denote the subsets of the boundary with fixed temperature and heat flux, respectively. We further assume that the medium is isotropic with $k_{ii}(x) = k(x)$, $\forall i \in [1, d]$ and $k_{ij} = 0$, $i \neq j$. The governing equation (4.25) can be rewritten as

$$c(x; \omega) \frac{\partial T}{\partial t} = \nabla \cdot [k(x; \omega) \nabla T] + f(t, x; \omega) \quad (x, \omega) \in D \times \Omega \quad (4.28)$$

with initial condition (4.26) and boundary condition (4.27). Note this assumption on \mathbf{k} simplifies the demonstration of the algorithm, but does not limit its applicability.

By using the generalized chaos expansion, we expand the random processes in the system of (4.28), (4.26) and (4.27) in the following form

$$k(x; \omega) = \sum_{i=0}^M k_i(x) \Phi_i(\boldsymbol{\xi}), \quad T(t, x; \omega) = \sum_{i=0}^M T_i(t, x) \Phi_i(\boldsymbol{\xi}), \quad f(t, x; \omega) = \sum_{i=0}^M f_i(t, x) \Phi_i(\boldsymbol{\xi}). \quad (4.29)$$

Note here we have replaced the infinite summation of $\boldsymbol{\xi}$ in infinite dimensions in equation (2.23) by a truncated finite-term summation of $\{\Phi\}$ in the finite dimensions of $\boldsymbol{\xi} = (\xi_1, \dots, \xi_n)$. The dimensionality n of $\boldsymbol{\xi}$ is determined by the random inputs. The random parameter ω is absorbed into the polynomial basis $\Phi(\boldsymbol{\xi})$, thus the expansion coefficients k_i , T_i and f_i are deterministic. Similar expansions are applied to other quantities c , T_0 , T_b and q_b . By substituting the expansion into governing equation (4.28), we obtain

$$\sum_{i=0}^M c_i(x) \Phi_i \sum_{j=0}^M \frac{\partial T_j}{\partial t} \Phi_j = \nabla \cdot \left[\sum_{i=0}^M k_i(x) \Phi_i \nabla \left(\sum_{j=0}^M T_j(t, x) \Phi_j \right) \right] + \sum_{i=0}^M f_i(t, x) \Phi_i. \quad (4.30)$$

A Galerkin projection of the above equation onto each polynomial basis $\{\Phi_i\}$ is then conducted in order to ensure that the error is orthogonal to the functional space spanned by the finite-dimensional basis $\{\Phi_i\}$. By projecting with Φ_k for each $k = \{0, \dots, M\}$ and employing the orthogonality relation (2.24), we obtain for each $k = 0, \dots, M$,

$$\sum_{i=0}^M \sum_{j=0}^M c_i(x) \frac{\partial T_j}{\partial t} e_{ijk} = \sum_{i=0}^M \sum_{j=0}^M \nabla \cdot [k_i(x) \nabla T_j(t, x)] e_{ijk} + f_k(t, x) \langle \Phi_k^2 \rangle, \quad (4.31)$$

where $e_{ijk} = \langle \Phi_i \Phi_j \Phi_k \rangle$. By defining

$$b_{jk}(x) = \sum_{i=0}^M c_i(x) e_{ijk}, \quad s_{jk}(x) = \sum_{i=0}^M k_i(x) e_{ijk}$$

we can rewrite the above equation as

$$\sum_{j=0}^M b_{jk}(x) \frac{\partial T_j}{\partial t}(t, x) = \sum_{j=0}^M \nabla \cdot [s_{jk}(x) \nabla T_j(t, x)] + f_k(t, x) \langle \Phi_k^2 \rangle, \quad \forall k \in [0, M]. \quad (4.32)$$

Equation (4.32) is a set of $(M + 1)$ coupled partial differential equations. The total number of equations $(M + 1) = (n + p)! / (n! p!)$ where n is the dimensionality of the chaos expansion and p the highest order of polynomials $\{\Phi\}$ (see equation (2.37)). The initial condition (4.26) and boundary condition (4.27) are expanded in the same form as (4.29). By matching the coefficients in the expansions, we obtain the initial conditions and boundary conditions for each expanded equation in (4.32) to complete the system.

By defining $\mathbf{B}(x) = [b_{ij}(x)]$, $\mathbf{S}(x) = [s_{ij}(x)]$ with the indices running through $[0, \dots, M]$ and solution vector $\mathbf{T}(t, x) = [T_0(t, x), T_1(t, x), \dots, T_M(t, x)]^t$, equation (4.32) can be written more concisely as

$$\mathbf{B}(x) \frac{\partial \mathbf{T}}{\partial t}(t, x) = \nabla \cdot [\mathbf{S}(x) \nabla \mathbf{T}(t, x)] + \mathbf{F}(t, x), \quad (4.33)$$

where $\mathbf{F}(x) = [f_0 \langle \Phi_0^2 \rangle, \dots, f_M \langle \Phi_M^2 \rangle]^t$. Here we have used the symmetry of matrices $\mathbf{B}(x)$ and $\mathbf{S}(x)$, i.e. $\mathbf{B}(x) = \mathbf{B}^t(x)$ and $\mathbf{S}(x) = \mathbf{S}^t(x)$. It can be seen that each expansion mode of the solution $T_i(t, x), i \in [0, \dots, M]$ in (4.33) is coupled on the left-hand-side and the right-hand-side. In order to solve the equation efficiently, we invert the matrix $\mathbf{B}(x)$ such that $\mathbf{D}(x) \equiv [d_{ij}(x)] = \mathbf{B}^{-1}(x)$ and rewrite (4.33) as

$$\frac{\partial \mathbf{T}}{\partial t}(t, x) = \mathbf{D}(x) \nabla \cdot [\mathbf{S}(x) \nabla \mathbf{T}(t, x)] + \mathbf{D}(x) \mathbf{F}(t, x) \quad (4.34)$$

or, in index form, $\forall k \in [0, \dots, M]$

$$\frac{\partial T_k}{\partial t}(t, x) = \sum_{i=0}^M \sum_{j=0}^M d_{kj}(x) \nabla \cdot [S_{ji}(x) \nabla T_i(t, x)] + \sum_{i=0}^M d_{ki}(x) f_i(t, x) \langle \Phi_i^2 \rangle \quad (4.35)$$

The left-hand-side is then decoupled and the equations can be integrated successively in time. To avoid the severe restriction on the size of time step, a mixed explicit-implicit method is employed where we keep the diagonal terms on the right-hand-side implicit and

the others explicit. In addition, we employ a high-order stiffly-stable integration scheme. To illustrate the algorithm, we denote the first term on the right-hand-side of equation (4.35) as

$$\begin{aligned} \sum_{i=0}^M \sum_{j=0}^M d_{kj}(x) \nabla \cdot [S_{ji}(x) \nabla T_i(t, x)] &= \sum_{j=0}^M d_{kj}(x) \nabla \cdot [S_{jk}(x) \nabla T_k(t, x)] + \\ &\quad \sum_{j=0}^M \sum_{i \neq k}^M d_{kj}(x) \nabla \cdot [S_{ji}(x) \nabla T_i(t, x)] \\ &\equiv R_{1_k}(t, x) + R_{2_k}(t, x). \end{aligned} \quad (4.36)$$

The scheme, in matrix form, can be written as

$$\frac{\gamma_0 \mathbf{T}^{n+1}(x) - \sum_{q=0}^{J-1} \alpha_q \mathbf{T}^{n-q}(x)}{\Delta t} = \mathbf{R}_1^{n+1}(x) + \sum_{q=0}^{J-1} \beta_q \mathbf{R}_2^{n-q}(x) + \mathbf{D}(x) \mathbf{F}^{n+1}(x) \quad (4.37)$$

where J is the order of accuracy in time and the superscripts $(n+1)$ and $(n-q)$ denote the time level t^{n+1} and t^{n-q} , respectively. The coefficients in the scheme are listed in table 4.1 for different temporal orders. Due to the diagonal dominance of matrix $\mathbf{S}(x)$, the restriction on time step is significantly relieved. The equations in (4.37) are *deterministic*

Coefficient	1st order	2nd order	3rd order
γ_0	1	3/2	11/6
α_0	1	2	3
α_1	0	-1/2	-3/2
α_2	0	0	1/3
β_0	1	2	3
β_1	0	-1	-3
β_2	0	0	1

Table 4.1: Coefficients in the mixed explicit-implicit integration (4.37) (see [63], chapter 8).

and can be discretized by any conventional method, e.g. finite elements, finite difference, etc. In this paper we employ the spectral/ hp element method to obtain high accuracy in physical space [63]. Specifically, the *Jacobi polynomials*, similar to the ones used in the aforementioned chaos expansion corresponding to beta distribution, are used for spatial

discretization. This produces a unified discretization in both the physical space and the random space.

4.3.2 Random Heat Conduction in an Electronic Chip

In this section we consider the heat conduction in an electronic chip subject to uncertainties in heat conductivity and capacity (see equation (4.28)). The computational domain D is shown in figure 4.3 along with the spatial discretization. The boundary of the domain consists of four segments: the top Γ_T , the bottom Γ_B , the two sides Γ_S and the boundaries of the cavity Γ_C , which has a depth of 0.6. Adiabatic boundary conditions are prescribed on Γ_B and Γ_S . The cavity boundary Γ_C is exposed to heat flux $q_b|_{\Gamma_C} = 1$. Two types of conditions on the top Γ_T are considered: one is maintained at constant temperature $T = 0$ (case 1) and the other is adiabatic (case 2). Due to non-zero net heat flux into the domain, there is no steady state in case 2. The initial condition is zero everywhere. For the spectral/ hp element solver in space, 16 elements are used in the domain, as shown in figure 4.3. Within each element, 6th-order (Jacobi) polynomials are employed. Numerical tests indicate that this is sufficient to resolve the problem in physical space. Six reference points are placed at the vertices of some chosen elements in the domain, as shown in figure 4.3. We are interested in the stochastic solution at these points and their cross-correlation coefficients. For example, the cross-correlation coefficient between reference point A and B is

$$\rho_{AB}(t) = \frac{\mathbb{E} [(T(t, x_A; \omega) - \mathbb{E}[T(t, x_A; \omega)])(T(t, x_B; \omega) - \mathbb{E}[T(t, x_B; \omega)])]}{\sigma_T(t, x_A)\sigma_T(t, x_B)}, \quad (4.38)$$

where $\sigma_T(t, x)$ is the standard deviation of the solution $T(t, x; \omega)$.

The uncertain heat conductivity and capacity of the medium are random fields, with mean fields $\bar{k}(x, y; \omega) = 1$, $\bar{c}(x, y; \omega) = 1$ and auto-correlation functions of the form

$$C(r) = \frac{r}{b} K_1 \left(\frac{r}{b} \right), \quad (4.39)$$

where K_1 is the modified Bessel function of the second kind with order 1, b scales as correlation length and r is the distance between two points. The Karhunen-Loeve (KL)

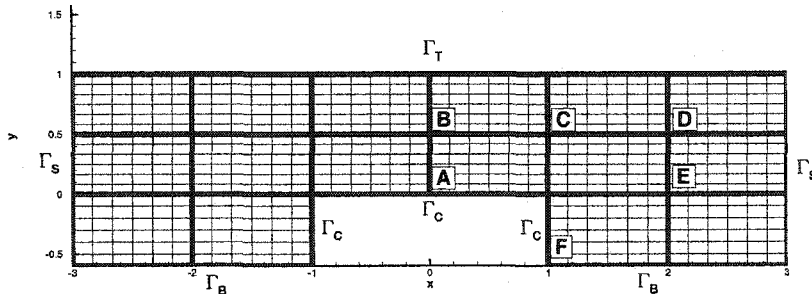


Figure 4.3: Schematic of the domain of the chip geometry. It consists of 16 spectral elements of order 6th (7 points).

decomposition (2.11) is employed, following a similar procedure as in section 3.2.2. For demonstration purposes, relatively strong auto-correlations are assumed for k and c with parameter $b = 20$, which results in fast decay of the eigenvalues from the KL decomposition. Subsequently, we employ the first three eigenmodes for k and the first eigenmode for c , and assume the random variables in (2.11) are *uniform* random variables. In figure 4.4, we plot the first two eigenmodes of the KL decomposition resulted from the numerical eigensolution of the Bessel type correlation function (4.39). We further assume zero cross-correlation between k and c , with uncertain intensity of $\sigma_k = \sigma_c = 0.2$. This results in a *four-dimensional* ($n = 4$) Wiener-Legendre chaos expansion, with three dimensions from k and one from c . Third-order ($p = 3$) Legendre chaos expansion is used. Resolution checks indicate that this is sufficient to resolve the problem in random space. For $n = 4$ and $p = 3$, the total number of chaos expansion terms is 35 (see equation (2.37)).

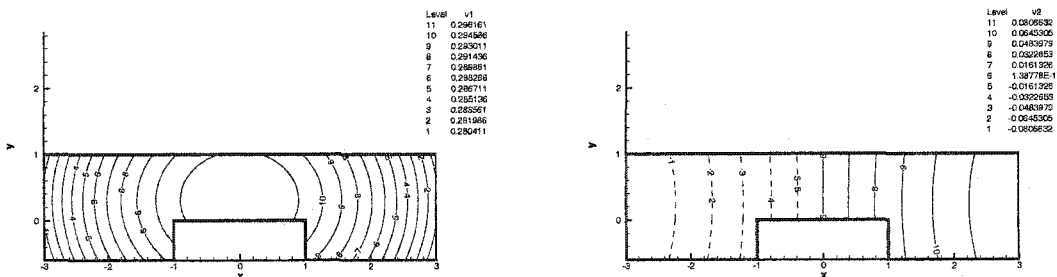


Figure 4.4: Eigenmodes of the correlation field. Left: the first eigenmode; Right: the second eigenmode.

We first consider case 1, where the temperature at the top boundary is maintained at $T_b|_{\Gamma_T} = 0$. In this case, the temperature reaches *steady state*. In figure 4.5 the contours of the stochastic solution of the temperature field, including the mean and standard deviation, are plotted. It is seen that the largest output uncertainty, indicated by the standard deviation, occurs near the corners between the cavity and the bottom boundary. In figure 4.6 we show the evolution of stochastic solution at the reference points, with mean on the left and COV (coefficient of variance) defined as $\text{COV}(x, t) = \sigma_T(x, t)/\mathbb{E}[T(x, t; \omega)]$ on the right. We observe that the solution reaches steady state quickly and there is a non-negligible response in COV at the early transient stage. The time evolution of cross-correlation coefficients between reference point A and the other points is shown in figure 4.7. It is seen that all the points except point B are negatively correlated with point A, and the cross correlation between A and B is weak. Note that from the definitions, the COV and cross-correlation coefficients are not defined at $t = 0$, as our initial condition is zero everywhere. Thus in the following, the value of these coefficients is not plotted near $t = 0$.

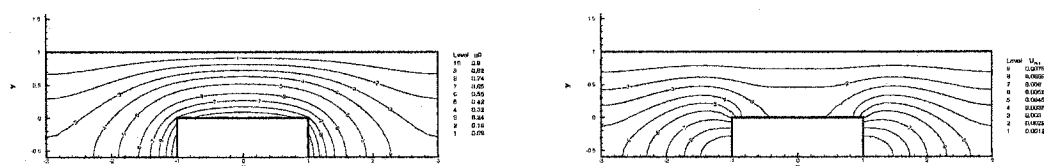


Figure 4.5: Contours of temperature distribution in the electronic chip at steady state (case 1). Left: mean field; Right: standard deviation.

For the second case, we consider the *top boundary as adiabatic*. Due to the net inward heat flux from the cavity boundary, the temperature field will keep increasing and thus there is no steady state. The equation is integrated to $t = 1$ and the contours of mean field and standard deviation field are shown in figure 4.8. It is seen that the variation of the standard deviation across the width of the domain is small and the maximum value is along the vertical center line. This is qualitatively different from the steady state solution of case 1. The solutions at reference points A through F are plotted in figure 4.9. It can be seen that while the mean temperature keeps growing over time, the COVs of temperature approach steady state. Relatively strong variation in COV is again visible at the early

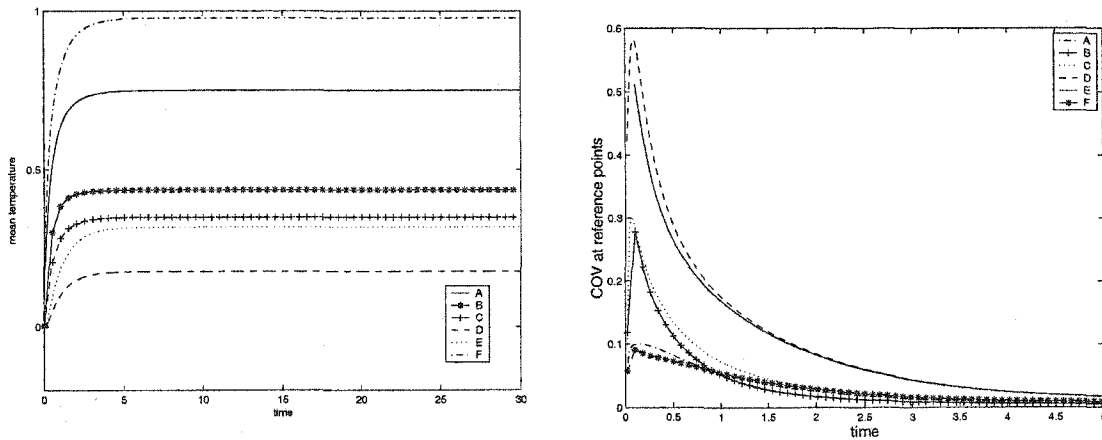


Figure 4.6: Temperature evolution at reference points (case 1). Left: mean temperature; Right: COV (coefficient of variance).

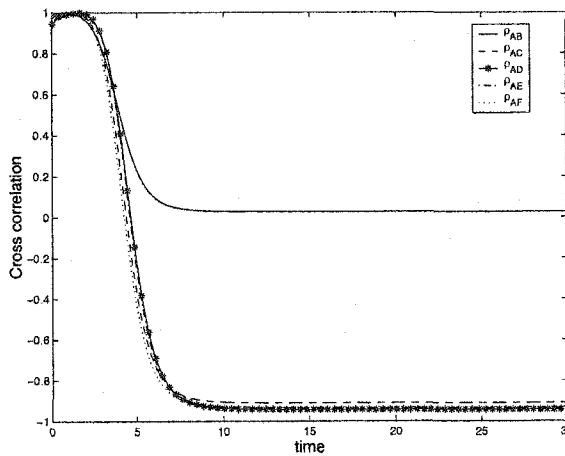


Figure 4.7: Time evolution of cross-correlation coefficients between reference point A and other points (case 1).

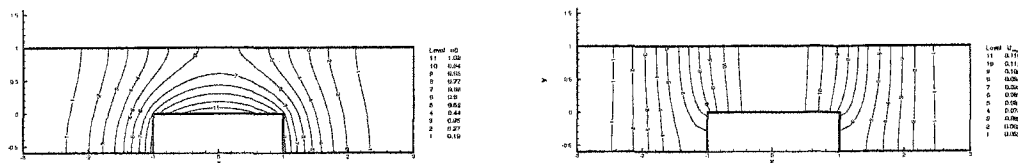


Figure 4.8: Contours of temperature distribution in the electronic chip (unsteady state at $t = 1$, case 2). Left: mean field; Right: standard deviation.

transient stage. Note that the reference point F, which has the highest mean temperature, is the least sensitive to the input uncertainty. Its COV reaches steady state very fast with value less than 10%. In figure 4.10, the cross-correlation coefficients of reference points B,C,D,E and F with respect to point A, are plotted. Again the statistics approach steady state over time. In contrast to the result from case 1 in figure 4.7, all points are positively correlated to point A with strong correlation. In figure 4.11, the evolution of temperature at reference points are plotted in error bars, with the lines centered at the mean values and the length of the bars equal to two standard deviations (one up and one down).

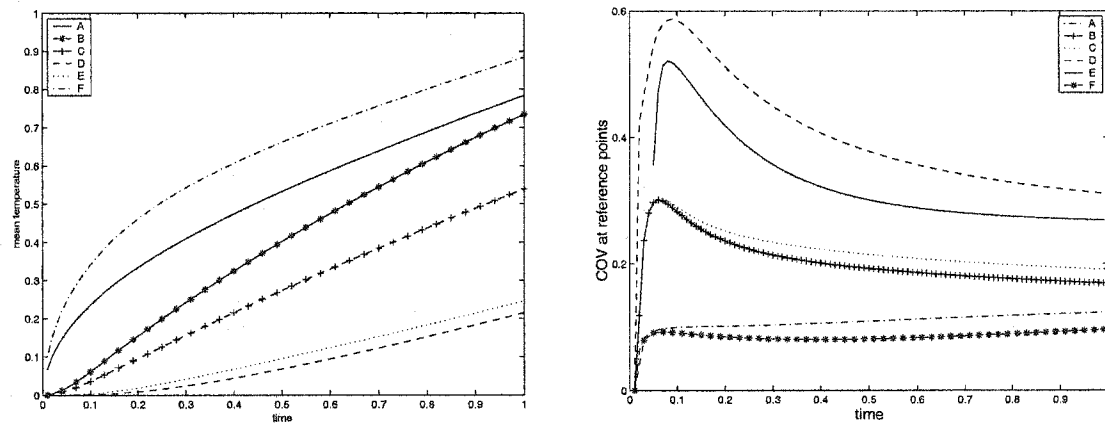


Figure 4.9: Temperature evolution at reference points (case 2: unsteady problem). Left: mean temperature; Right: COV (coefficient of variance).

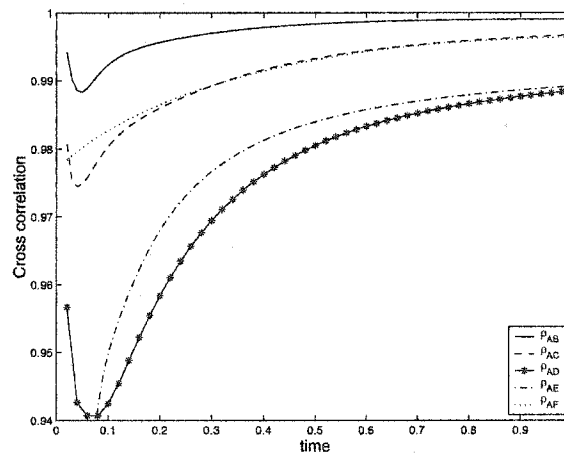


Figure 4.10: Time evolution of cross-correlation coefficients between reference point A and other points (case 2: unsteady problem).

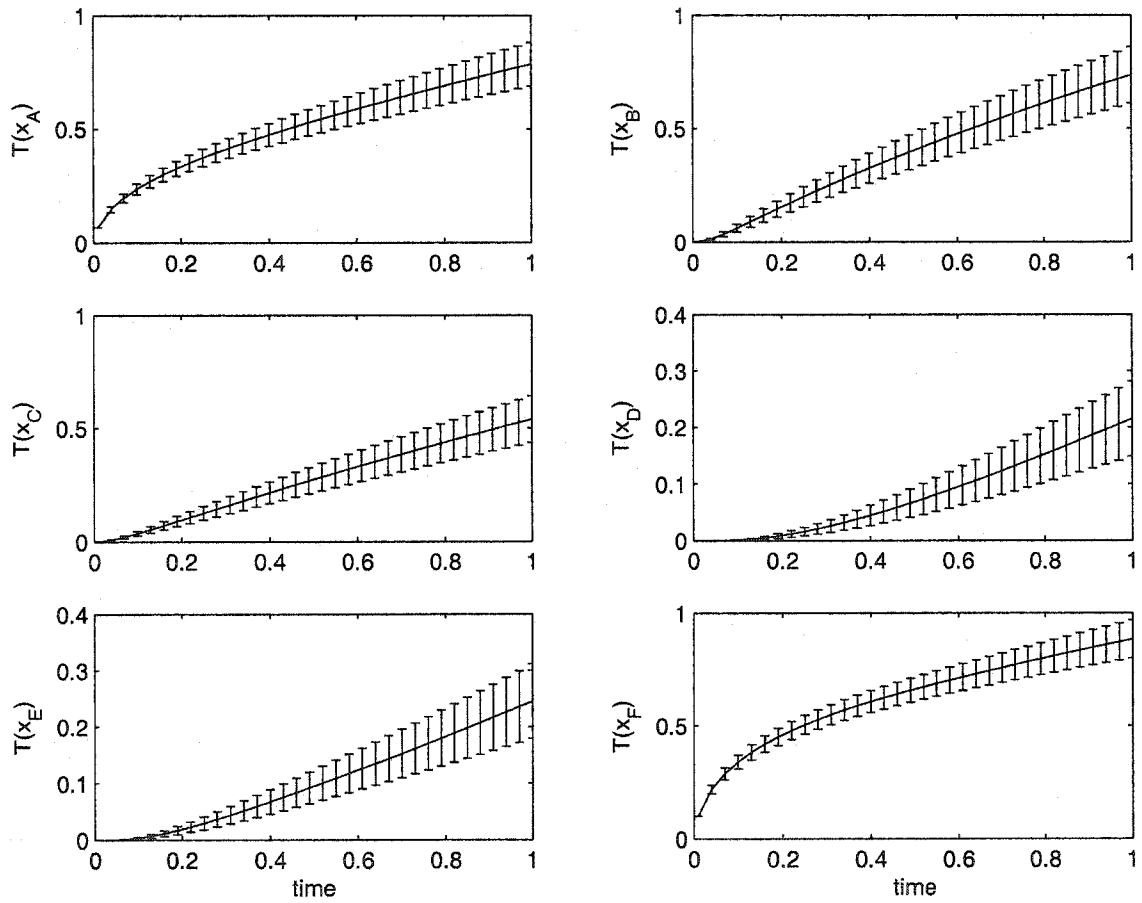


Figure 4.11: Stochastic solution at reference points (case 2: unsteady problem).

Monte Carlo simulations were also conducted, for both cases, to validate the results by polynomial chaos expansion. For case 1 (steady problem) we conducted 20,000 realizations. For case 2 (unsteady problem) we employed 150,000 realizations due to the shorter integration interval in time ($t = 1$). In figure 4.12 we show the evolution of solution statistics at some reference points. On the left, the cross-correlation coefficients at reference points A and B for case 1 are plotted. The integration was conducted up to $t = 20$ when the solutions reach steady state, and we show the close-up view up to $t = 6$ to focus on the early transient state. It can be seen that the results between Monte Carlo Simulation and polynomial chaos agree well; both reveal the negative cross-correlation between points A and C. The agreement between other reference points is equally good and thus it is not shown here. On the right of figure 4.12, we show, for case 2, the evolution of COVs at reference points A and D (note in this case, point D has the maximum response in COV). Again the results of MCS (150,000 realizations) agree well with those of chaos expansion. Oscillations in MCS result can be seen during the early sharp transition of point D. Good agreement is obtained for the other statistics, e.g. the mean, standard deviation and cross-correlation, and thus they are not shown here.

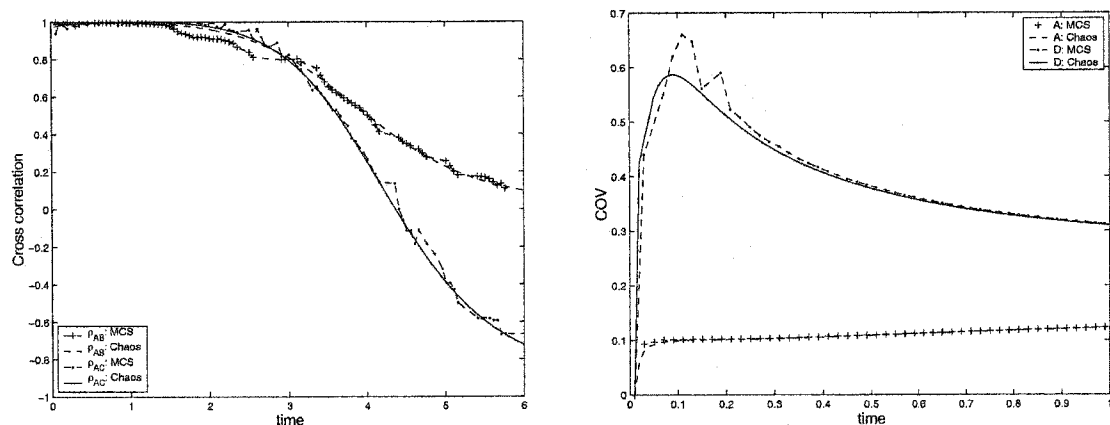


Figure 4.12: Comparison of results obtained by Monte Carlo simulation and generalized polynomial chaos expansion. Left: evolution of cross-correlation coefficients at reference points for case 1 (20,00 realizations for MCS); Right: evolution of COVs at reference points for case 2 (150,000 realizations for MCS).

Another issue we are interested in is the individual effect of the uncertainty in k and c on the output for the unsteady case (case 2). Two simulations are performed with

one having random conductivity k only and the other random heat capacity c only. All other parameters are the same as those in case 2. In figure 4.13 we plot the evolution of temperature COV at the reference points, with random capacity c only (left) and random conductivity k only (right). It can be seen that the COVs of the random capacity only case are smaller than those of random conductivity only, indicating the uncertainty in heat conductivity has more influence on the output than that in heat capacity, for this particular problem. Comparison on the cross-correlation coefficients are shown in figure 4.14, where we observe a stronger correlation for the random capacity only case. Note that for this unsteady problem where the temperature grows exponentially fast, the influence of heat capacity can be much more substantial if its probability distribution has unbounded support, e.g. Gaussian distribution. This was illustrated for a one-dimensional heat conduction problem in [40], and we have verified the results independently.

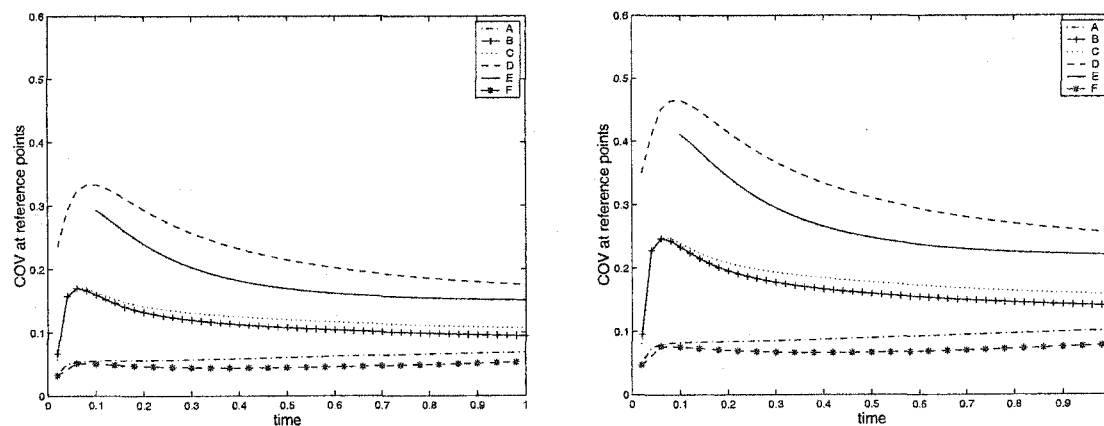


Figure 4.13: Temperature COV evolution at reference points. Left: random capacity only; Right: random conductivity only.

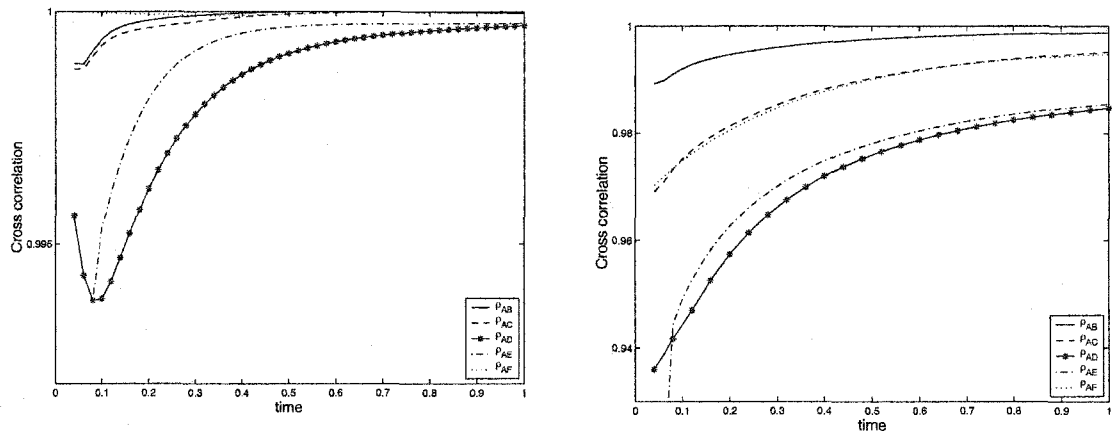


Figure 4.14: Evolution of cross-correlation coefficient between reference point A and the other points. Left: random capacity only; Right: random conductivity only.

Chapter 5

Advection-Diffusion Equation

5.1 Linear Advection-Diffusion

In this section, we consider the two-dimensional advection-diffusion equation with random transport velocity. This can be considered as a model of transport phenomena in random media, which has been a subject of intensive research; see, for example, [99, 100, 110, 127, 128]. A study of one-dimensional advection equation using Hermite-chaos can be found in [57]. In this section, we use this equation as a means of examining the approximation properties of generalized polynomial chaos. Different types of random distributions are considered, and convergence rate is examined using exact solutions.

Consider the two-dimensional advection-diffusion equation with random transport velocity

$$\frac{\partial \phi}{\partial t}(\mathbf{x}, t; \omega) + \mathbf{u}(\mathbf{x}; \omega) \cdot \nabla \phi = \nu \nabla^2 \phi \quad (\mathbf{x}, t; \omega) \in D \times \mathbb{R}^+ \times \Omega, \quad (5.1)$$

where D is a bounded domain in \mathbb{R}^2 , and Ω is a probability space. In this paper, we will assume deterministic boundary and initial conditions. The transport velocity field is $\mathbf{u}(\mathbf{x}; \omega) = u(x, y; \omega)\mathbf{e}_x + v(x, y; \omega)\mathbf{e}_y$, and we will focus on large-scale random perturbations, i.e. the random field is strongly correlated and retains certain smoothness. Stochastic advection-diffusion subject to white noise input will not be considered here.

The solution process and the transport velocity field are expanded in term of generalize

polynomial chaos

$$\phi(\mathbf{x}, t; \omega) = \sum_{i=0}^M \phi_i(\mathbf{x}, t) \Phi_i(\boldsymbol{\xi}(\omega)), \quad \mathbf{u}(\mathbf{x}; \omega) = \sum_{i=0}^M \mathbf{u}_i(\mathbf{x}) \Phi_i(\boldsymbol{\xi}(\omega)). \quad (5.2)$$

By substituting the expansions into governing equation (5.1) and conducting the Galerkin projection onto each basis Φ_k for $k = \{0, \dots, M\}$, we obtain for $k = \{0, \dots, M\}$,

$$\frac{\partial \phi_k}{\partial t} + \frac{1}{\langle \Phi_k^2 \rangle} \sum_{i=0}^M \sum_{j=0}^M \mathbf{u}_i \cdot \nabla \phi_j e_{ijk} = \nu \nabla^2 \phi_k, \quad (5.3)$$

where $e_{ijk} = \langle \Phi_i \Phi_j \Phi_k \rangle$.

Equation (5.3) is a set of $(M + 1)$ partial differential equations coupled through the advection terms. These equations are *deterministic* and can be solved readily by any conventional numerical schemes. In this paper, we employ the spectral/*hp* element method in physical space and a second-order stiffly stable method in time.

5.1.1 Model problem: convergence

We first consider a simple model problem where its exact solution is available. Assume the transport velocity is a circular motion plus a constant random perturbation, i.e.

$$\mathbf{u}(\mathbf{x}; \omega) = (y + a(\omega), -x - b(\omega)), \quad (5.4)$$

where $a(\omega)$ and $b(\omega)$ are random variables. The initial condition is a Gaussian-shape cone

$$\phi(\mathbf{x}, 0; \omega) = e^{-[(x-x_0)^2 + (y-y_0)^2]/2\lambda^2}. \quad (5.5)$$

The exact stochastic solution can be obtained as

$$\phi_e(\mathbf{x}, t; \omega) = \frac{\lambda^2}{\lambda^2 + 2\nu t} e^{-(\hat{x}^2 + \hat{y}^2)/2(\lambda^2 + 2\nu t)}, \quad (5.6)$$

where

$$\begin{cases} \hat{x} = x + b(\omega) - (x_0 + b(\omega)) \cos t - (y_0 + a(\omega)) \sin t, \\ \hat{y} = y + a(\omega) + (x_0 + b(\omega)) \sin t - (y_0 + a(\omega)) \cos t. \end{cases}$$

By using the exact solution, we examine the ‘mean-square’ error of numerical solutions,

$$e_2(\mathbf{x}, t) = \left(E [\phi_p(\mathbf{x}, t; \omega) - \phi_e(\mathbf{x}, t; \omega)]^2 \right)^{1/2}, \quad (5.7)$$

where $E(\cdot)$ denotes the ‘expectation’ operator and ϕ_M is the numerical solution obtained by p^{th} -order expansion. We then examine the L_∞ -norm of $e_2(\mathbf{x}, t)$ at some fixed time t in the physical space. Here we set $\nu = 10^{-5}$, $\lambda = 1/8$ and $a(\omega) = b(\omega) = 0.05\xi$, where ξ is a continuous random variable with zero mean. The final integration time is set as $t = 3\pi$.

Beta random input and Jacobi-chaos

Here we assume $\xi \sim Be^{(\alpha, \beta)}(-1, 1)$ is a beta random variable defined in $(-1, 1)$ with PDF (A.17) and parameters $\alpha, \beta > -1$. Correspondingly, the Jacobi-chaos is employed.

The result of uniform random input ($\alpha = \beta = 0$) by Legendre-chaos is shown in Figure 5.1. We observe that errors in both the mean and variance decrease exponentially fast as the order of chaos expansion (p) increases. This is in accordance with the results in [129, 130, 131].

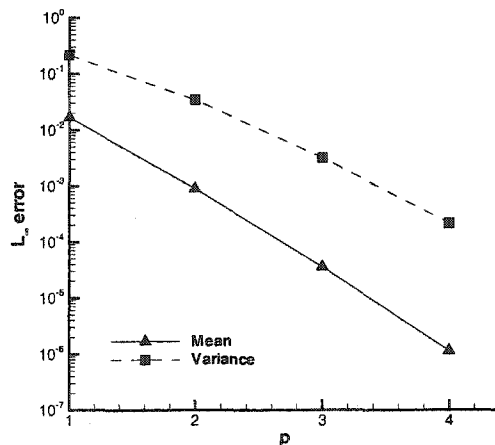


Figure 5.1: L^∞ error of Legendre-chaos with uniform random input at $T = 3\pi$.

In Figure 5.2, the error convergence of $Be^{(10,10)}(-1, 1)$ random input is shown, and similar exponential convergence is obtained.

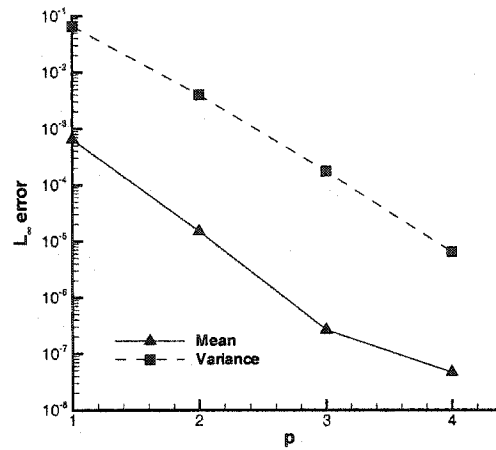


Figure 5.2: L^∞ error of Jacobi-chaos with $Be^{(10,10)}(-1, 1)$ random input at $T = 3\pi$.

Gaussian random input and Hermite-chaos

Figure 5.3 shows the convergence rate of Hermite-chaos expansion when the input follows a Gaussian distribution, i.e. $\xi \sim N(0, 1)$.

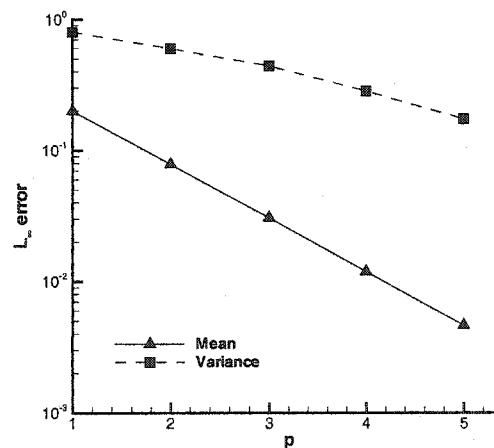


Figure 5.3: L^∞ error of Hermite-chaos with Gaussian random input at $T = 3\pi$.

In Figure 5.4, the probability density function (PDF) of the solution at its peak location

is shown at $t = \pi$, along with the corresponding PDF from the exact solution (5.6). The peak of the solution is in the range of $[0, \phi_{\max}]$ where $\phi_{\max} \leq \frac{\lambda^2}{\lambda^2 + 2\nu t} \leq 1$. Thus, its PDF should be strictly bounded on both sides, i.e. with no tails present. It is seen from Figure 5.4 that the Hermite-chaos approximates the exact PDF well, except the apparent Gibb's oscillations near the corner. However, the numerical PDF is clearly not bounded from below and has a thin tail along the negative axis. In fact, since Gaussian random variables have infinite support, i.e. $\xi \in (-\infty, \infty)$, we expect Hermite-chaos expansions, which are polynomial functions of Gaussian variables, have infinite long tail on at least one side, depending on the sign of the highest expansion order. In this particular problem, the long tail indicates the existence of unphysical solution with very small but *nonzero* probability.

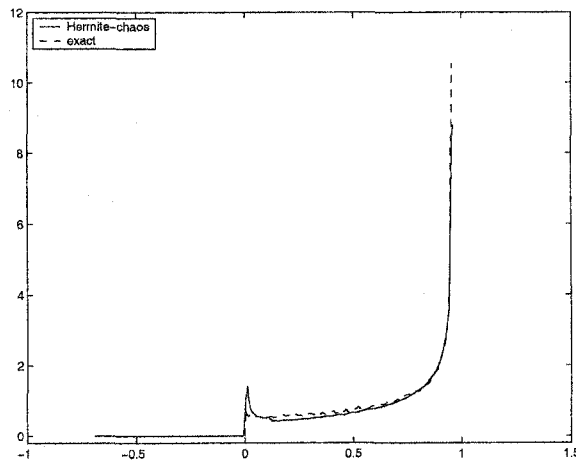


Figure 5.4: PDF of the peak solution at $T = \pi$ with Gaussian input and Hermite-chaos expansion.

'Truncated' Gaussian input and Jacobi-chaos

One alternative to the Gaussian distribution is a 'truncated' Gaussian distribution, first introduced in [133]. This is a Jacobi-chaos approximation to Gaussian distributions. It approximates Gaussian distributions closely with no long tails. It has been shown that the long tails of Gaussian distribution can result in ill-posedness of Hermite-chaos expansion for certain applications where the boundedness of stochastic inputs is critical. (see [5, 133] and section 4.2.1.) Thus, the 'truncated' Gaussian distribution can be used to represent

Gaussian-like inputs with no tails. Details on the construction of ‘truncated’ Gaussian $G^{(\alpha,\beta)}$ can be found in Appendix C. Here, we examine the performance of truncated Gaussian, although for random transport velocity the tails of the Gaussian assumption will not pose ill-posedness of the problem. In particular, we employ the fifth-order Jacobi-chaos approximation with $\alpha = \beta = 10$, i.e., $G^{(10,10)}$. The corresponding Jacobi-chaos with $\alpha = \beta = 10$ is used to solve the problem. The error convergence is shown in Figure 5.5, where we use the exact solution from Gaussian input. We can see that the error converges fast, and it is almost exponential with respect to polynomial order. This indicates that the error from the difference between $G^{(10,10)}$ and $N(0,1)$ is subdominant compared to the overall error.

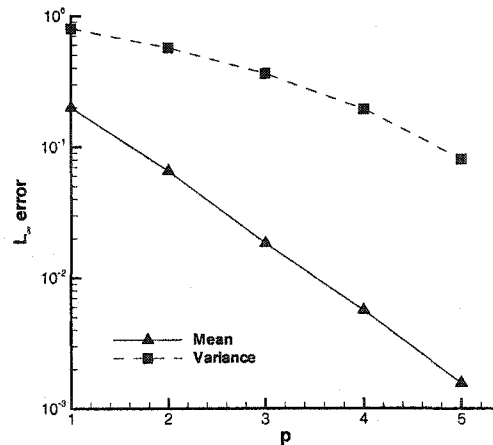


Figure 5.5: L^∞ error of Jacobi-chaos with truncated Gaussian $G^{(10,10)}$ random input at $T = 3\pi$.

In Figure 5.6 we show the PDF of the solution at its peak location at $t = \pi$. The solution of Jacobi-chaos approximates the exact PDF well, except the apparent Gibb’s oscillations near the corner. Note that here the PDF of the Jacobi-chaos solution is strictly bounded on both ends with no tails, consistent with the physics of the advection-diffusion.

The stochastic response at the solution peak is shown in Figure 5.7, along with the deterministic solution denoted by dotted line. The presence of the random perturbation in the transport velocity introduces extra ‘diffusion’ in the mean solution, compared to

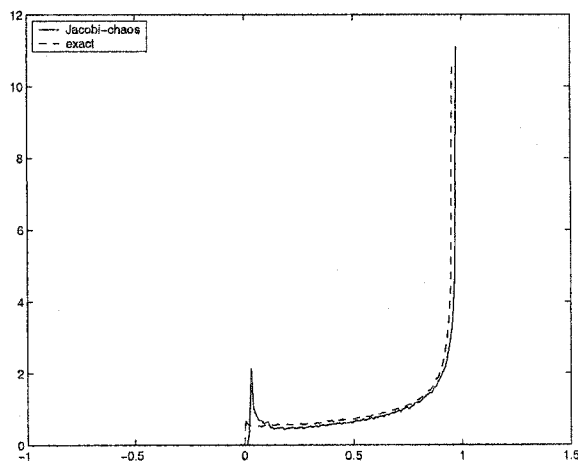


Figure 5.6: PDF of the peak solution at $T = \pi$ with $G^{(10,10)}$ input and Jacobi-chaos expansion.

the deterministic solution. It should be noted that for this particular type of random perturbation (5.4), the stochastic effect disappears at $t = 2n\pi, n = 0, 1, \dots$ (see exact solution (5.6)). This can be clearly seen from the error bars.

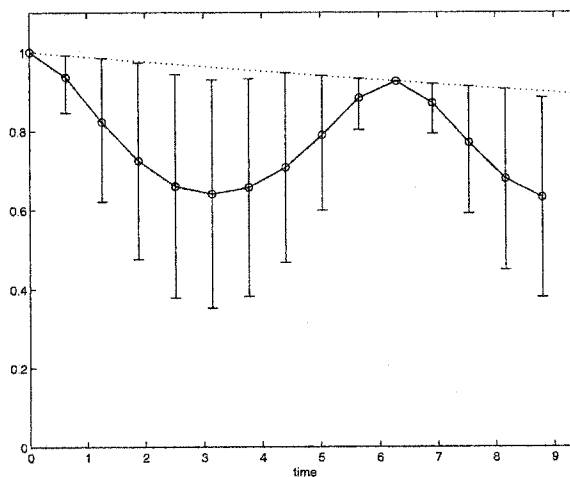


Figure 5.7: Error bars of the evolution of the peak solution with $G^{(10,10)}$ input and Jacobi-chaos expansion. The circles represent the stochastic mean solution and the dotted line the deterministic solution.

In Figures 5.8 to 5.13, the evolution of the mean solutions and variances under the truncated Gaussian input $G^{(10,10)}$ is shown at different times. The initial condition is a symmetric Gaussian-shape cone with circular contours. We observe that as the cone

travels, it becomes asymmetric with elliptic contours due to the random perturbation introduced in the transport velocity (5.4). After one evolution ($t = 2\pi$), it returns to the symmetric shape as the random effect disappears at this instance. This is confirmed in Figure 5.11; the solution variance here at $t = 2\pi$ is of the order $O(10^{-7})$. The deformation resumes after this. The corresponding deterministic solution is free from such deformation, and the cone will remain a symmetric cone shape and simply decay over time.

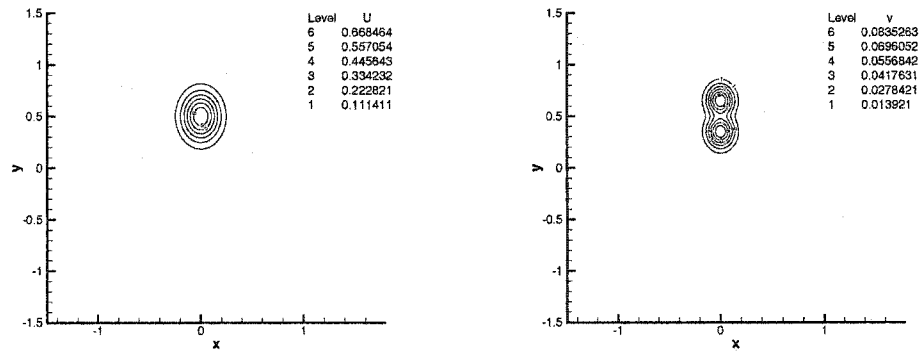


Figure 5.8: Jacobi-chaos solution with $G^{(10,10)}$ random input at $T = 0.5\pi$. Left: mean solution; Right: variance.

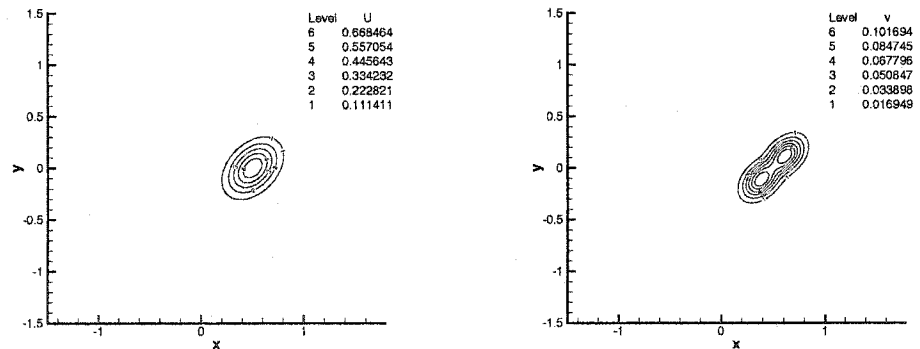


Figure 5.9: Jacobi-chaos solution $G^{(10,10)}$ random input at $T = \pi$. Left: mean solution; Right: variance.

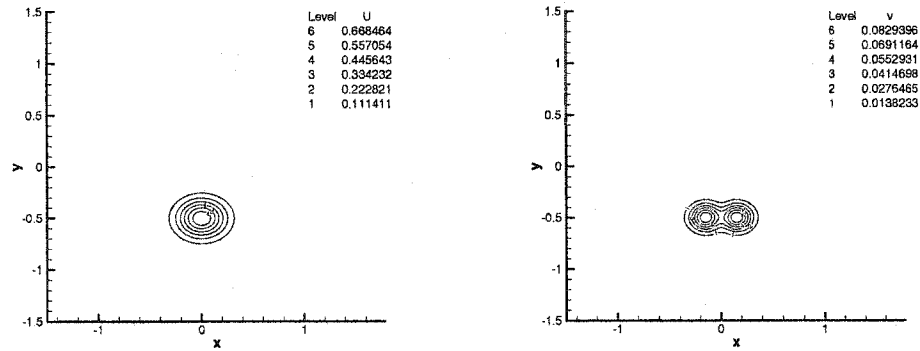


Figure 5.10: Jacobi-chaos solution $G^{(10,10)}$ random input at $T = 1.5\pi$. Left: mean solution; Right: variance.

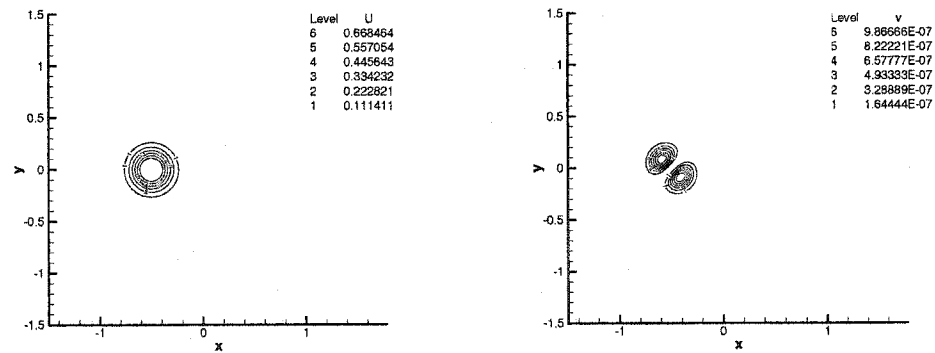


Figure 5.11: Jacobi-chaos solution $G^{(10,10)}$ random input at $T = 2\pi$. Left: mean solution; Right: variance.

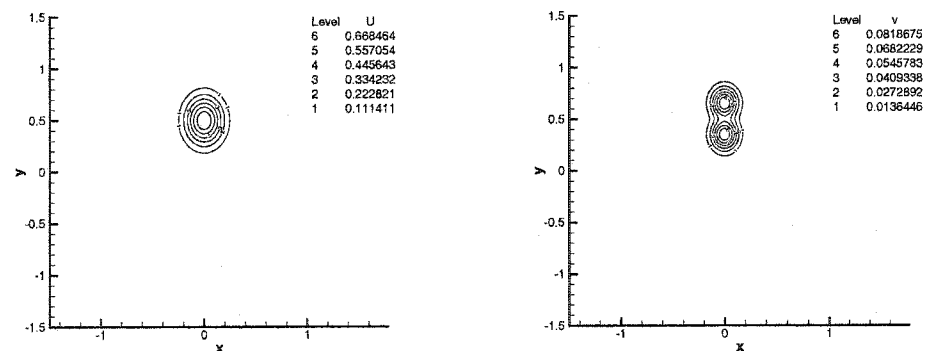


Figure 5.12: Jacobi-chaos solution $G^{(10,10)}$ random input at $T = 2.5\pi$. Left: mean solution; Right: variance.

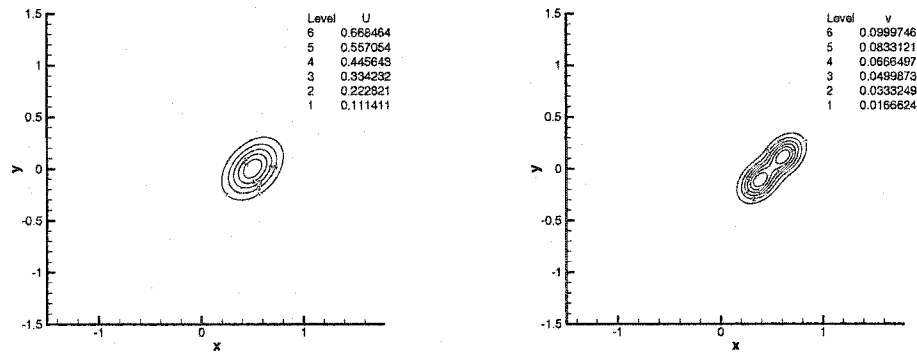


Figure 5.13: Jacobi-chaos solution $G^{(10,10)}$ random input at $T = 3\pi$. Left: mean solution; Right: variance.

5.1.2 Results with two-dimensional ‘truncated’ Gaussian input

In this section we assume the random transport velocity takes the following form

$$\mathbf{u} = (y + 0.05y\xi_1, -x - 0.05x\xi_2), \quad (5.8)$$

where ξ_1 and ξ_2 are two independent Gaussian random variables with zero mean and unit variance. To avoid the unphysical tails in the solution, we use the ‘truncated’ Gaussian $G^{(10,10)}$ to approximate ξ_1 and ξ_2 , and employ the Jacobi-chaos to solve the equations.

The evolution of the stochastic response at the peak is shown in Figure 5.14, along with the deterministic solution denoted by dotted line. The extra diffusion introduced by randomness in transport velocity can be seen clearly, compared to the deterministic solution. As opposed to the example in Section 5.1.1, the random effect does not disappear after every 2π evolution in time.

The evolution of the stochastic solutions at different times is plotted in Figures 5.15 to 5.20. On the left are the mean solutions, and on the right are the variances. Compared to the results of one-dimensional ‘truncated’ Gaussian perturbation in Section 5.1.1, the mean solution under the two-dimensional random perturbation deforms in a different way and does not return to the symmetric shape after each period 2π .

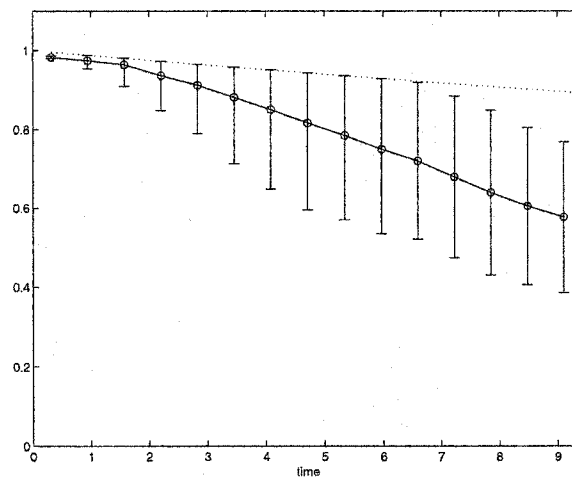


Figure 5.14: Error bars of the evolution of the peak solution with two-dimensional 'truncated' Gaussian input and Jacobi-chaos expansion. The circles represent the stochastic mean solution and the dotted line the deterministic solution.

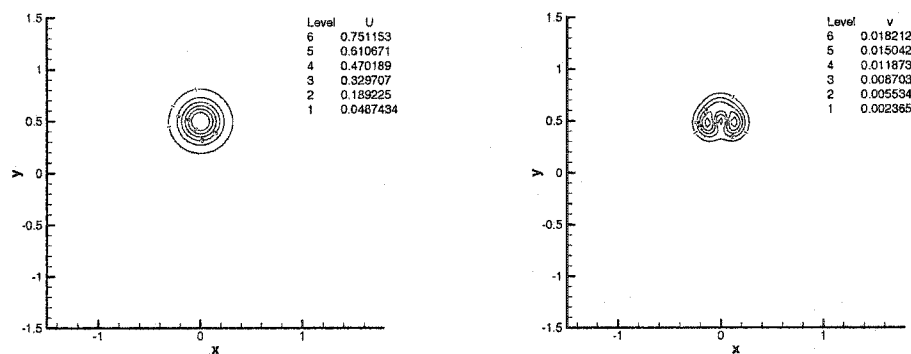


Figure 5.15: Jacobi-chaos solution with 2D-Gaussian random input at $T = 0.5\pi$. Left: mean solution; Right: variance.

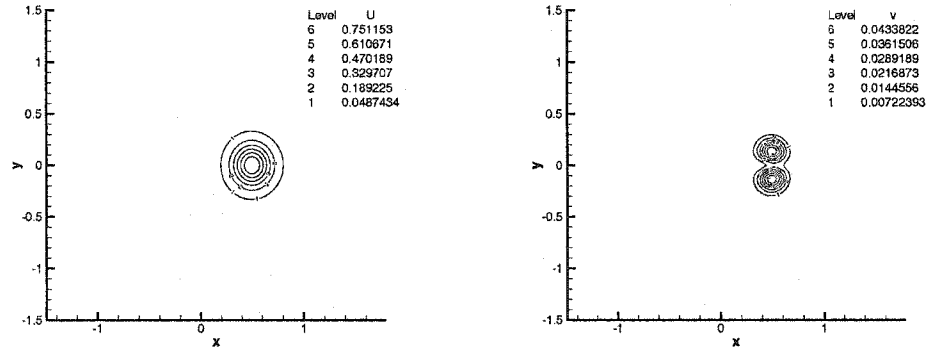


Figure 5.16: Jacobi-chaos solution of 2D-Gaussian random input at $T = \pi$. Left: mean solution; Right: variance.

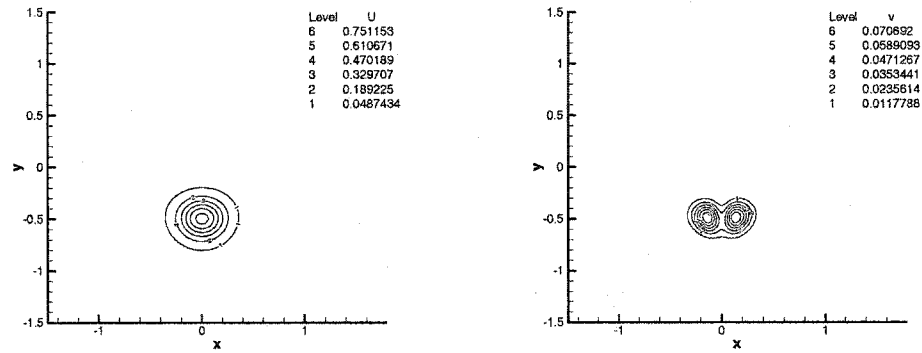


Figure 5.17: Jacobi-chaos solution of 2D-Gaussian random input at $T = 1.5\pi$. Left: mean solution; Right: variance.

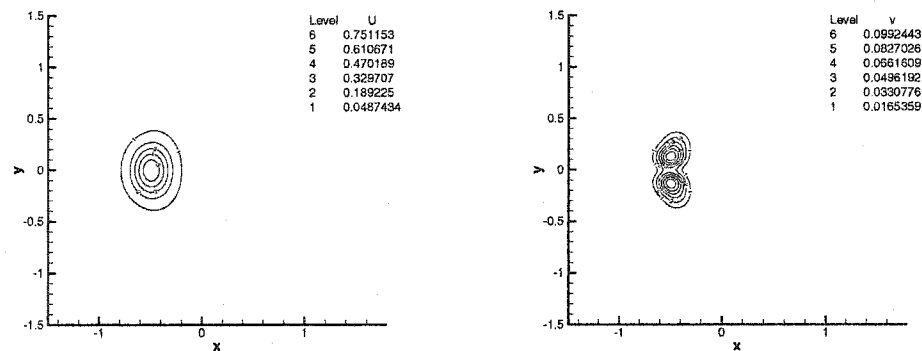


Figure 5.18: Jacobi-chaos solution of 2D-Gaussian random input at $T = 2\pi$. Left: mean solution; Right: variance.

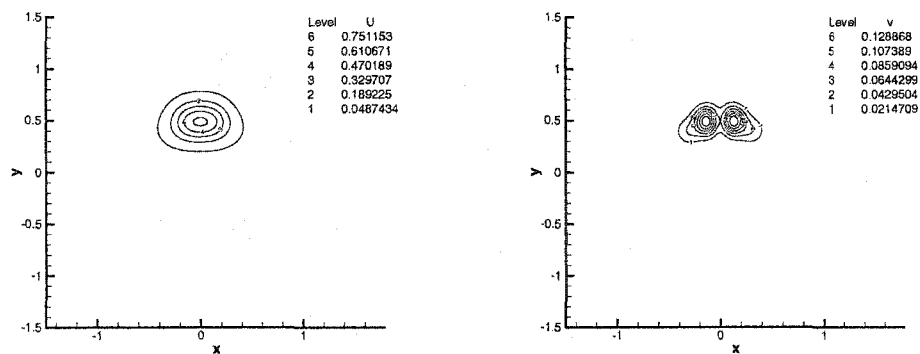


Figure 5.19: Jacobi-chaos solution of 2D-Gaussian random input at $T = 2.5\pi$. Left: mean solution; Right: variance.

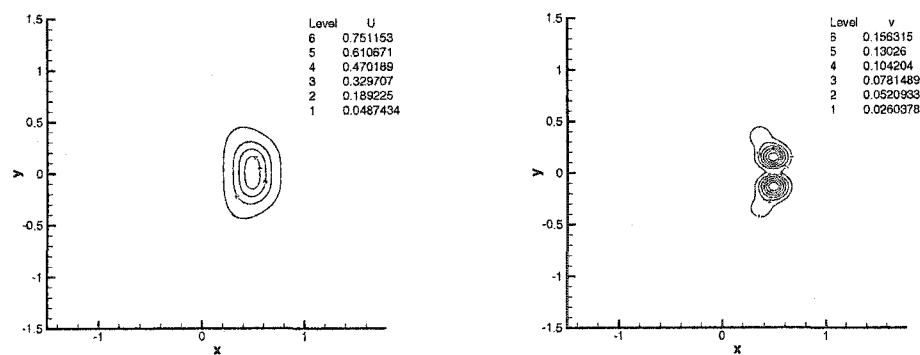


Figure 5.20: Jacobi-chaos solution of 2D-Gaussian random input at $T = 3\pi$. Left: mean solution; Right: variance.

5.2 Nonlinear Advection-Diffusion: Burgers' Equation

We consider the viscous Burgers' equation,

$$\begin{cases} u_t + uu_x = \nu u_{xx}, & x \in [-1, 1], \\ u(-1) = 1 + \delta, & u(1) = -1, \end{cases} \quad (5.9)$$

where $\delta > 0$ is a small perturbation to the left boundary condition ($x = -1$) and $\nu > 0$ is the viscosity. The presence of viscosity smoothes out the shock discontinuity which will develop otherwise. Thus, the solution has a transition layer, which is a region of rapid variation and extends over a distance $O(\nu)$ as $\nu \downarrow 0$. The location of the transition layer z , defined as the zero of the solution profile $u(z) = 0$, varies with time, and its eventual location at steady state is extremely sensitive to the boundary data. This phenomenon, termed *supersensitivity* in *deterministic* asymptotic analysis, was first observed by Lorentz [81]. In this section, we will present numerical solutions that exhibit supersensitivity under both deterministic and random perturbations on the boundary condition. In particular, we consider the following two cases:

1. $0 < \delta \ll O(1)$ is a deterministic value;
2. $\delta \in (0, \epsilon)$ is a random variable in $(0, \epsilon)$ with $\epsilon \ll O(1)$ and a given continuous probability distribution function (PDF) $f(\delta)$.

For problems with deterministic perturbations, extensive research efforts by asymptotic analysis have been devoted to the Burgers' equation and more general viscous conservation laws in one spatial dimension (see [66, 67, 68, 69, 70, 105, 106]). In [33], numerical simulations were conducted for both one-dimensional Burgers' equation and its two-dimensional generalization. The results agree well with the asymptotic estimates. In this section we first revisit the deterministic supersensitivity problem. Two numerical approaches are employed. First, we solve the exact formula at steady state. This formula defines the steady state solution implicitly in a nonlinear way. Although it has been known in the literature, its solution has rarely been sought. Here we solve it iteratively with high accuracy for some chosen parameters. Subsequently, we conduct direct numerical simulations by integrating the Burgers' equation (5.9) via the spectral/ hp element method [63]. It is shown

that the results from the direct simulations agree with the exact solution for up to seven significant digits.

5.2.1 Deterministic Supersensitivity

In this section we study the viscous Burgers' equation (5.9) with a small *deterministic* perturbation $\delta > 0$ on the upstream boundary condition.

Exact solution

The viscous Burgers' equation (5.9) has an exact solution at steady state

$$u(x) = -A \tanh \left[\frac{A}{2\nu} (x - z_{ex}) \right] \quad (5.10)$$

where z_{ex} is the location of transition layer where $u(z_{ex}) = 0$ and $-A = \left. \frac{\partial u}{\partial x} \right|_{x=z_{ex}}$ its slope at this location. These two unknowns are determined by the two boundary conditions

$$A \tanh \left[\frac{A}{2\nu} (1 + z_{ex}) \right] = 1 + \delta, \quad A \tanh \left[\frac{A}{2\nu} (1 - z_{ex}) \right] = 1. \quad (5.11)$$

We can eliminate z_{ex} and obtain a single equation for A

$$(1 + \delta + A^2) \tanh(A/\nu) = (2 + \delta)A. \quad (5.12)$$

Thus, we can solve (5.12) for A first and then solve z_{ex} from one of the equations in (5.11). Iterative methods are needed for these nonlinear equations. It should be noted that the convergence is very sensitive to the choices of initial guess due to the 'supersensitive' nature of the original problem.

Asymptotic analysis

There has been a great number of publications on the asymptotic analysis of the supersensitivity of Burgers' equation and other viscous conservation laws, see [66, 67, 68, 69, 70, 105, 106] and the references therein. Here we briefly summarize the results for Burgers' equation (5.9). Based on the asymptotic expansions of (5.10) and (5.11), it can be shown

that if the viscosity ν is small and δ satisfies

$$\delta = O\left(e^{-a/\nu}\right), \quad \text{as } \delta, \nu \downarrow 0 \quad (5.13)$$

for some constant $a \in (0, 1)$ which does not depend on δ or ν , then the position of the transition layer, defined as the zero of the solution profile $u(z) = 0$, varies on a transcendently slow time scale

$$t^* = te^{-a/\nu}. \quad (5.14)$$

The limit of the transition layer position at steady state is

$$z_{as} = 1 + \nu \ln(\delta/2), \quad t^* \rightarrow \infty. \quad (5.15)$$

The asymptotic relation (5.13) implies that δ is transcendently small (in the sense of asymptotic analysis) compared to ν , but dominates $e^{-1/\nu}$ as $\nu \downarrow 0$. Equation (5.15) shows that this transcendently small perturbation δ leads to a measurable, i.e. order one, effect on the final location of the transition layer. This phenomenon is called *supersensitivity*.

Direct numerical simulations

Although numerical solutions can be obtained by solving the exact solutions (5.10) and (5.11), it is nontrivial to construct robust initial conditions that guarantee convergence of the iterative solvers in the parameter range of supersensitivity. Hence we seek high accurate numerical solutions by integrating Burgers' equation (5.9) directly. Equation (5.9) is integrated by the semi-implicit scheme. Since we are only interested in the steady-state solution, a first-order scheme is employed.

$$\frac{u^{n+1} - u^n}{\Delta t} + (uu_x)^n = \nu u_{xx}^{n+1}, \quad (5.16)$$

where the superscript n denotes the time level $t^n = n\Delta t$. However, high resolution is required in space in order to capture accurately the location of the transition layer, which is 'supersensitive' to the small perturbation on the boundary condition.

In [33], Garbey and Kaper used a domain decomposition method with two nonover-

lapping subdomains, where the interface is adaptively located near the position of the transition layer. The Chebychev collocation method is employed and they found that with $N = 39$ collocation points in each subdomain the computed location of transition layer converges with three significant digits.

In this work we employ the spectral/ hp element method that combines the high accuracy of traditional spectral methods and the flexibility of mesh control from finite element methods [63]. Improved solution can be obtained by either redistributing the elements nonuniformly across the computational domain (h -refinement) or increasing the order of polynomials within each element (p -refinement), or both (hp -refinement). Thus, spectral element methods offer a dual-path of convergence. Here we employ the modal-basis, continuous-Galerkin method, where Jacobi polynomials are used as the basis polynomials within elements (see [63] for details).

In Figure 1.1 the steady state solution of (5.9) with $\nu = 0.05$ is shown. The solid line is the perturbed solution with $\delta = 0.01$, and the unperturbed solution with $\delta = 0$ is shown in dashed line for reference. Also shown in the figure is the distribution of five elements. The first element occupies $(-1, -0.2)$ and the rest divide the interval $(-0.2, 1)$ equally. Smaller mesh size is used in the right half of the domain where the transition layer moves through. This mesh will be used throughout this paper, and better resolution is obtained by p -refinement, i.e. by increasing the basis polynomial order within each element. From Figure 1.1, we can see clearly that with perturbation δ as small as 0.01, the location of the transition layer, defined as the zero of the solution $u(z) = 0$, is of order one. Specifically, we obtain $z = 0.73746$ in this case.

Computations are conducted for different magnitudes of perturbation δ , and with different viscosity ν . To ensure steady states are reached, we require $du/dt \simeq (u^{n+1} - u^n)/\Delta t < 10^{-12}$. Systematic p -refinement was conducted by increasing the order N of the basis polynomials in each element until resolution-independent solutions in space are obtained. In these computations we require the location of the transition layer to converge to eight significant digits, which in most cases require 20th-order ($N = 20$) spectral elements. In Table 5.1 and 5.2, we present locations of transition layer from our direct numerical computations and those from solution of the exact formulas (5.11), along with

the asymptotic estimates from (5.15) and results from [33] for comparison. It can be seen that the direct numerical solutions are accurate for up to seven digits when compared with the exact solution. Also, the numerical results from [33] and those of asymptotic estimates agree well with the exact solutions in general. Details of the resolution independence tests are reported in Appendix D.1 to verify the convergence of the simulations.

Table 5.1: Locations of transition layer of Burgers' equation with $\nu = 0.1$ subject to deterministic perturbation on boundary condition. z_{as} is the asymptotic estimate from (5.15), z_{GK} is the numerical result from [33], z is the present direct numerical computation, and z_{ex} is the numerical solution from exact formula (5.11).

δ	z_{as}	z_{GK}	z	z_{ex}
10^{-1}	0.700427	0.72464	0.72322525	0.72322525
10^{-2}	0.470176	0.47486	0.47492742	0.47492741
10^{-3}	0.240724	0.24133	0.24142361	0.24142361
10^{-4}	0.052606	0.05265	0.052669616	0.052669612
10^{-5}	0.005504	0.00537	0.0055085545	0.0055085559

Table 5.2: Locations of transition layer of Burgers' equation with $\nu = 0.05$ subject to deterministic perturbation on boundary condition. z_{as} is the asymptotic estimate from (5.15), z_{GK} is the numerical result from [33], z is the present direct numerical computation, and z_{ex} is the numerical solution from exact formula (5.11).

δ	z_{as}	z_{GK}	z	z_{ex}
10^{-1}	0.850213	0.86237	0.86161262	0.86161262
10^{-2}	0.735084	0.73755	0.73746015	0.73746015
10^{-3}	0.619955	0.62055	0.62030957	0.62030957
10^{-4}	0.504826	0.50485	0.50487263	0.50487264
10^{-5}	0.389696	0.38962	0.38970223	0.38970229

5.2.2 Stochastic Supersensitivity

Generalized polynomial chaos

Since the only random input in (5.9) is δ through the boundary condition, the one-dimensional finite-term generalized polynomial chaos expansion is employed

$$u(x, t; \omega) = \sum_{i=0}^M u_i(x, t) \Phi_i(\xi(\omega)), \quad (5.17)$$

where M is the highest order of the expansion. Depending on the distribution of the random variable ξ , different types of orthogonal polynomial bases are chosen. The appropriate correspondence is shown in Table 2.1.

In this paper, we assume δ has a continuous distribution with bounded support. Thus, the Jacobi-chaos, i.e. an expansion in terms of beta random variables is employed. This includes the special case of Legendre-chaos which is in terms of uniform random variables.

Upon substituting (5.17) into (5.9) and conducting a Galerkin projection onto the bases spanned by $\{\Phi_k\}_{k=0}^M$, we obtain

$$\frac{\partial u_k}{\partial t} + \frac{1}{\langle \Phi_k^2 \rangle} \sum_{i=0}^M \sum_{j=0}^M u_i \frac{\partial u_j}{\partial x} e_{ijk} = \nu \frac{\partial^2 u_k}{\partial x^2}, \quad \forall k \in [0, M], \quad (5.18)$$

where $e_{ijk} = \langle \Phi_i \Phi_j \Phi_k \rangle$. Equation (5.18) is a set of $(M + 1)$ coupled nonlinear equations. Here we employ again the semi-implicit scheme where the viscous terms are treated implicitly and the nonlinear terms explicitly.

The boundary conditions are also expanded in the form of (5.17). For example, if we assume $\delta \in (0, \epsilon)$ is a beta random variable $Be^{(\alpha, \beta)}(0, \epsilon)$ with $\alpha, \beta > -1$, the left boundary condition can be rewritten as

$$u(-1) = 1 + \delta = (1 + \bar{\delta}) + \sigma \xi, \quad (5.19)$$

where $\bar{\delta}$ is the mean of δ and $\xi \in (-1, 1)$ is a beta random variable $Be^{(\alpha, \beta)}(-1, 1)$ with

zero mean and probability density function (A.17)

$$f(\xi) = \frac{\Gamma(\alpha + \beta + 2)}{2^{\alpha+\beta+1}\Gamma(\alpha + 1)\Gamma(\beta + 1)}(1 - \xi)^\alpha(1 + \xi)^\beta.$$

Here σ scales as its standard deviation. Under this expression, the generalized polynomial chaos expansion for the left boundary condition takes the form

$$u_0(-1) = 1 + \bar{\delta}, \quad u_1(-1) = \sigma, \quad u_k(-1) = 0 \text{ for } k \geq 2. \quad (5.20)$$

The right boundary condition $u(1) = -1$ takes a simpler expansion form of $u_0(1) = -1$ and $u_k(1) = 0$ for $k \geq 1$.

Perturbation method

Again $\delta \in (0, \epsilon)$ is a random variable and we further assume $\epsilon \ll 1$. The left boundary condition is written as

$$u(-1) = 1 + \delta = \mu + \xi, \quad (5.21)$$

where $\mu = 1 + \bar{\delta}$ is the mean value and $\xi \in (-\epsilon/2, \epsilon/2)$. In the perturbative approach, the stochastic quantities are expanded via a Taylor series around the mean value of the random inputs, i.e.

$$u(x, t; \omega) = u_0(x, t) + \xi u_1(x, t) + \xi^2 u_2(x, t) + \dots \quad (5.22)$$

where

$$u_k(x, t) = k! \left. \frac{\partial^k u(x, t; \omega)}{\partial \xi^k} \right|_{\xi(\omega)=\mu}, \quad k = 0, 1, 2, \dots \quad (5.23)$$

Upon substituting the expansion (5.22) into (5.9) and equating the terms of different orders, under the assumption that $O(1) \gg O(\xi) \gg O(\xi^2) \gg \dots$, we obtain the following set of equations:

$$O(\xi^0): \quad \frac{\partial u_0}{\partial t} + u_0 \frac{\partial u_0}{\partial x} = \nu \frac{\partial^2 u_0}{\partial x^2}, \quad (5.24)$$

$$O(\xi^k): \quad L(u_k) = F_k(u_0, \dots, u_{k-1}) \quad k \geq 1, \quad (5.25)$$

where

$$L(u_k) = \frac{\partial u_k}{\partial t} + \frac{\partial(u_0 u_k)}{\partial x} - \frac{\partial^2 u_k}{\partial x^2}, \quad (5.26)$$

is a linear operator, and the right-hand-side terms are

$$F_1 = 0, \quad F_2 = -u_1 \frac{\partial u_1}{\partial x}, \quad F_3 = -\frac{\partial(u_1 u_2)}{\partial x}, \quad F_4 = -\frac{\partial(u_1 u_3)}{\partial x} - u_2 \frac{\partial u_2}{\partial x}, \dots \quad (5.27)$$

The boundary conditions are matched by the orders of ξ as well. For the left boundary, $u_0(-1) = \mu$, $u_1(-1) = 1$ and $u_k(-1) = 0$ for $k \geq 2$; for the right boundary, $u_0(1) = -1$ and $u_k(1) = 0$ for $k \geq 1$.

Monte Carlo Simulation

The brute-force Monte Carlo simulation (MC) is also employed, where samples of $\delta \in (0, \epsilon)$ are drawn according to its distribution and the deterministic solver is executed for each sample input. Two deterministic solvers are available: the iterative solver of the exact solution (5.10) and (5.11); and the direct numerical integration of (5.9). Due to the supersensitive nature of the problem, it is nontrivial to construct robust initial conditions for the iterative solver to converge for all the random realizations. Thus, we employ the direct integration of Burgers' equation. (Note that this is the traditional approach in Monte Carlo simulations as the exact solutions are not known in general.) This approach, however, is time consuming, especially for the supersensitivity problem which reaches steady states on a very slow time scale t^* (see equation (5.14)). Here we conduct MC simulations for one specific case of ν and δ to validate the results obtained by generalized polynomial chaos.

Numerical Results with Uniform Random Input

Here we present the numerical results of the viscous Burgers' equation subject to random perturbations on the boundary condition (5.9). We focus on the statistics of the location of the transition layer at steady state. In particular, we document the mean position of the transition layer and its standard deviation, denoted as \bar{z} and σ_z hereafter, respectively. The same mesh as shown in Figure 1.1 is used.

We assume $\delta \sim U(0, \epsilon)$ is a uniform random variable in $(0, \epsilon)$, which is a special case of beta random variable with $\alpha = \beta = 0$, i.e. $\delta \sim Be^{(0,0)}(0, \epsilon)$.

In Figure 5.21 and 5.22, the stochastic solutions by Legendre-chaos with $\delta \sim U(0, 0.1)$ are shown at two viscosity values $\nu = 0.05$ and $\nu = 0.1$, respectively. The mean solution profile, the standard deviation, and the upper and lower bounds of the solution are plotted. The upper and lower bounds are the deterministic solutions with boundary condition corresponding to the bounds of the random inputs, i.e. $\delta = 0.1$ and $\delta = 0$ in this case. They give the extreme solutions which constitute a rather wide response interval, and the mean location of the transition layer is not centered in the interval. The standard deviation peaks near the mean location of the transition layer. A 10% random input results in more than 40% peak response of the random output for $\nu = 0.05$. Also, the profiles of the standard deviation give us sharper estimations of the variation of the stochastic output.

The stochastic solutions in Figure 5.21 and 5.22 are obtained by high-order discretization, with 10th-order chaos expansion ($M = 10$) and 22th-order ($N = 22$) spectral elements. In Table 5.3, we tabulate the results at $\nu = 0.05$ and $\nu = 0.1$ under uniform random input $\delta \sim U(0, \epsilon)$, with different values of ϵ . Examples of the detailed resolution refinement tests are shown in Appendix D.2. Note that in these cases, even very small random perturbation of 0.1% can result in more than 30% stochastic response in the output.

Table 5.3: The mean locations (\bar{z}) of the transition layer and their corresponding standard deviations (σ_z) subject to uniform random perturbation $\delta \sim U(0, \epsilon)$ on the boundary condition.

ϵ	$\nu = 0.05$			$\nu = 0.1$		
	10^{-1}	10^{-2}	10^{-3}	10^{-1}	10^{-2}	10^{-3}
\bar{z}	0.81390488	0.69062979	0.57410655	0.62781226	0.38156021	0.15912335
σ_z	0.41403291	0.37864690	0.37322135	0.41400822	0.37591977	0.30390529

One of the advantages of the generalized polynomial chaos expansions is that the solutions take an analytical form in terms of the random inputs. Thus, one can in principle apply various manipulations to obtain the desired output statistics. Here we show the probability density functions of the solutions at various spatial locations, in particular, at

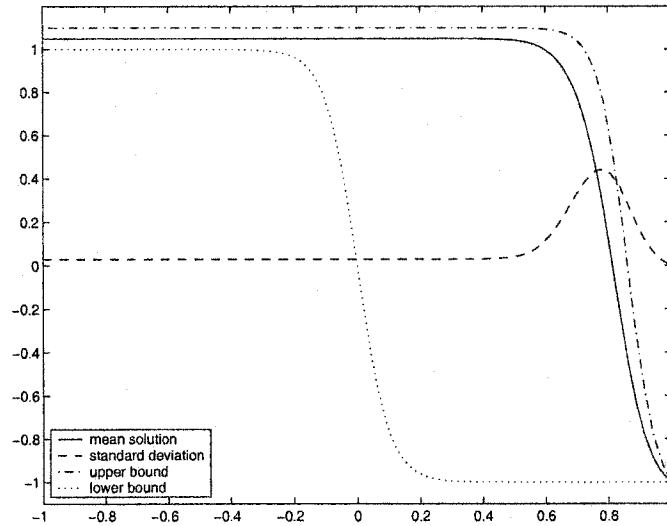


Figure 5.21: Stochastic solutions by Legendre-chaos with $\delta \sim U(0, 0.1)$ and $\nu = 0.05$. The upper and lower bounds are the deterministic solutions corresponding to the bounds of the random inputs, $\delta = 0.1$ and $\delta = 0$, respectively.

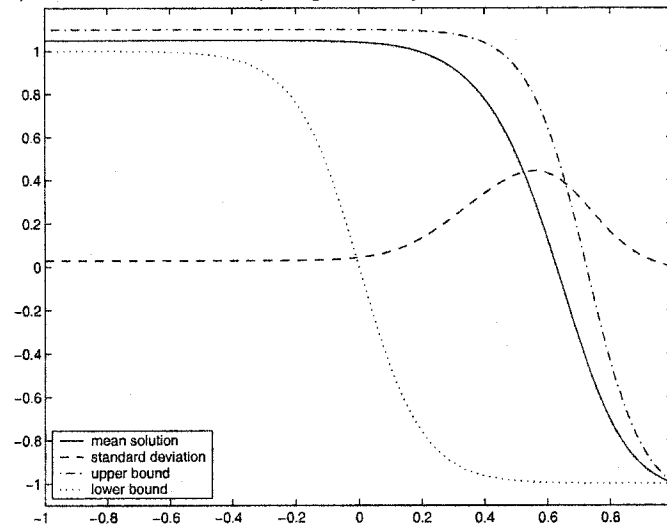


Figure 5.22: Stochastic solutions by Legendre-chaos with $\delta \sim U(0, 0.1)$ and $\nu = 0.1$. The upper and lower bounds are the deterministic solutions corresponding to the bounds of the random inputs, $\delta = 0.1$ and $\delta = 0$, respectively.

$x = 0.6, 0.7, 0.8$ and 0.9 which are located inside the transition layer. The results with $\delta \in U(0, 0.1)$ are shown in Figure 5.23 and 5.24. Figure 5.23 shows the results at $\nu = 0.05$. In this case the point $x = 0.6$ is located at the entrance of the transition layer, and the PDF here has a clear cutoff on the right and a tail on the left. The stochastic Gibb's phenomenon is present as we observe numerical oscillations. Inside the transition layer at $x = 0.7$ and $x = 0.8$, the PDFs are wider, with cutoff on the left as well. Near the end of the transition layer at $x = 0.9$, the PDF becomes narrower. Not all the PDFs are uniform. Figure 5.24 shows the results for $\nu = 0.1$. Here the first point $x = 0.6$ is already inside the transition layer. Again the PDF is sharp near the end of the layer at $x = 0.9$. From these results, we observe that the uniform random input at the left boundary is widened inside the transition layer, and sharpened near the end of the layer.

Monte Carlo simulations based on the direct numerical simulations of (5.9) are conducted for the case of $\nu = 0.05, \delta \sim U(0, 0.1)$ to validate the results obtained by generalized polynomial chaos. Because of the slow convergence $O(\sqrt{n})$ where n is the number of realizations, we relax the spatial resolutions as the sampling error will be predominant. In particular, we require $du/dt < 10^{-7}$ for steadiness and employ $N = 14$ spectral element. Deterministic results in Appendix D.1 show that at this spatial resolution the location of transition layer can be accurate up to five significant digits, which ensures the spatial errors to be subdominant. The results of Monte Carlo simulations are shown in Table 5.4. It is seen that as the number of realizations increases, the Monte Carlo solutions converge, nonmonotonically, to the solution of Legendre-chaos in Table 5.3. With $n = 10,000$, the mean and standard deviation agree with the Legendre-chaos results in three significant digits, and the difference is certainly within the sampling error range of the MC simulations. Furthermore, in Figure 5.25 and 5.26 we show the solution PDFs by Monte Carlo computation with $n = 10,000$ realizations at the four points $x = 0.6, 0.7, 0.8$, and 0.9 , along with the PDFs from Legendre-chaos expansion. We observe good agreements between the two sets of results, in spite of the Gibb's oscillations of Legendre-chaos near the sharp corner. These results serve as validations of the Legendre-chaos computations.

We also solve the case of $\nu = 0.05$ and $\delta \sim U(0, 0.1)$ by a perturbation method. The results are tabulated in Table 5.5. The spectral element order is $N = 20$ which ensures

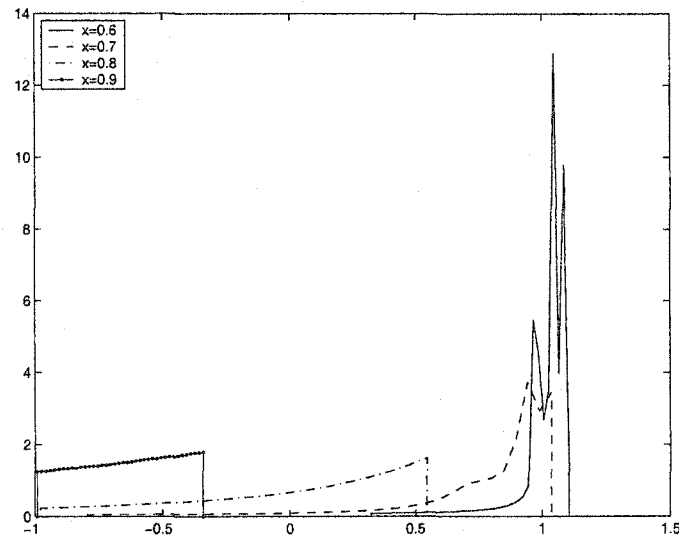


Figure 5.23: Probability density functions at various locations for $\delta \sim U(0,0.1)$ and $\nu = 0.05$. Gibbs's oscillations are present at $x = 0.6$ and 0.5 .

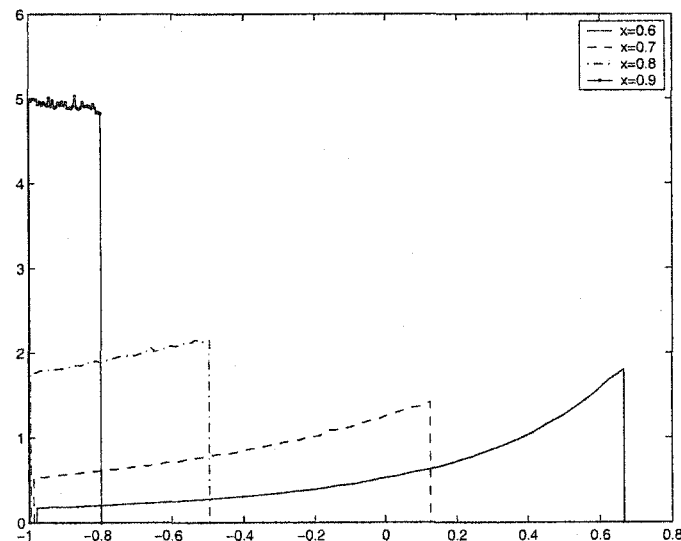


Figure 5.24: Probability density functions at various locations for $\delta \sim U(0,0.1)$ and $\nu = 0.1$.

Table 5.4: The mean location of the transition layer (\bar{z}) and its standard deviation (σ_z) from Monte Carlo simulations. n is the number of realizations, $\delta \sim U(0,0.1)$ and $\nu = 0.05$. Also shown are the converged Legendre-chaos solutions for comparison.

	$n = 100$	$n = 1,000$	$n = 2,000$	$n = 5,000$	$n = 10,000$	Legendre-chaos
\bar{z}	0.81853	0.81407	0.81448	0.81436	0.81397	0.81390488
σ_z	0.38705	0.41801	0.41699	0.41676	0.41418	0.41403291

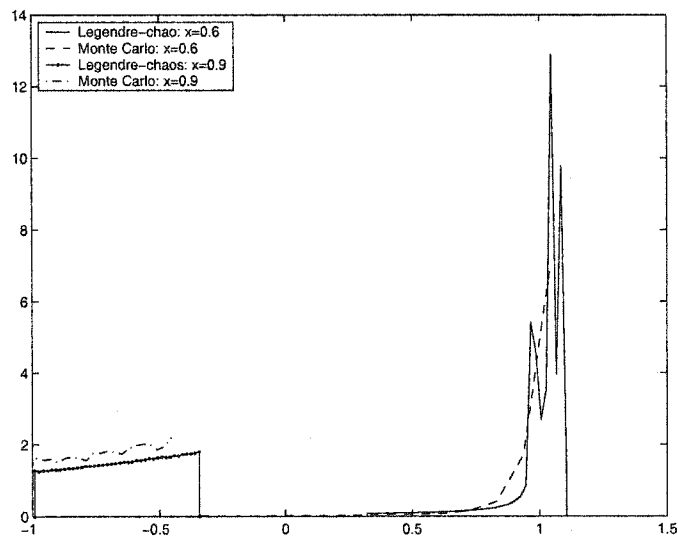


Figure 5.25: Probability density functions at $x = 0.6$ and $x = 0.9$ for $\delta \sim U(0, 0.1)$ and $\nu = 0.05$ by Monte Carlo simulation and Legendre-chaos expansion. (The oscillations at $x = 0.9$ are due to Gibbs' phenomenon.)

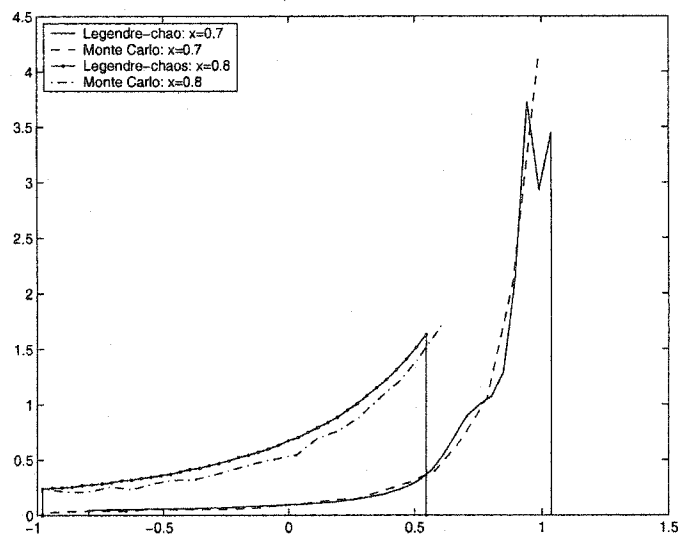


Figure 5.26: Probability density functions at $x = 0.7$ and $x = 0.8$ for $\delta \sim U(0, 0.1)$ and $\nu = 0.05$ by Monte Carlo simulation and Legendre-chaos expansion.

convergence in physical space. Up to a fourth-order perturbative expansion is employed. It is seen that while the mean location is close to the converged solution of polynomial chaos computation, the standard deviations have as high as 20% error compared to the chaos solution. Also, there is no clear sign of convergence as we increase the order of expansion. In fact, the first-order results are better than the rest, and the standard deviations of the third-, fourth-order results are noticeably worse than the first- and second-order results.

Table 5.5: The mean location of the transition layer (\bar{z}) and its standard deviation (σ_z) from the perturbation method. k is the order of the perturbative expansion, $\delta \sim U(0, 0.1)$ and $\nu = 0.05$. Also shown are the converged results from Legendre-chaos.

	$k = 1$	$k = 2$	$k = 3$	$k = 4$	Legendre-chaos
\bar{z}	0.82316323	0.82381706	0.82381706	0.82379866	0.81390488
σ_z	0.34931667	0.34896352	0.32800483	0.32801031	0.41403291

Two reasons can be attributed to the poor resolution of the perturbation method. First, although the random input is only 10% in maximum value, the response of the solution has fluctuations as high as 40%, as shown by the generalized polynomial chaos computation. This is clearly out of the effective regime of perturbation methods, and explains the relatively poor results, especially in standard deviation. Second, the nature of perturbative approach does not guarantee convergence as one increases the order of expansion. In fact, for a given magnitude of perturbation, there exists an optimal expansion order that gives the best result, see for example, [88, 89, 96, 120]. This is a well-known fact in asymptotic analysis, and it appears that the first-order expansion is optimal in this case.

Numerical Results with ‘Truncated’ Gaussian Random Input

In this section we model the random input at boundary with a ‘Gaussian-like’ distribution. We employ the ‘truncated Gaussian’ model $G^{(\alpha, \beta)}(a, b)$ where (a, b) is the bounded support of the distribution (see Appendix C). Here we employ the fifth-order Jacobi-chaos model with $\alpha = \beta = 10$, as shown in Figure C.3.

In Table 5.6 we show the mean location of the transition layer and its standard devi-

ation with $\delta \sim G^{(10,10)}(0, 0.1)$ as the random perturbation on the left boundary condition of (5.9). These solutions are obtained by 9th-order Jacobi-chaos with $\alpha = \beta = 10$ ($M = 9$) and 22th-order spectral elements ($N = 22$) to ensure the solutions converge to eight significant digits. Compared to the uniform perturbation $\delta \sim U(0, 0.1)$, under ‘Gaussian’ perturbation $\delta \sim G^{(10,10)}(0, 0.1)$ the mean location of transition layer is further to the right, but with much smaller standard deviation.

Table 5.6: The mean location of the transition layer (\bar{z}) and its standard deviation (σ_z) with truncated Gaussian random inputs $\delta \sim G^{(10,10)}(0, 0.1)$, for $\nu = 0.05$ and $\nu = 0.1$.

	$\nu = 0.05, \delta \sim G^{(10,10)}(0, 0.1)$	$\nu = 0.1, \delta \sim G^{(10,10)}(0, 0.1)$
\bar{z}	0.82217889	0.64435795
σ_z	0.13195896	0.13367561

The solutions with $\delta \sim G^{(10,10)}(0, 0.1)$ are shown in Figure 5.27 and 5.28, for $\nu = 0.05$ and $\nu = 0.1$, respectively. The corresponding PDF of the solutions at locations $x = 0.6, 0.7, 0.8$ and $x = 0.9$ are shown in Figure 5.29 and 5.30. Again, point $x = 0.6$ is located at the beginning of the transition layer for $\nu = 0.05$. We observe from Figure 5.29 that the distribution is widened inside the transition layer at $x = 0.7$ and $x = 0.8$, and is sharpened near the end of the layer at $x = 0.9$. This sharpening process is clearly seen from Figure 5.30, which is for the case of $\nu = 0.1$. In this case, the first point $x = 0.6$ is inside the transition layer. Since the random inputs at the boundary are extremely close to Gaussian, we naturally compare the PDFs at these locations to Gaussian distributions. In Figure 5.31 and 5.32, the PDFs at these locations for $\nu = 0.05$ are shown. Also shown with dashed lines are the reference Gaussian PDFs obtained at these locations with same mean values and standard deviations. It is seen that except at $x = 0.9$, the distributions are non-Gaussian. The PDFs are skewed and with clear cutoff at the tails. Near the end of the transition layer at $x = 0.9$, the skewness is smoothed and the distribution becomes close to Gaussian. (see Figure 5.32). Note that although the PDF is close to Gaussian, it is *not* Gaussian as it does not possess long tails. In Figure 5.33 and 5.34, the comparisons of the PDFs at these locations are shown for $\nu = 0.1$, and we observe similar results.

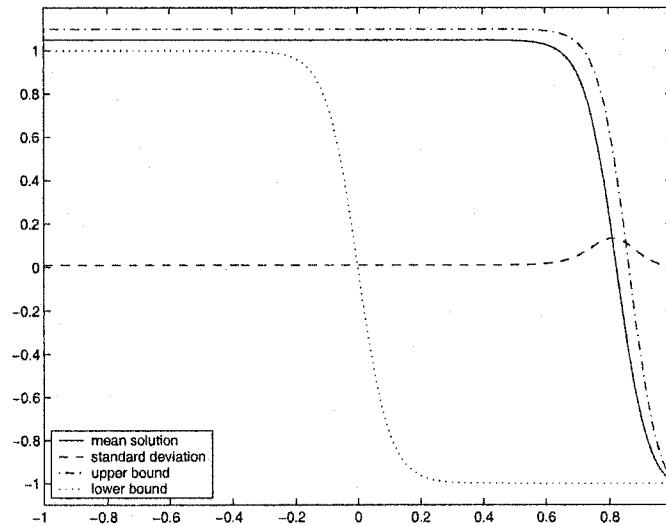


Figure 5.27: Stochastic solution by Jacobi-chaos ($\alpha = \beta = 10$) with $\delta \sim G^{(10,10)}(0, 0.1)$ and $\nu = 0.05$. The upper and lower bounds are the deterministic solutions corresponding to the bounds of the random inputs $\delta = 0.1$ and $\delta = 0$, respectively.

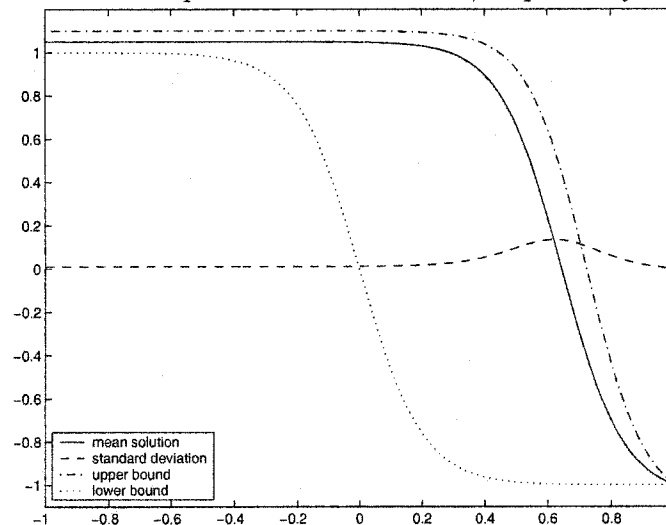


Figure 5.28: Stochastic solution by Jacobi-chaos ($\alpha = \beta = 10$) with $\delta \sim G^{(10,10)}(0, 0.1)$ and $\nu = 0.1$. The upper and lower bounds are the deterministic solutions corresponding to the bounds of the random inputs $\delta = 0.1$ and $\delta = 0$, respectively.

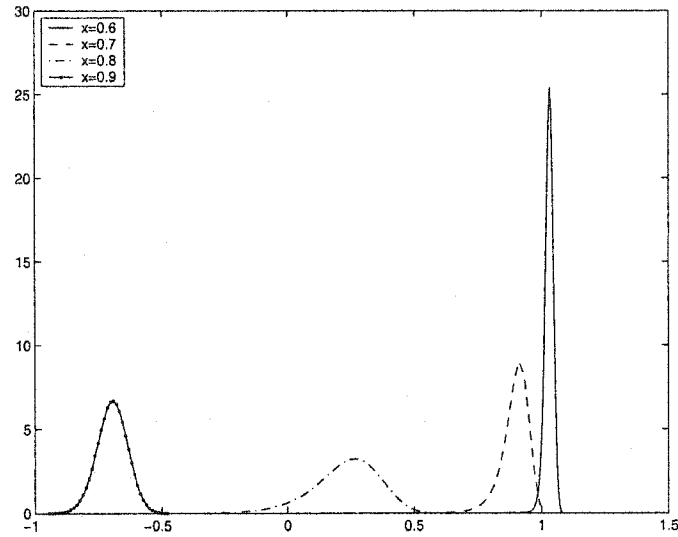


Figure 5.29: Probability density functions at various locations ($\delta \sim G^{(10,10)}(0, 0.1)$ and $\nu = 0.05$).

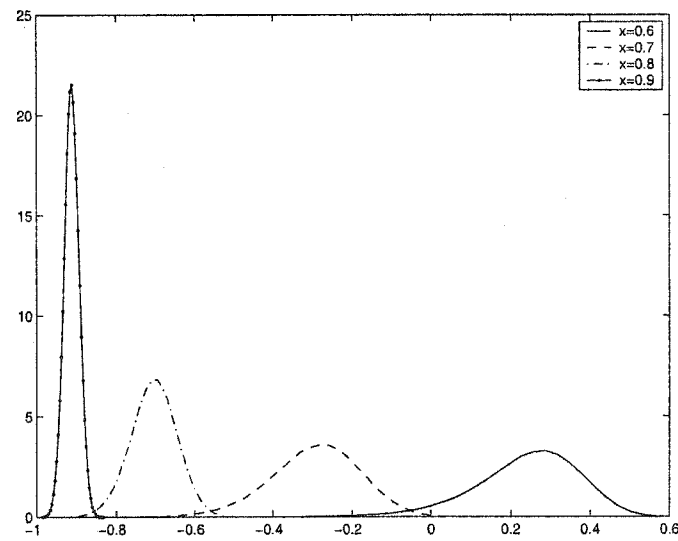


Figure 5.30: Probability density functions at various locations ($\delta \sim G^{(10,10)}(0, 0.1)$ and $\nu = 0.1$).

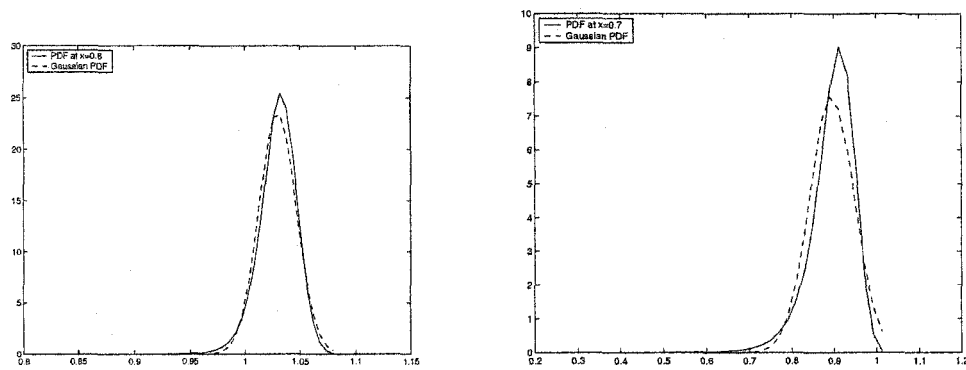


Figure 5.31: Probability density functions with $\nu = 0.05$, $\delta \sim G^{(10,10)}(0,0.1)$. Left: $x = 0.6$, Right: $x = 0.7$.

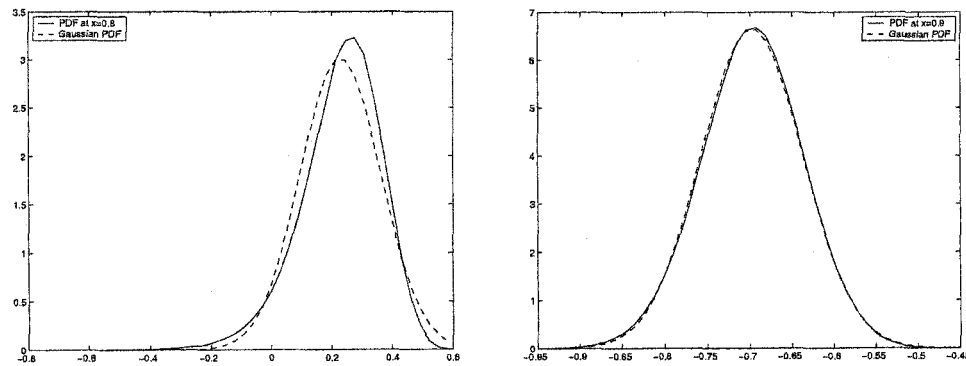


Figure 5.32: Probability density functions with $\nu = 0.05$, $\delta \sim G^{(10,10)}(0,0.1)$. Left: $x = 0.8$, Right: $x = 0.9$.

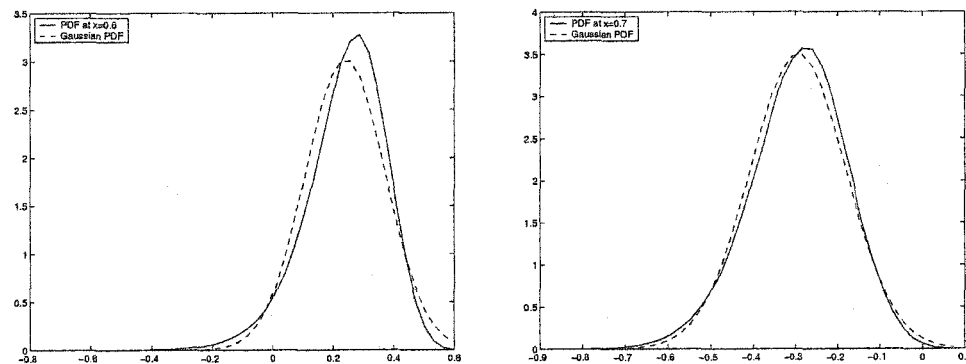


Figure 5.33: Probability density functions with $\nu = 0.1$, $\delta \sim G^{(10,10)}(0,0.1)$. Left: $x = 0.6$, Right: $x = 0.7$.

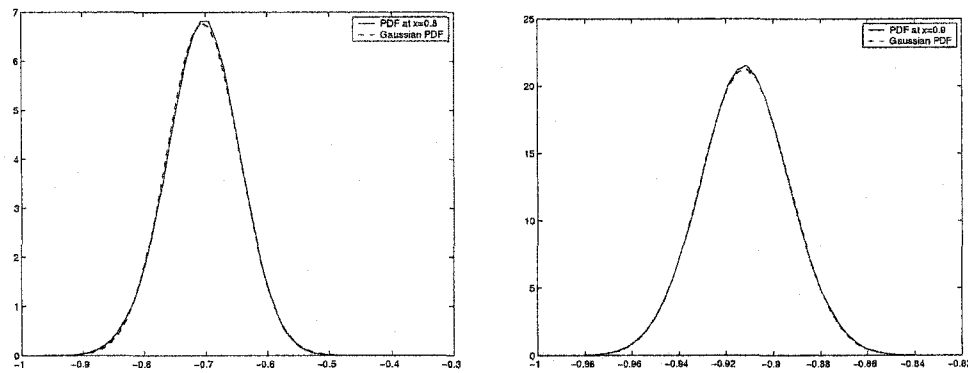


Figure 5.34: Probability density functions with $\nu = 0.1$, $\delta \sim G^{(10,10)}(0, 0.1)$. Left: $x = 0.8$, Right: $x = 0.9$.

Summary

In this paper the supersensitivity of the viscous Burgers' equation subject to small perturbations on the boundary condition was studied numerically. We presented the detailed simulations for both the *deterministic* and *stochastic* supersensitivity problems. High-resolution stochastic simulations are conducted by high-order spectral/*hp* element method in physical space, and high-order generalized polynomial chaos expansions in random space. Extensive numerical experiments are conducted to ensure the results are accurate and convergent.

It is found that small random perturbations on the upstream boundary condition can result in *order one* changes on the eventual mean location of the transition layer. The uncertainty of this transition layer, measured by the standard deviation of its mean location, is also high. As high as 30% output uncertainty can be obtained by only 0.1% random input. The generalized polynomial chaos expansion is shown to be capable of capturing this highly nonlinear problem accurately. Its convergence is demonstrated by resolution refinements both in physical space and random space. Its accuracy is verified by conducting Monte Carlo simulations. Perturbation methods of up to fourth-order expansions are also employed. The resolution, however, is poor, due to its inherent limitations. High-order perturbation methods do not offer advantages compared to first-order method, at least for this particular problem.

The stochastic supersensitivity problem is a natural extension of its well-studied de-

terministic counterpart. It is a highly nonlinear problem where small random inputs can result in large stochastic outputs, and ignoring the uncertain inputs will completely “miss the picture”. We expect that similar problems will arise in compressible fluid mechanics problems.

Chapter 6

Incompressible Navier-Stokes Equations

In this chapter we present the solution procedure for solving the stochastic Navier-Stokes equations by generalized polynomial chaos expansion. The randomness in the solution can be introduced through boundary conditions, initial conditions, forcing, etc..

6.1 Stochastic Formulation

6.1.1 Governing Equations

We employ the incompressible Navier-Stokes equations

$$\nabla \cdot \mathbf{u} = 0, \quad (6.1)$$

$$\frac{\partial \mathbf{u}}{\partial t} + (\mathbf{u} \cdot \nabla) \mathbf{u} = -\nabla \Pi + Re^{-1} \nabla^2 \mathbf{u}, \quad (6.2)$$

where Π is the pressure and Re the Reynolds number. All flow quantities, i.e., velocity and pressure, are considered stochastic processes.

$$\mathbf{u} = \mathbf{u}(\mathbf{x}, t; \omega); \quad \Pi = \Pi(\mathbf{x}, t; \omega). \quad (6.3)$$

We then apply the finite-term generalized polynomial chaos expansion, (2.23), to these quantities and obtain

$$\mathbf{u}(\mathbf{x}, t; \omega) = \sum_{i=0}^M \mathbf{u}_i(\mathbf{x}, t) \Phi_i(\boldsymbol{\xi}(\omega)); \quad \Pi(\mathbf{x}, t; \omega) = \sum_{i=0}^M \Pi_i(\mathbf{x}, t) \Phi_i(\boldsymbol{\xi}(\omega)), \quad (6.4)$$

By substituting (6.4) into Navier-Stokes equations ((6.1) and (6.2)) and conducting a Galerkin projection onto each polynomial basis, we obtain for each $k = 0, \dots, M$,

$$\nabla \cdot \mathbf{u}_k = 0, \quad (6.5)$$

$$\frac{\partial \mathbf{u}_k}{\partial t} + \frac{1}{\langle \Phi_k^2 \rangle} \sum_{i=0}^M \sum_{j=0}^M e_{ijk} [(\mathbf{u}_i \cdot \nabla) \mathbf{u}_j] = -\nabla \Pi_k + Re^{-1} \nabla^2 \mathbf{u}_k, \quad (6.6)$$

where $e_{ijk} = \langle \Phi_i \Phi_j \Phi_k \rangle$. The set of equations consists of $(P + 1)$ system of ‘Navier-Stokes-like’ equations for each random mode coupled through the convective terms.

6.1.2 Numerical Formulation

We employ the semi-implicit high-order fractional step method, which for the standard deterministic Navier-Stokes equations ((6.1) and (6.2)) has the form [62]:

$$\frac{\hat{\mathbf{u}} - \sum_{q=0}^J \alpha_q \mathbf{u}^{n-q}}{\Delta t} = -\sum_{q=0}^J \beta_q [(\mathbf{u} \cdot \nabla) \mathbf{u}]^{n-q}, \quad (6.7)$$

$$\frac{\hat{\mathbf{u}} - \hat{\mathbf{u}}}{\Delta t} = -\nabla \Pi^{n+1}, \quad (6.8)$$

$$\frac{\gamma_0 \mathbf{u}^{n+1} - \hat{\mathbf{u}}}{\Delta t} = Re^{-1} \nabla^2 \mathbf{u}^{n+1}, \quad (6.9)$$

where J is order of accuracy in time and α, β and γ are integration weights. A pressure Poisson equation is obtained by enforcing the discrete divergence-free condition $\nabla \cdot \mathbf{u}^{n+1} = 0$

$$\nabla^2 \Pi^{n+1} = \frac{1}{\Delta t} \nabla \cdot \hat{\mathbf{u}}, \quad (6.10)$$

with the appropriate pressure boundary condition given as

$$\frac{\partial \Pi}{\partial n} = -\mathbf{n} \cdot \left[\frac{\hat{\mathbf{u}}}{\Delta t} + Re^{-1} \nabla \times \boldsymbol{\omega}^{n+1} \right], \quad (6.11)$$

where \mathbf{n} is the outward unit normal vector and $\boldsymbol{\omega} = \nabla \times \mathbf{u}$ is the vorticity. The method is stiffly-stable and achieves third-order accuracy in time; the coefficients for the integration weights can be found in table 4.1.

In order to discretize the stochastic Navier-Stokes equations, we apply the same approach to the coupled set of equations (6.5) and (6.6):

For each $k = 0, \dots, M$,

$$\frac{\hat{\mathbf{u}}_k - \sum_{q=0}^J \alpha_q \mathbf{u}_k^{n-q}}{\Delta t} = -\frac{1}{\langle \Phi_k^2 \rangle} \sum_{q=0}^J \beta_q \left[\sum_{i=0}^M \sum_{j=0}^M e_{ijk} (\mathbf{u}_i \cdot \nabla) \mathbf{u}_j \right]^{n-q}, \quad (6.12)$$

$$\frac{\hat{\hat{\mathbf{u}}}_k - \hat{\mathbf{u}}_k}{\Delta t} = -\nabla \Pi_k^{n+1}, \quad (6.13)$$

$$\frac{\gamma_0 \mathbf{u}_k^{n+1} - \hat{\hat{\mathbf{u}}}_k}{\Delta t} = Re^{-1} \nabla^2 \mathbf{u}_k^{n+1}. \quad (6.14)$$

The discrete divergence-free condition for each mode $\nabla \cdot \mathbf{u}_k^{n+1} = 0$ results in a set of consistent Poisson equations for each pressure mode

$$\nabla^2 \Pi_k^{n+1} = \frac{1}{\Delta t} \nabla \cdot \hat{\mathbf{u}}_k, \quad k = 0, \dots, M, \quad (6.15)$$

with appropriate pressure boundary condition derived similarly as in [62]

$$\frac{\partial \Pi_k}{\partial n} = -\mathbf{n} \cdot \left[\frac{\hat{\mathbf{u}}_k}{\Delta t} + Re^{-1} \nabla \times \boldsymbol{\omega}_k^{n+1} \right], \quad k = 0, \dots, M, \quad (6.16)$$

where \mathbf{n} is the outward unit normal vector along the boundary, and $\boldsymbol{\omega}_k = \nabla \times \mathbf{u}_k$ is the vorticity for each random mode.

6.2 Microchannel Flow

We consider a pressure-driven channel flow as shown in figure 6.1, where the boundary conditions are considered to be uncertain. The domain (see figure 6.1) has dimensions

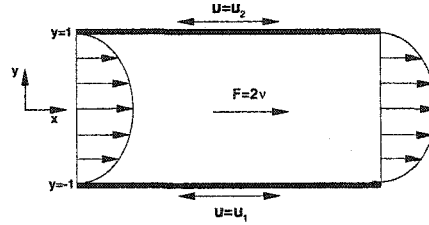


Figure 6.1: Schematic of the domain for pressure-driven channel flow with random boundary conditions.

such that $y \in [-1, 1]$ and $x \in [-5, 5]$. The pressure gradient, acting like a driving force, is equal to twice the kinematic viscosity, and thus for a no-slip wall condition the solution is a parabolic profile with centerline velocity equals unity.

6.2.1 Uniform Boundary Conditions

We assume that the boundary conditions at the two walls are uncertain with zero mean value, i.e., $u_1 = 0 + \sigma_1 \xi_1$ and $u_2 = 0 + \sigma_2 \xi_2$, where ξ_1 and ξ_2 are two independent random variables, and σ_1 and σ_2 are their corresponding standard deviations. Since the boundary conditions are uniform in space, with periodic boundary conditions specified in the streamwise direction, the nonlinear terms in the stochastic Navier-Stokes equations (6.6) vanish, and we obtain the exact solution

$$u(x, y) = (1 - y^2) + \frac{1 - y}{2} \sigma_1 \xi_1 + \frac{1 + y}{2} \sigma_2 \xi_2, \quad v(x, y) = 0. \quad (6.17)$$

The solution consists of a parabolic profile for the mean solution and two linear random modes (ξ_1 and ξ_2) linearly distributed across the channel width. Note the form of the exact solution is independent of the distribution type of random variables ξ_1 and ξ_2 .

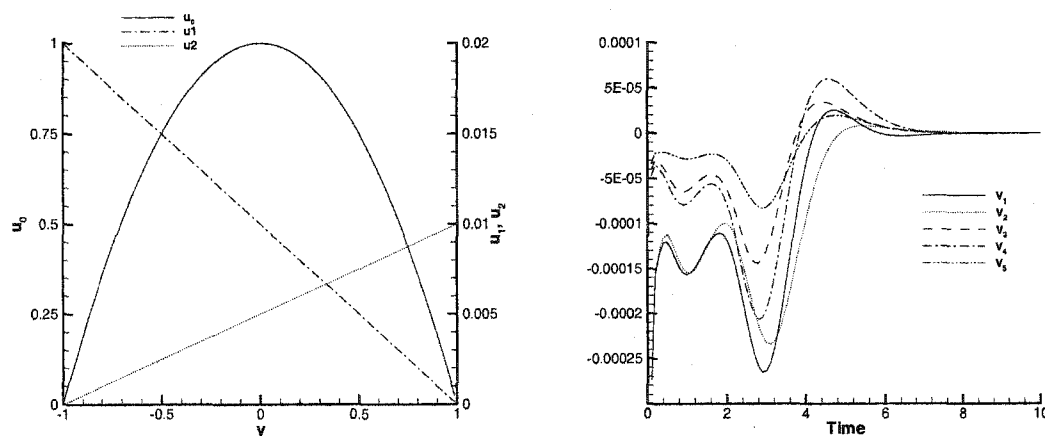


Figure 6.2: Solution of the pressure-driven channel with uniform Gaussian random boundary conditions; Left: the solution profile, Right: development of random modes of v -velocity with nonzero initial conditions.

On the left of figure 6.2 we show the solution profile across the channel. The ξ_1 and ξ_2 are two independent Gaussian random variables with $\sigma_1 = 0.02$ and $\sigma_2 = 0.01$. The two-dimensional ($n = 2$) Hermite-Chaos, the optimal Askey-Chaos in this case, is employed. Although the solution suggests that only a first-order expansion ($p = 1$) is needed, higher-order terms ($p > 1$) are included in the computation but are identically zero as expected. Another test is to set the initial condition of the flow to an arbitrary random state. We add perturbation terms to the exact solution (equation (6.17)) for each random mode in the form of $u_k(x, y, 0) = \alpha^p f(x, y)$ and $v_k(x, y, 0) = \alpha^p g(x, y)$ for $k = 0, \dots, M$. Here p is the order of the chaos expansions and $0 < \alpha < 1$ to ensure the decaying of the perturbation. On the right of figure 6.2 we show the time history of some dominant random modes of v -velocity at the center of the channel. It is seen that due to the nonlinear interactions between the random modes some of them are amplified in the early stage, but eventually all modes converge to the exact solution.

Computations with other types of random inputs have been conducted with their corresponding Askey-Chaos expansions. More specifically, we set ξ_1 and ξ_2 to be beta and

gamma random variables and employ the Jacobi-Chaos and Laguerre-Chaos, respectively. Similar results were obtained with the results shown in figure 6.2.

6.2.2 Non-uniform Boundary Conditions

Next we consider the case of non-uniform random boundary conditions, i.e. the wall boundary conditions at different locations are partially-correlated. The wall boundary conditions are assumed to be random processes with correlation function in the form

$$C(x_1, x_2) = \sigma^2 e^{-\frac{|x_1 - x_2|}{b}}, \quad (6.18)$$

where b is the *correlation length*.

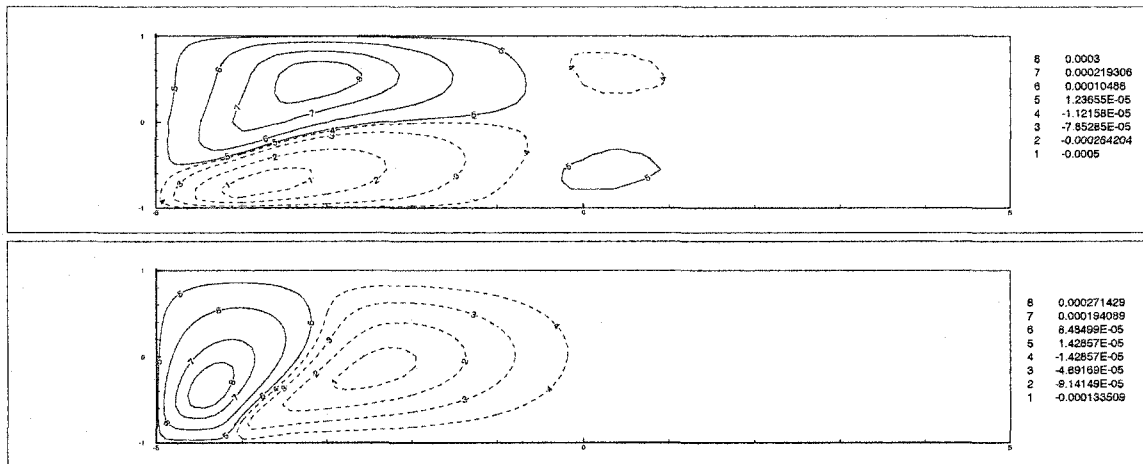


Figure 6.3: Deviation of mean solution from a parabolic profile in pressure-driven channel flow with partially-correlated random boundary conditions at the lower wall; Upper: u -velocity, Lower: v -velocity.

By setting a relatively large correlation length $b = 100$, the eigenvalues of the Karhunen-Loeve expansion are

$$\lambda_1 = 9.675354, \quad \lambda_2 = 0.1946362, \quad \lambda_3 = 0.05014117, \quad \dots$$

Due to the fast decay of the eigenvalues, we use the first two terms in the Karhunen-Loeve expansion given by equation (2.11). This results in a two-dimensional chaos expansion ($n = 2$). Resolution-independence checks were conducted and the fourth-order chaos

expansion ($p = 4$) were found to be sufficient to resolve the problem in the random space. Using equation (2.37) this results in a fifteen-term expansion ($M = 14$). Only the lower wall boundary condition is assumed to be uncertain with $\sigma = 0.1$, while the upper wall is stationary and deterministic. A parabolic velocity profile is specified at the inlet and zero Neumann condition at the outlet. A mesh with 10×2 elements is employed and basis Jacobi polynomials of sixth-order in each element results in resolution independent solution in space.

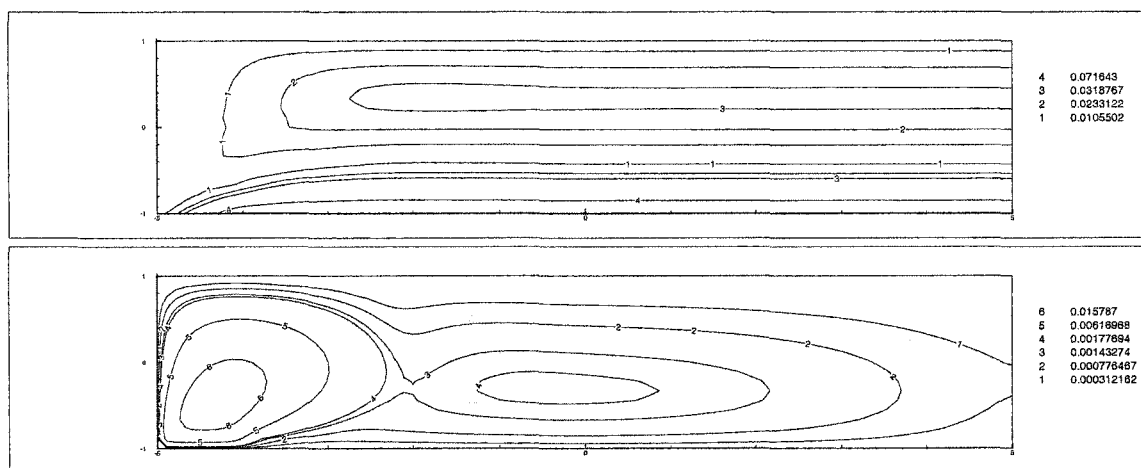


Figure 6.4: Contours of *rms* of u -velocity (upper) and v -velocity (lower).

We first consider the lower wall boundary condition a Gaussian random process and employ the Hermite-Chaos expansion. Figure 6.3 shows the velocity contour plot of the deviation of the mean solution at steady-state from a parabolic profile. The mean of u -velocity remains close to the parabolic shape and the mean of v -velocity, although small in magnitude, is non-zero. Figure 6.4 shows steady-state solutions of the *rms* (root-mean-square) of u and v -velocity. We see the development of a ‘stochastic boundary layer’ close to the lower wall. All the higher-order expansion terms are non-zero, which implies that although the random input is a Gaussian process, the solution output is *not* Gaussian. Since no analytic solution is available, Monte Carlo (MC) simulation is used to validate the result. Figure 6.5 shows the solution of mean velocity u and v along the centerline of the channel. It is seen that the Monte Carlo solution converges non-monotonically to the Hermite-Chaos result as the number of realizations increases. In this case, it is only

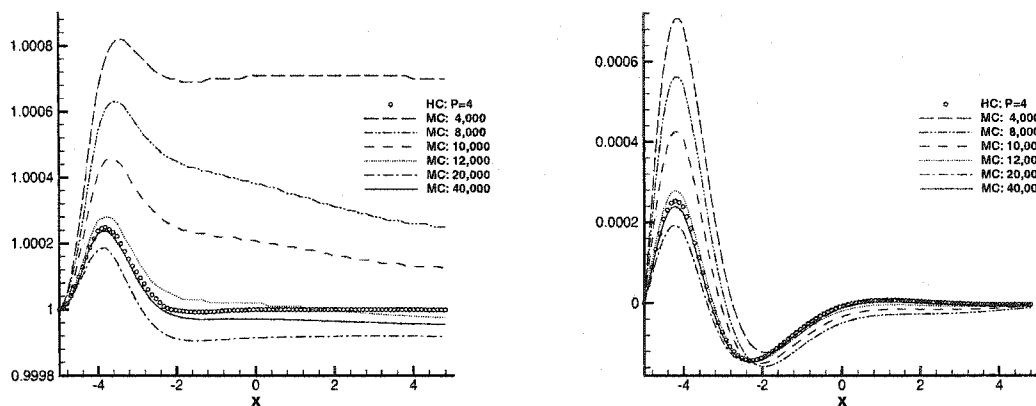


Figure 6.5: Monte Carlo (MC) and Hermite-Chaos (HC) solution of the mean velocities along the centerline of the channel; Left: u -velocity, Right: v -velocity.

after 40,000 realizations that Monte Carlo solution can capture the solution accurately, especially the nonlinear interactions close to the inlet. The polynomial chaos solver, with 15 terms in the expansions, is more than two thousands times faster than the Monte Carlo computation without using any special optimization techniques. In figure 6.6 the solution

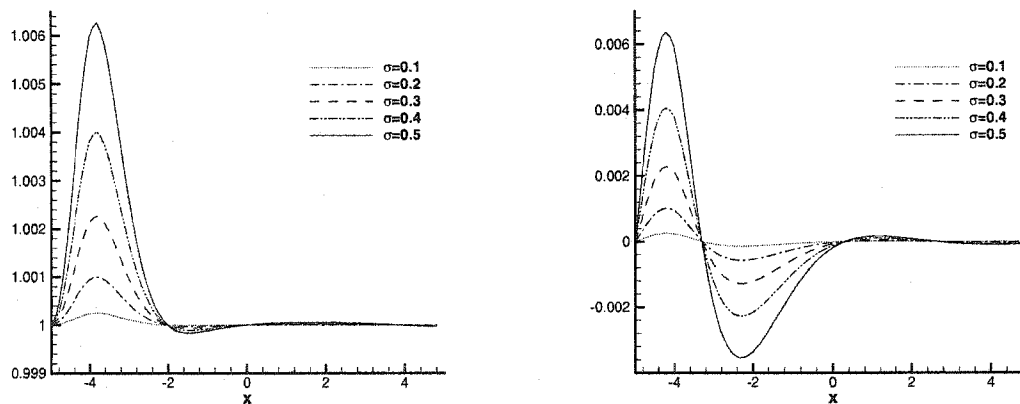


Figure 6.6: Hermite-Chaos solution of the mean velocities along the centerline of the channel with different σ ; Left: u -velocity, Right: v -velocity.

of the mean velocity along the centerline is shown corresponding to different values of σ . It can be seen that as the intensity of the input uncertainty σ increases the stochastic solution responses increase nonlinearly.

In figure 6.7 we plot the mean solution along the centerline of the channel with different types of stochastic inputs. Specifically, we assume the random processes of the low wall boundary condition are zero-mean Gaussian, uniform and exponential processes with the same exponential correlation structure (equation (6.18)) and fixed parameter $\sigma = 0.4$. The corresponding Askey-Chaos, i.e., the Hermite-, Legendre- and Laguerre-Chaos, respectively, are employed. The variance of the velocity, non-dimensionalized by the input variance σ^2 , is shown in figure 6.8. It is seen that the uniform random process results in a smoother solution with smaller variances due to the fact that the uniform distribution has finite support.

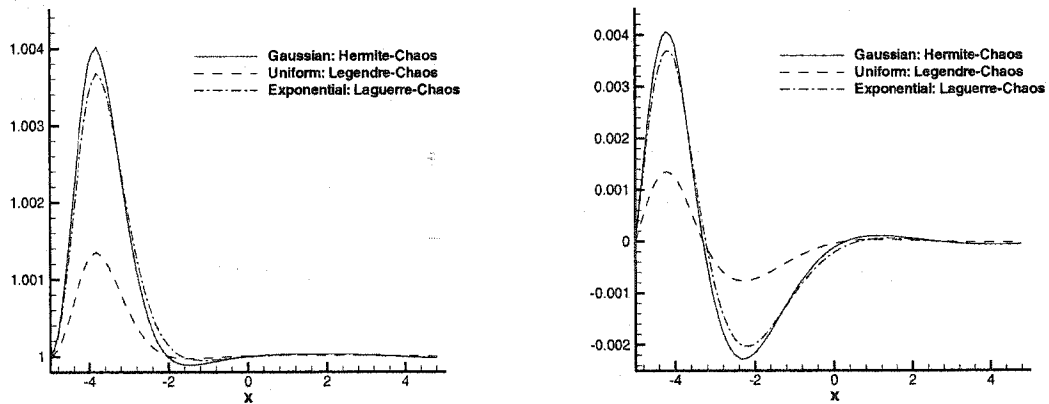


Figure 6.7: Chaos solution of mean velocities along the centerline of the channel with different types of input processes; Left: u -velocity, Right: v -velocity.

Figure 6.9 shows the solution of mean velocity along the centerline of the channel corresponding to *uniform* stochastic process as the lower wall boundary conditions, with the same correlation structure as above ($\sigma = 0.4$). The Legendre-Chaos expansion is employed. The Monte Carlo solution converges to the chaos solution; with 120,000 realizations it captures the nonlinear interactions near the inlet accurately. The Legendre-Chaos corresponds to dimension $n = 2$ and polynomial order $p = 4$, which according to the formula of equation (2.37) gives 15 terms in the expansion.

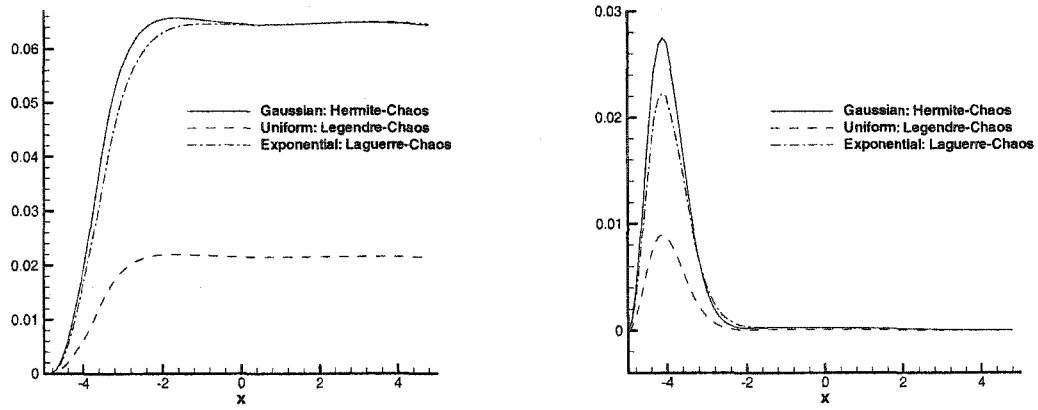


Figure 6.8: Chaos solution of variance along the centerline of the channel with different types of input processes; Left: variance of u -velocity, Right: variance of v -velocity.

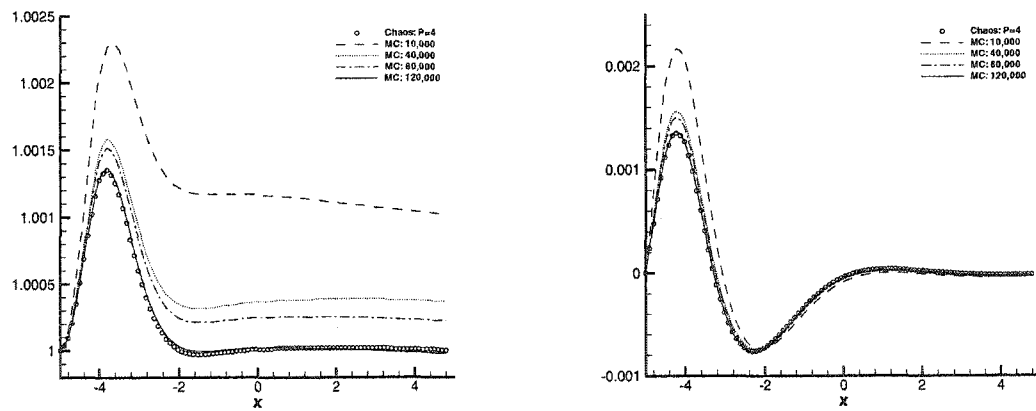


Figure 6.9: Monte Carlo (MC) and Legendre-Chaos solution of the mean velocities along the centerline of the channel with uniform stochastic inputs; Left: u -velocity, Right: v -velocity.

6.3 Flow Past a Circular Cylinder

In this section we simulate two-dimensional incompressible flow past a circular cylinder with random fluctuations superimposed to the free-stream. More specifically, the inflow takes the form $u_{in} = \bar{u} + g$, where g is a random variable or process. Here we focus on the Gaussian process and Hermite-Chaos solution. The computational domain is shown in figure 6.10. The size of the domain is $[-15, 25] \times [-9, 9]$ and the cylinder is at the origin $(0, 0)$ with diameter $D = 1$. The definition of Reynolds number is based on the mean value of the inflow velocity \bar{u} and the diameter of the cylinder. The domain consists of 412 triangular elements with periodic conditions specified in the crossflow direction. Sixth-order Jacobi polynomial in each element is observed to result in resolution-independent solution in space for Reynolds number less than 200. The Reynolds number is defined as $Re = U_\infty D / \nu$, where U_∞ is the inflow and ν the kinematic viscosity.

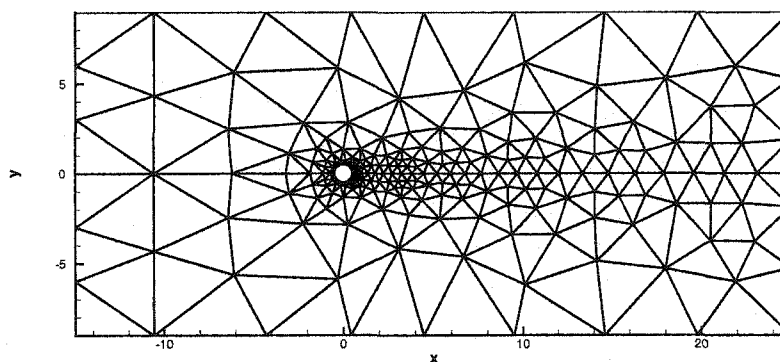


Figure 6.10: Schematic of the domain for flow past an elastically mounted circular cylinder.

6.3.1 Onset of instability

It is well known that for two-dimensional flow past a circular cylinder, the first critical Reynolds number is around $Re \sim 40$, where the flow bifurcates from steady state to periodic vortex shedding [125]. Here we study the effects of the upstream random perturbations close to this Reynolds number. We set $u_{in} = \bar{u} + \sigma\xi$, where ξ is a Gaussian random variable and σ is its standard deviation. The one-dimensional Hermite-Chaos expansion

is thus employed. The pressure at the rear stagnation point of the cylinder is extremely sensitive to the vortex shedding state and is monitored in our computation.

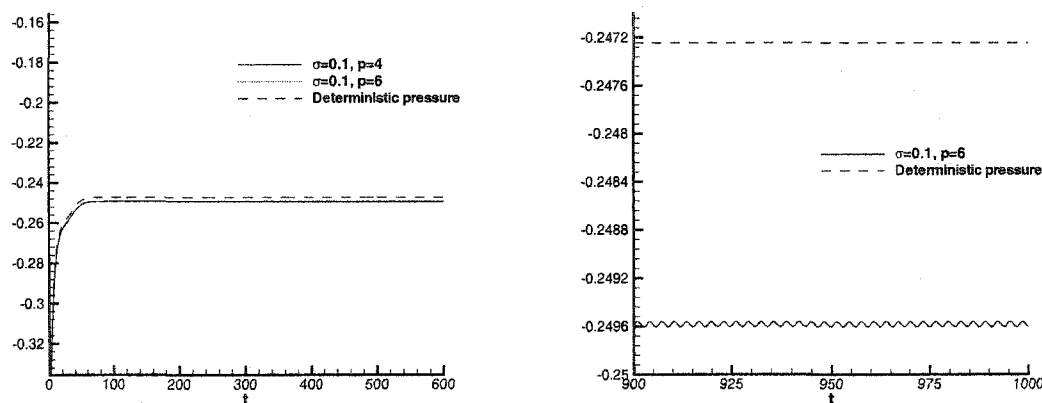


Figure 6.11: Time history of mean pressure at the rear stagnation point at $Re = 40$ (Gaussian perturbation with $\sigma = 0.1$); Left: The time history, Right: Close-up view.

Figure 6.11 shows the time history of the mean pressure at the rear stagnation point at $Re = 40$, which is close to the critical Reynolds number. Solution with fourth-order and sixth-order Hermite-Chaos are shown, together with the deterministic pressure history as reference. A negligible difference is observed between fourth-order and sixth-order chaos solutions (less than 0.1%). Thus, the solution can be considered as resolution-independent in the random space. In the close-up view we see that the 10% random perturbation ($\sigma = 0.1$) triggers an instability and the flow becomes weakly periodic, as opposed to the deterministic solution which remains steady.

Next, we lower further the inflow Reynolds number to $Re = 35$. In figure 6.12 we show the time history of the mean pressure signal at the rear stagnation point. Again, resolution independence checks show a negligible difference (less than 0.1%) in the solutions by fourth-order and sixth-order Hermite-Chaos. It is shown that at this Reynolds number a 10% random perturbation ($\sigma = 0.1$) is unable to trigger an instability and the flow remains steady. On the other hand, with a larger perturbation ($\sigma = 0.2$) the flow becomes weakly unsteady again.

These results suggest that the inflow random perturbations have noticeable effects

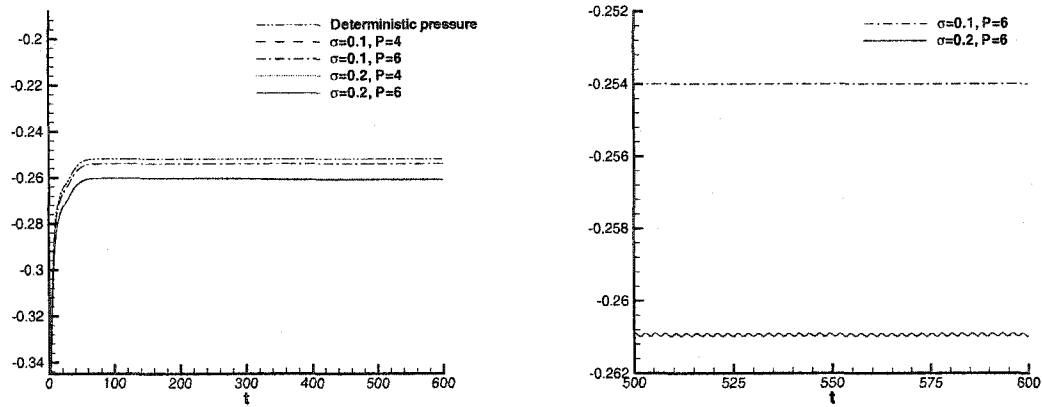


Figure 6.12: Time history of mean pressure at the rear stagnation point at $Re = 35$; Left: The time history, Right: Close-up view.

on the stability of the flow near its critical Reynolds number. In fact, the existence of upstream perturbation induces the instability and forces the transition to occur at lower Reynolds number. This study is similar to that of [58] where the convective instability is studied by introducing random perturbations at the inflow of the backward-facing step flow. Instead of running many realizations of the deterministic flow solver, here we can resolve the propagation of inflow uncertainty by chaos expansion in one single run of the stochastic solver.

6.3.2 Vortex Shedding

We consider another case at $Re = 100$ with freestream random velocity partially correlated. The inflow is $u_{in} = \bar{u} + g(y)$ where $g(y)$ is a Gaussian process with the exponential covariance kernel of equation (6.18) with $\sigma = 0.02$. Again, a relatively large correlation length is chosen ($b = 100$) so that the first two eigenmodes are adequate to represent the process by Karhunen-Loeve expansion (2.11). Thus, we employ a two-dimensional Hermite-Chaos expansion ($n = 2$) and fourth-order chaos ($p = 4$).

Figure 6.13 shows the pressure signal, together with the deterministic signal for reference (denoted as P_D in dotted line). We see that the stochastic *mean* pressure signal has a smaller amplitude and is out-of-phase with respect to the deterministic signal. Although

initially, the stochastic response follows the deterministic response, eventually there is a change in the Strouhal frequency as shown in figure 6.14. Specifically, the Strouhal frequency of the mean stochastic solution is slightly lower than the deterministic one and has a broader support.

In figure 6.15 we present velocity profiles along the centerline for the deterministic and the mean stochastic solution at the same time instant. We see that significant quantitative differences emerge even with a relatively small 2% uncertainty in the freestream. In figure 6.16 we plot instantaneous vorticity contours for the mean of the vorticity and compared it with the corresponding plot from the deterministic simulation; we observe a diffusive effect induced by the randomness. In figure 6.17 we plot contours of the corresponding *rms* of vorticity. It shows that the uncertainty influences the most interesting region of the flow, i.e., the shear layers and the near-wake but not the far-field.

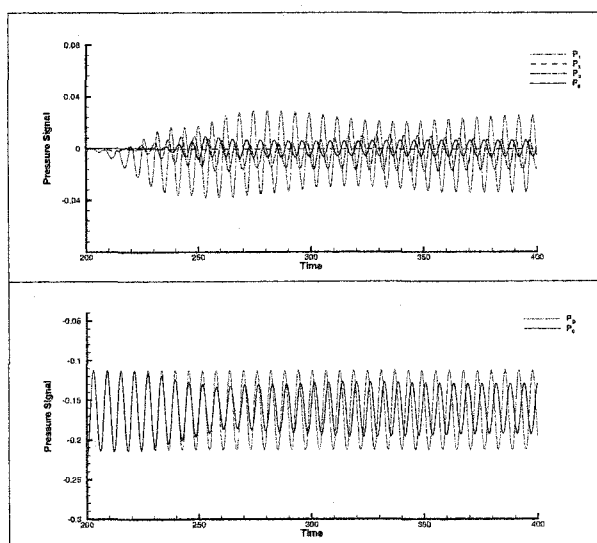


Figure 6.13: Pressure signal of cylinder flow with non-uniform Gaussian random inflow. Upper: High modes. Lower: Zero mode (mean).

6.4 Flow in a Grooved Channel

In this section we study two-dimensional incompressible flow in a periodically grooved channel, a typical model of a wall bounded flow with separation. Groove flows serve as a prototype in which the multiple interactions of free shear layers and steady or unsteady

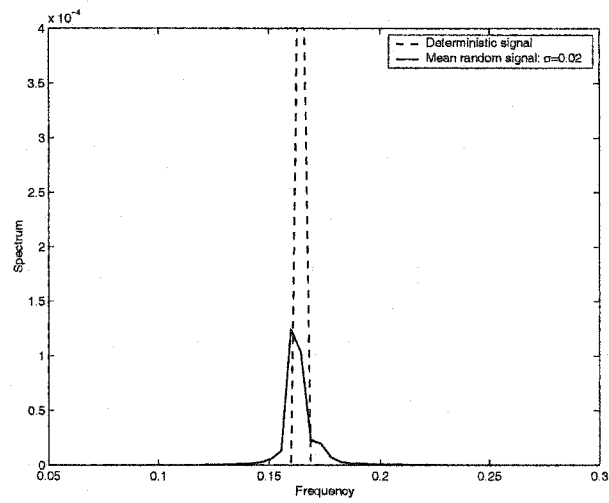


Figure 6.14: Frequency spectrum for the deterministic (high peak) and stochastic simulation (low peak).

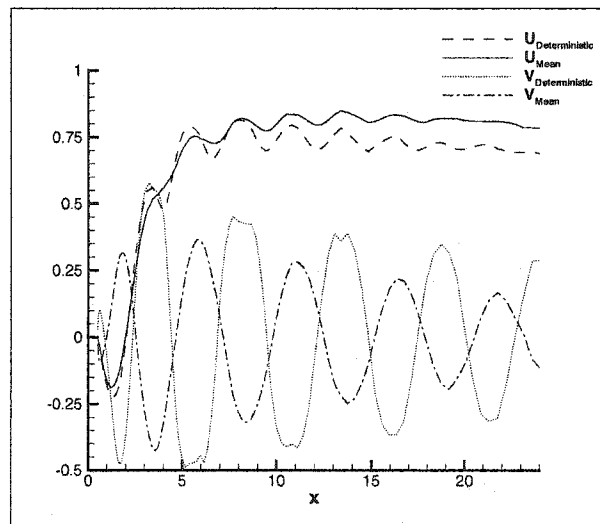


Figure 6.15: Instantaneous profiles of the two velocity components along the centerline (in the wake) for the deterministic and the mean stochastic solution.

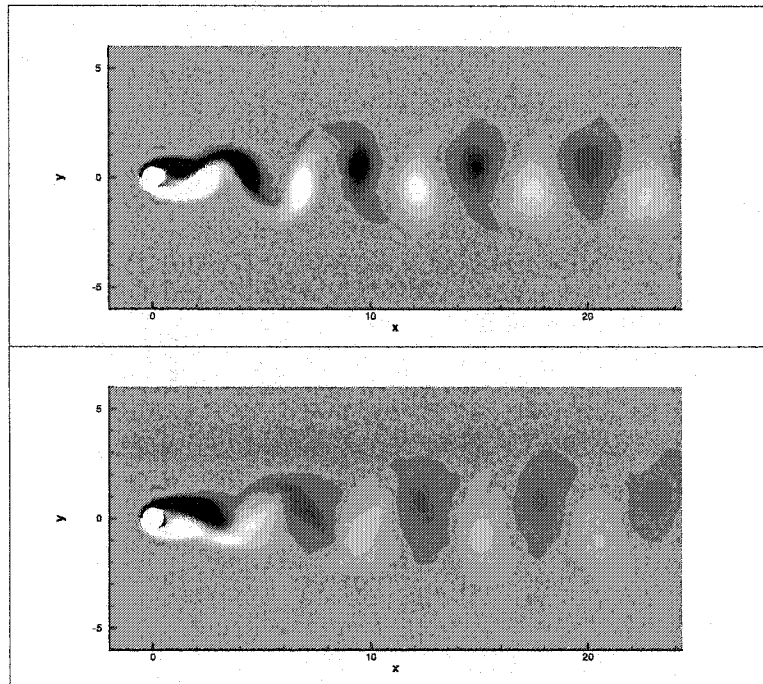


Figure 6.16: Instantaneous vorticity field : Upper - Deterministic solution with uniform inflow; Lower - Mean solution with non-uniform Gaussian random inflow.

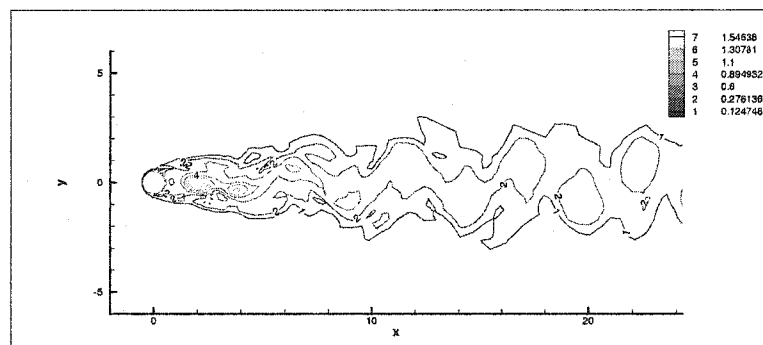


Figure 6.17: Instantaneous contours of *rms* of vorticity field with non-uniform Gaussian random inflow.

vortices can be investigated in great detail. Detailed stability analysis has been performed in [20, 36], and here we focus on the effect of uncertainty in boundary conditions on the critical Reynolds number.

In figure 6.18, the computational domain of the grooved channel is shown. The depth of the cavity is 1.75. The domain is discretized into 66 non-uniform elements, where the h -refinement is employed close to and inside the cavity. The boundary conditions are no-slip condition at the rigid walls and periodicity in the streamwise direction. The flow is driven via a forcing term $\mathbf{f} = (2\nu, 0)$, where ν is the kinematic viscosity. This is equivalent to the imposition of a constant mean pressure gradient. The equivalent pressure drop is scaled with the kinematic viscosity so that it maintains the flow rate (Q) approximately constant at different Reynolds numbers. The Reynolds number for this geometry is defined as

$$\text{Re} = 3Q/4\nu. \quad (6.19)$$

Since the mass flow is not known *a priori*, it is convenient to use the inverse viscosity and regard it as a reduced or modified Reynolds number:

$$r = 1/\nu. \quad (6.20)$$

A systematic resolution independence test was conducted, and it is found that the 6th-order spectral element is able to resolve the problem. In table 6.1 we show the correspondence between the Reynolds number (Re) and the modified Reynolds number (r) by high-order deterministic simulations. When $r = 275$, the flow becomes weakly periodic and the Reynolds number varies between 296.1 and 296.6. We further identify that the critical Reynolds number for the appearance of the first (Hopf) bifurcation, where the flow transits from steady state to weakly periodic state, is at $r = 270$, where $\text{Re} \approx 291.1$. This is consistent with the results from [20], where the first critical Reynolds number is reported to be around $\text{Re} \approx 300$.

Next we examine the effect of uncertainty in boundary conditions on the first critical

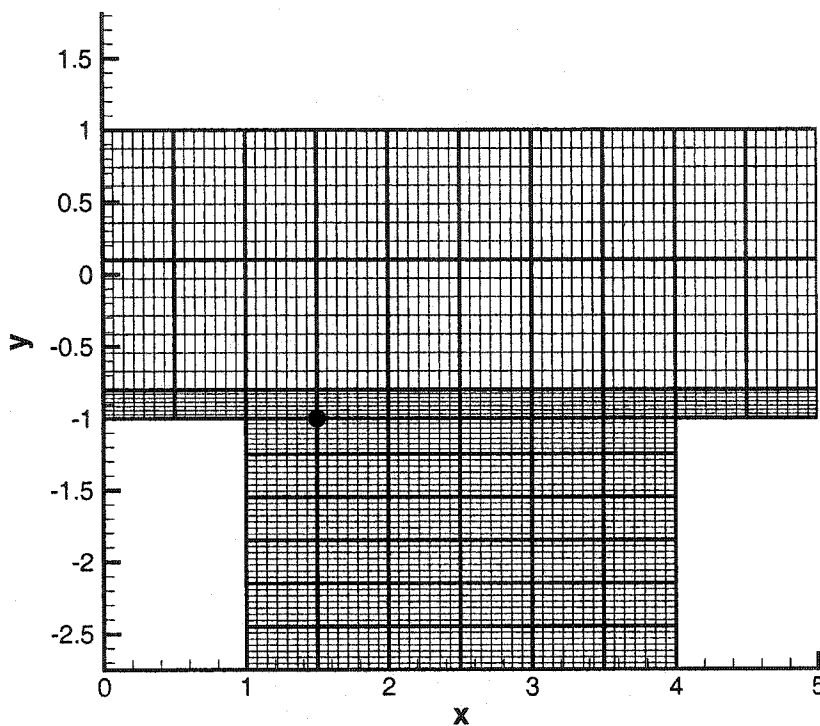


Figure 6.18: Flow in a grooved channel: the computational mesh. (The history point is shown as a solid dot.)

r	200	225	250	275
Re	217.3	243.7	270.1	(296.1, 296.6)

Table 6.1: Reynolds number (Re) and the modified Reynolds number (r) in a grooved channel (Equation (6.19) and (6.20)).

Reynolds number. Instead of no-slip condition, we assume a slip condition

$$u_T = \sigma \xi(\omega) \quad (6.21)$$

on the wall, where u_T denotes the tangential velocity along the wall, $\xi \sim U(-1, 1)$ is a uniform random variable and $\sigma > 0$ scales as its deviation. We applied this condition to the different segments of the solid walls of the grooved channel, and found that it has the most significant effect when applied to the top channel wall.

Figure 6.19 shows the time evolution of the mean velocities at the history point (shown in figure 6.18). The no-slip condition is employed at all solid walls, except at the top wall where (6.21) is applied with $\sigma = 0.1$. We observe that, after long-term integration, the flow fields become (weakly) periodic with a frequency $f \approx 0.1075$ (period $T \approx 9.30$). The modified Reynolds number is $r = 220$. The mean Reynolds number, calculated from (6.19) by the mean flow rate (\bar{Q}), is $\text{Re} \approx 238.6$. The corresponding deterministic flow with no-slip wall conditions is steady at this Reynolds number, as shown in figure 6.19 in dashed lines. By introducing the uncertain slip condition, the first critical Reynolds number reduces from 291.1 to 238.6. Hence, an approximately 18% reduction in critical Reynolds number for $\sigma = 0.1$.

In figure 6.20 and 6.21 we show the mean velocity fields and their standard deviations at time $t = 5,000$, respectively. We observe that the maximum of uncertainty in the u -velocity is close to the top boundary, as this is where the random input is. The standard deviation of the v -velocity shows a cell-structure, and the local maximum values are close the center of the channel, and behind the tip of the lower wall inside the cavity, which is where the shear layer resides.

The pattern in the standard deviation from figure 6.21 closely resembles the distorted (due to cavity) Tollmein-Schlichting (TS) wave pattern from [36]. In [36], it was demonstrated that the grooved channel instability is a process of the free-shear-layer destabilizing the otherwise stable Tollmien-Schlichting waves, and that the frequency of oscillation is dictated by the least stable mode of the TS wave. The frequency of TS wave is calculated

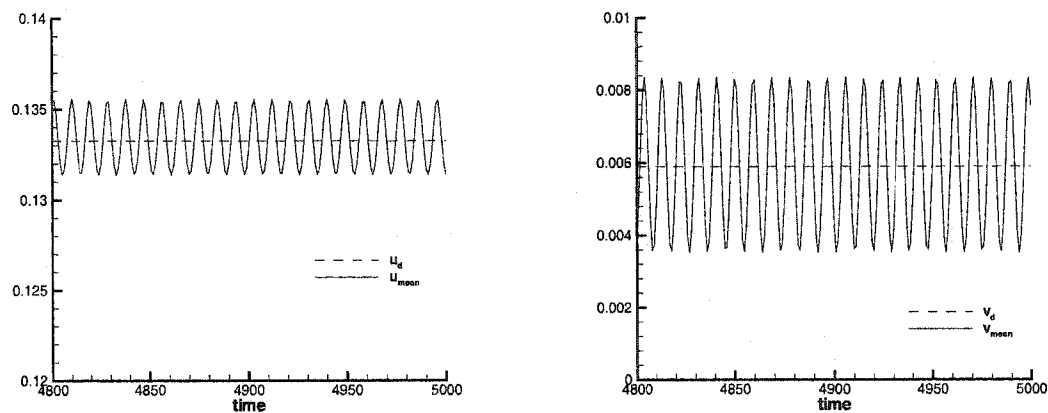


Figure 6.19: Evolution of mean velocity field at the history point (solid lines), with the reference deterministic results shown in dashed lines. $r = 220$ and $Re = 238.6$. Left: u -velocity, Right: v -velocity.

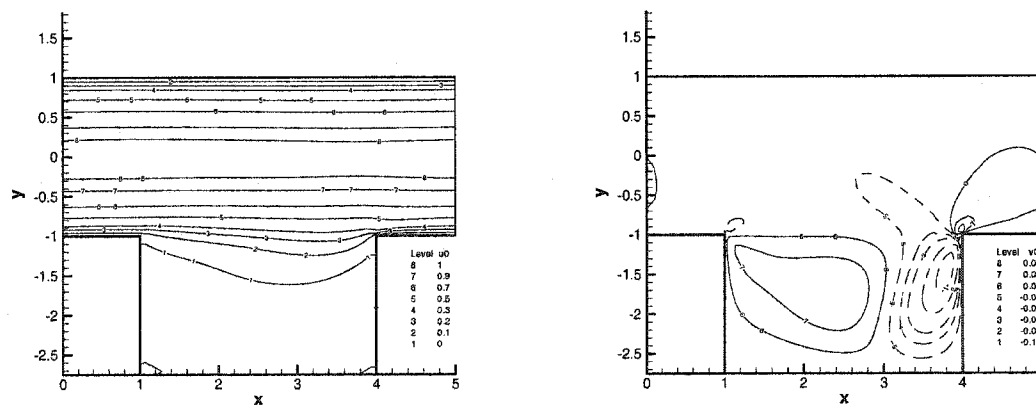


Figure 6.20: Mean velocity fields at $t = 5,000$. $r = 220$ and $Re = 238.6$. Left: u -velocity, Right: v -velocity.

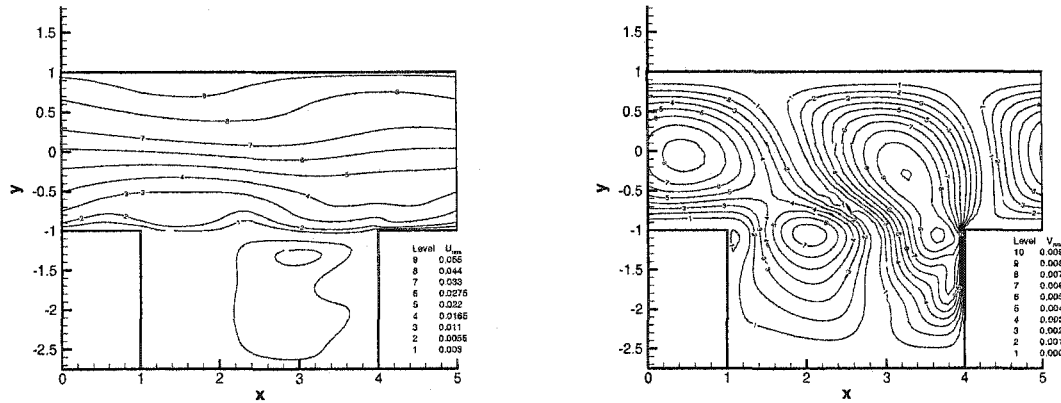


Figure 6.21: Standard deviation of velocity fields at $t = 5,000$. $r = 220$ and $Re = 238.6$. Left: u -velocity, Right: v -velocity.

from the Orr-Sommerfeld equation for a straight channel, (see, for example, [25])

$$\frac{1}{Re}(D^2 - \alpha^2)^2 \phi - 2i\alpha \phi = \lambda(D^2 - \alpha^2)\phi, \quad D^2 = \frac{d^2}{dy^2}, \quad (6.22)$$

with boundary conditions $\alpha \phi = D\phi = 0$ at $y = \pm 1$. Here the base steady flow is $\mathbf{U} = (1 - y^2, 0)$ and the perturbation takes the form

$$\mathbf{u}'(\mathbf{x}, t) = \hat{\mathbf{v}}(y) \exp(i\alpha x + \lambda t), \quad (6.23)$$

where $\lambda = \sigma + i2\pi f$ is complex. Equation 6.22 defines an eigenvalue problem, from which the least stable mode can be solved in the following form

$$\mathcal{F}(\sigma_{TS}, f_{TS}; \alpha, Re) = 0. \quad (6.24)$$

Such problem was first solved accurately in [97] by a spectral method, and several different approaches were proposed afterwards. (cf. [15, 55], etc.) Here we adopt the pseudospectral method based on Chebyshev polynomials developed in [55], where two distinct interpolation polynomials are employed for the second and fourth derivatives to effectively eliminate the spurious eigenvalues produced by a direct spectral tau method [34, 86]. In table 6.2, the results of the current computation via $N = 100$ Chebyshev points

Re	α	λ/α (present)	λ/α ([97])
10,000	1	$0.00373967 - 0.23752649i$	$0.00373967 - 0.23752649i$
5772.22	1.02056	$-6.9(-10) - 0.26400174i$	$-5.9(-10) - 0.26400174i$
5772.23	1.02056	$-1.6(-8) - 0.26400166i$	$-1.9(-8) - 0.26400166i$

Table 6.2: Comparison of the least stable mode ($\lambda = \sigma + i2\pi f$) of the Orr-Sommerfeld equation for plain Poiseuille flow.

are presented, along with results from [97]. It can be seen that the present computation agrees with that of [97] up to 10^{-8} , which is the accuracy limit of [97] due to its single-precision arithmetic.

Following similar approach in [36], we observe that the velocity perturbation from figure 6.21 has $n = 1$ wave. Thus the wave number is $\alpha = 2\pi n/L = 1.25664$ (the channel length is $L = 5$). The corresponding TS wave frequency is calculated to be $f_{\text{TS}} = 0.094$. The frequency from figure 6.19 is $f = 0.1075$ and is reasonably close to f_{TS} . Hence we conclude that the observed instability is again the least stable Tollmein-Schlichting wave mode destabilized by the random boundary condition and the free-shear-layer. Since the deterministic flow at this Reynolds number is steady, the dominant destabilization factor is the random boundary condition.

This preliminary study demonstrates the effect of uncertainty in boundary conditions on flow instability. Future research is to study the effect of more realistic noisy slip conditions, i.e. random processes incorporated in various slip models for microflow [61], and their effects on the first critical Reynolds number as well as the second critical Reynolds number where the three-dimensional modes are excited.

Chapter 7

Summary

The concept of generalized polynomial chaos is developed in this thesis. This is a framework, which extends the original Wiener-Hermite polynomial chaos, for the purpose of uncertainty quantification in practical applications. Here, we studied the mathematical properties of generalized polynomial chaos, and further applied it to various differential equations subject to random inputs. In particular, the systems we have studied include:

- Ordinary differential equation, where the spectral converge of generalized polynomial chaos is presented. The effect of using non-optimal bases is also studied.
- Elliptic equation, i.e., steady state diffusion equation with random diffusivity, source terms, and/or boundary conditions. A random mapping technique is also proposed to solve problems with uncertain domain (roughness).
- Parabolic equation. Here the well-posedness of the semi-discrete equations from the chaos expansion is studied via a simple unsteady diffusion equation with random diffusivity. On the application side, the unsteady heat conduction in an electronic chip is simulated with uncertain heat capacity and heat conductivity.
- Advection-diffusion. This includes both a linear advection-diffusion equation subject to random transport velocity, and nonlinear advection-diffusion, i.e. Burgers' equation with random perturbation on the boundary condition. In particular, the stochastic supersensitivity is simulated via high-order expansion, both in physical

space and random space.

- **Incompressible flow.** A microchannel flow with random boundary conditions is considered, where Monte Carlo simulations are employed to validate the results from generalized polynomial chaos, and good agreements are obtained. Two flows, flow past a circular cylinder (external flow) and flow in a periodically grooved channel (internal flow), are then studied, where the effect of uncertainty in boundary conditions on the flow instability is examined. It is found that the random inputs can triggered flow instability at lower Reynolds numbers.

In all the applications, extensive validations are conducted, where the results from generalized polynomial chaos are compared to exact solutions if known, or results from Monte Carlo simulations. It is shown that the results from chaos expansion are accurate and converge fast. The generalized polynomial chaos, with appropriately chosen bases, achieves exponential convergence for model problems. Compared to Monte Carlo simulations, the computational cost of generalized polynomial chaos is significantly lower, in many cases, by two to three orders.

Although the generalized polynomial chaos is shown to be highly efficient compared to sampling methods, it is still a new concept and there exist several open issues. Among them, we list the following prominent ones:

- *Mathematical framework.* More rigorous mathematical analysis is needed to clearly define the functional space determined by each set of polynomial bases. Correspondingly, various mathematical properties can be studied. This will help us further understand the applicability of generalized polynomial chaos. For example, many theoretical results in Gaussian Hilbert space rely heavily on the rotational invariance of Gaussian measure. For the non-Gaussian measures utilized by the generalized polynomial chaos, such invariance does not exist and its effect needs to be studied.
- *Convergence.* Although exponential convergence has been demonstrated in various model problems, the rigorous analysis on the convergence rate is still lacking. Also, the poor convergence of polynomial chaos for some problems, e.g., see examples in [98], needs to be explained.

- *High-dimensional expansion.* Similar to many numerical techniques, the generalized polynomial chaos suffers from the ‘curse of dimensionality’. The number of expansion terms grows rapidly when the dimensionality increases, so does the computational cost. Thus, the efficiency of generalized polynomial chaos decreases drastically for high-dimensional expansions.

In conclusion, generalized polynomial chaos has been shown to be a very promising tool for uncertainty quantification in real systems, as many of the examples in this thesis have demonstrated. It remains a relatively new concept, and much more research efforts are needed to further exploit its advantage.

Appendix A

Some Important Orthogonal Polynomials in Askey-scheme

Here we summarize the definitions and properties of some important orthogonal polynomials from Askey scheme. Denote $\{Q_n(x)\}$ as orthogonal polynomial system with the orthogonal relation

$$\int_S Q_n(x)Q_m(x)w(x)dx = h_n^2\delta_{mn},$$

for continuous x , or in the discrete case

$$\sum_x Q_n(x)Q_m(x)w(x) = h_n^2\delta_{mn},$$

where S is the support of $w(x)$. The three-term recurrence relation takes the form

$$-xQ_n(x) = b_nQ_{n+1}(x) + \gamma_nQ_n(x) + c_nQ_{n-1}(x), \quad n \geq 0,$$

with initial conditions $Q_{-1}(x) = 0$ and $Q_0(x) = 1$. Another way of expressing the recurrence relation is

$$Q_{n+1}(x) = (A_nx + B_n)Q_n(x) - C_nQ_{n-1}(x), \quad n \geq 0, \quad (\text{A.1})$$

where $A_n, C_n \neq 0$ and $C_n A_n A_{n-1} > 0$. It is straightforward to show that, if we scale variable x by denoting $y = \alpha x$ for $\alpha > 0$, then the recurrence relation takes the form

$$S_{n+1}(y) = (A_n y + \alpha B_n) S_n(y) - \alpha^2 C_n S_{n-1}(y). \quad (\text{A.2})$$

A.1 Continuous Polynomials

A.1.1 Hermite Polynomial $H_n(x)$ and Gaussian Distribution

Definition:

$$H_n(x) = (2x)^n {}_2F_0 \left(-\frac{n}{2}, -\frac{n-1}{2}; ; -\frac{2}{x^2} \right). \quad (\text{A.3})$$

Orthogonality:

$$\int_{-\infty}^{\infty} H_m(x) H_n(x) w(x) dx = n! \delta_{mn}, \quad (\text{A.4})$$

where

$$w(x) = \frac{1}{\sqrt{2\pi}} e^{-x^2/2}. \quad (\text{A.5})$$

Recurrence relation:

$$H_{n+1}(x) = x H_n(x) - n H_{n-1}(x). \quad (\text{A.6})$$

Rodriguez formula:

$$e^{-x^2/2} H_n(x) = (-1)^n \frac{d^n}{dx^n} \left(e^{-x^2/2} \right). \quad (\text{A.7})$$

A.1.2 Laguerre Polynomial $L_n^{(\alpha)}(x)$ and Gamma Distribution

Definition:

$$L_n^{(\alpha)}(x) = \frac{(\alpha+1)_n}{n!} {}_1F_1(-n; \alpha+1; x). \quad (\text{A.8})$$

Orthogonality:

$$\int_0^{\infty} L_m^{(\alpha)}(x) L_n^{(\alpha)}(x) w(x) dx = \frac{(\alpha+1)_n}{n!} \delta_{mn}, \quad \alpha > -1, \quad (\text{A.9})$$

where

$$w(x) = \frac{x^\alpha e^{-x}}{\Gamma(\alpha+1)}. \quad (\text{A.10})$$

Recurrence relation:

$$(n+1)L_{n+1}^{(\alpha)}(x) - (2n + \alpha + 1 - x)L_n^{(\alpha)}(x) + (n + \alpha)L_{n-1}^{(\alpha)}(x) = 0. \quad (\text{A.11})$$

Normalized recurrence relation:

$$xq_n(x) = q_{n+1}(x) + (2n + \alpha + 1)q_n(x) + n(n + \alpha)q_{n-1}(x), \quad (\text{A.12})$$

where

$$L_n^{(\alpha)}(x) = \frac{(-1)^n}{n!} q_n(x).$$

Rodriguez formula:

$$e^{-x} x^\alpha L_n^{(\alpha)}(x) = \frac{1}{n!} \frac{d^n}{dx^n} (e^{-x} x^{n+\alpha}). \quad (\text{A.13})$$

Recall that the *gamma* distribution has the probability density function

$$f(x) = \frac{x^\alpha e^{-x/\beta}}{\beta^{\alpha+1} \Gamma(\alpha+1)}, \quad \alpha > -1, \beta > 0. \quad (\text{A.14})$$

The weighting function of Laguerre polynomial (A.10) is the same of gamma distribution with the scale parameter $\beta = 1$.

A.1.3 Jacobi Polynomial $P_n^{(\alpha,\beta)}(x)$ and Beta Distribution

Definition:

$$P_n^{(\alpha,\beta)}(x) = \frac{(\alpha+1)_n}{n!} {}_2F_1 \left(-n, n + \alpha + \beta + 1; \alpha + 1; \frac{1-x}{2} \right). \quad (\text{A.15})$$

Orthogonality:

$$\int_{-1}^1 P_m^{(\alpha,\beta)}(x) P_n^{(\alpha,\beta)}(x) w(x) dx = h_n^2 \delta_{mn}, \quad \alpha, \beta > -1, \quad (\text{A.16})$$

where

$$\begin{aligned} h_n^2 &= \frac{(\alpha+1)_n(\beta+1)_n}{n!(2n+\alpha+\beta+1)(\alpha+\beta+2)_{n-1}}, \\ w(x) &= \frac{\Gamma(\alpha+\beta+2)}{2^{\alpha+\beta+1}\Gamma(\alpha+1)\Gamma(\beta+1)}(1-x)^\alpha(1+x)^\beta. \end{aligned} \quad (\text{A.17})$$

Recurrence relation:

$$\begin{aligned} xP_n^{(\alpha,\beta)}(x) &= \frac{2(n+1)(n+\alpha+\beta+1)}{(2n+\alpha+\beta+1)(2n+\alpha+\beta+2)}P_{n+1}^{(\alpha,\beta)}(x) \\ &+ \frac{\beta^2-\alpha^2}{(2n+\alpha+\beta)(2n+\alpha+\beta+2)}P_n^{(\alpha,\beta)}(x) \\ &+ \frac{2(n+\alpha)(n+\beta)}{(2n+\alpha+\beta)(2n+\alpha+\beta+1)}P_{n-1}^{(\alpha,\beta)}(x). \end{aligned} \quad (\text{A.18})$$

Normalized recurrence relation:

$$\begin{aligned} xp_n(x) &= p_{n+1}(x) + \frac{\beta^2-\alpha^2}{(2n+\alpha+\beta)(2n+\alpha+\beta+2)}p_n(x) \\ &+ \frac{4n(n+\alpha)(n+\beta)(n+\alpha+\beta)}{(2n+\alpha+\beta-1)(2n+\alpha+\beta)^2(2n+\alpha+\beta+1)}p_{n-1}(x), \end{aligned} \quad (\text{A.19})$$

where

$$P_n^{(\alpha,\beta)}(x) = \frac{(n+\alpha+\beta+1)_n}{2^n n!} p_n(x).$$

Rodriguez formula:

$$(1-x)^\alpha(1+x)^\beta P_n^{(\alpha,\beta)}(x) = \frac{(-1)^n}{2^n n!} \frac{d^n}{dx^n} \left[(1-x)^{n+\alpha}(1+x)^{n+\beta} \right]. \quad (\text{A.20})$$

A.2 Discrete Polynomials

A.2.1 Charlier Polynomial $C_n(x; a)$ and Poisson Distribution

Definition:

$$C_n(x; a) = {}_2F_0 \left(-n, -x; ; -\frac{1}{a} \right). \quad (\text{A.21})$$

Orthogonality:

$$\sum_{x=0}^{\infty} \frac{a^x}{x!} C_m(x; a) C_n(x; a) = a^{-n} e^a n! \delta_{mn}, \quad a > 0. \quad (\text{A.22})$$

Recurrence relation:

$$-x C_n(x; a) = a C_{n+1}(x; a) - (n + a) C_n(x; a) + n C_{n-1}(x; a). \quad (\text{A.23})$$

Rodriguez formula:

$$\frac{a^x}{x!} C_n(x; a) = \nabla^n \left(\frac{a^x}{x!} \right), \quad (\text{A.24})$$

where ∇ is the backward difference operator defined as $\nabla f(x) = f(x) - f(x - 1)$.

The probability function of *Poisson* distribution is

$$f(x; a) = e^{-a} \frac{a^x}{x!}, \quad k = 0, 1, 2, \dots \quad (\text{A.25})$$

Despite of a constant factor e^{-a} , it is the same as the weighting function of Charlier polynomials.

A.2.2 Krawtchouk Polynomial $K_n(x; p, N)$ and Binomial Distribution

Definition:

$$K_n(x; p, N) = {}_2F_1 \left(-n, -x; -N; \frac{1}{p} \right), \quad n = 0, 1, \dots, N. \quad (\text{A.26})$$

Orthogonality:

$$\sum_{x=0}^N \binom{N}{x} p^x (1-p)^{N-x} K_m(x; p, N) K_n(x; p, N) = \frac{(-1)^n n!}{(-N)_n} \left(\frac{1-p}{p} \right)^n \delta_{mn}, \quad 0 < p < 1. \quad (\text{A.27})$$

Recurrence relation:

$$\begin{aligned} -x K(x; p, N) &= p(N-n) K_{n+1}(x; p, N) - [p(N-n) + n(1-p)] K_n(x; p, N) \\ &+ n(1-p) K_{n-1}(x; p, N). \end{aligned} \quad (\text{A.28})$$

Rodriguez formula:

$$\binom{N}{x} \left(\frac{p}{1-p}\right)^x K_n(x; p, N) = \nabla^n \left[\binom{N-n}{x} \left(\frac{p}{1-p}\right)^x \right]. \quad (\text{A.29})$$

Clearly, the weighting function from (A.27) is the probability function of the *binomial* distribution.

A.2.3 Meixner Polynomial $M_n(x; \beta, c)$ and Negative Binomial Distribution

Definition:

$$M_n(x; \beta, c) = {}_2F_1 \left(-n, -x; \beta; 1 - \frac{1}{c} \right). \quad (\text{A.30})$$

Orthogonality:

$$\sum_{x=0}^{\infty} \frac{(\beta)_x}{x!} c^x M_m(x; \beta, c) M_n(x; \beta, c) = \frac{c^{-n} n!}{(\beta)_n (1-c)^\beta} \delta_{mn}, \quad \beta > 0, \quad 0 < c < 1. \quad (\text{A.31})$$

Recurrence relation:

$$\begin{aligned} (c-1)xM_n(x; \beta, c) &= c(n+\beta)M_{n+1}(x; \beta, c) - [n+(n+\beta)c]M_n(x; \beta, c) \\ &+ nM_{n-1}(x; \beta, c). \end{aligned} \quad (\text{A.32})$$

Rodriguez formula:

$$\frac{(\beta)_x c^x}{x!} M_n(x; \beta, c) = \nabla^n \left[\frac{(\beta+n)_x c^x}{x!} \right]. \quad (\text{A.33})$$

The weighting function is

$$f(x) = \frac{(\beta)_x}{x!} (1-c)^\beta c^x, \quad 0 < c < 1, \quad \beta > 0, \quad x = 0, 1, 2, \dots \quad (\text{A.34})$$

It can be verified that it is the probability function of *negative binomial* distribution. In the case of β being integer, it is often called the *Pascal* distribution.

A.2.4 Hahn Polynomial $Q_n(x; \alpha, \beta, N)$ and Hypergeometric Distribution

Definition:

$$Q_n(x; \alpha, \beta, N) = {}_3F_2(-n, n + \alpha + \beta + 1, -x; \alpha + 1, -N; 1), \quad n = 0, 1, \dots, N. \quad (\text{A.35})$$

Orthogonality: For $\alpha > -1$ and $\beta > -1$ or for $\alpha < -N$ and $\beta < -N$,

$$\sum_{x=0}^N \binom{\alpha+x}{x} \binom{\beta+N-x}{N-x} Q_m(x; \alpha, \beta, N) Q_n(x; \alpha, \beta, N) = h_n^2 \delta_{mn}, \quad (\text{A.36})$$

where

$$h_n^2 = \frac{(-1)^n (n + \alpha + \beta + 1)_{N+1} (\beta + 1)_n n!}{(2n + \alpha + \beta + 1) (\alpha + 1)_n (-N)_n N!}.$$

Recurrence relation:

$$-xQ_n(x) = A_n Q_{n+1}(x) - (A_n + C_n) Q_n(x) + C_n Q_{n-1}(x), \quad (\text{A.37})$$

where

$$Q_n(x) := Q_n(x; \alpha, \beta, N)$$

and

$$\begin{cases} A_n = \frac{(n+\alpha+\beta+1)(n+\alpha+1)(N-n)}{(2n+\alpha+\beta+1)(2n+\alpha+\beta+2)} \\ C_n = \frac{n(n+\alpha+\beta+N+1)(n+\beta)}{(2n+\alpha+\beta)(2n+\alpha+\beta+1)}. \end{cases}$$

Rodriguez formula:

$$w(x; \alpha, \beta, N) Q_n(x; \alpha, \beta, N) = \frac{(-1)^n (\beta + 1)_n}{(-N)_n} \nabla^n [w(x; \alpha + n, \beta + n, N - n)], \quad (\text{A.38})$$

where

$$w(x; \alpha, \beta, N) = \binom{\alpha+x}{x} \binom{\beta+N-x}{N-x}.$$

If we set $\alpha = -\tilde{\alpha} - 1$ and $\beta = -\tilde{\beta} - 1$, we obtain

$$\tilde{w}(x) = \frac{1}{\binom{N-\tilde{\alpha}-\tilde{\beta}-1}{N}} \frac{\binom{\tilde{\alpha}}{x} \binom{\tilde{\beta}}{N-x}}{\binom{\tilde{\alpha}+\tilde{\beta}}{N}}.$$

Apart from the constant factor $1/\binom{N-\tilde{\alpha}-\tilde{\beta}-1}{N}$, this is the definition of *hypergeometric* distribution.

Appendix B

Estimation of the Largest Zero of Hermite Polynomials

Since our definition of Hermite polynomials is different from the traditional definition, the corresponding estimates of the largest zero are slightly different. They are presented here for the completeness of the paper.

The classical Hermite polynomials $h_n(x)$ are defined as

$$h_n(x) = (2x)^n {}_2F_0\left(-\frac{n}{2}, -\frac{n-1}{2}; ; -\frac{1}{x^2}\right), \quad (\text{B.1})$$

and satisfy the three-term recurrence relation

$$h_{n+1}(x) - 2xh_n(x) + 2nh_{n-1}(x) = 0. \quad (\text{B.2})$$

From the classical analysis on $h_n(x)$, there are two estimates on the largest zeros x_0 of Hermite polynomials $h_n(x)$: lower bound $x_0 > \sqrt{(n-1)/2}$; lower bound $x_0 \leq \sqrt{2}(n-1)/\sqrt{n-2}$ (see [117]).

The relation between the Hermite polynomials used in this paper $\{H_n(x)\}$ (A.3) and the traditional ones $\{h_n(x)\}$ is

$$h_n(x) = 2^{n/2} H_n(\sqrt{2}x).$$

Hence, the largest zero of Hermite polynomials $H_n(x)$ are

$$\text{lower bound: } x_0 > \sqrt{n-1}; \quad (\text{B.3})$$

$$\text{upper bound: } x_0 \leq \frac{2(n-1)}{\sqrt{n-2}}. \quad (\text{B.4})$$

Appendix C

The Truncated Gaussian Model

$G(\alpha, \beta)$

The truncated Gaussian model was developed in [133] in order to circumvent the mathematical difficulty resulted from the tails of Gaussian distribution. It is an approximation of Gaussian distributions by Jacobi-chaos expansion. The approximation can be improved either by increasing the order of expansion, or by adjusting the parameters in the Jacobi-chaos definition. The important property of the model is that it has bounded support, i.e. no tails. This can be used as an alternative in practical applications, where the random inputs resemble Gaussian distributions *and* the boundedness of the supports is critical to the solution procedure. Here we briefly review its construction from [133].

Suppose $y(\omega) \sim N(0, 1)$ is a Gaussian random variable, and we use the Jacobi-chaos $\{\Phi(\xi)\}$ to represent it. Here $\xi \sim Be^{(\alpha, \beta)}(-1, 1)$ is a beta random variable defined in $(-1, 1)$ with parameters $\alpha, \beta > -1$ and probability density function (A.17).

$$\hat{y}(\omega) = \sum_{k=0}^M y_k \Phi_k(\xi), \quad y_k = \frac{\langle y(\omega), \Phi_k(\xi) \rangle}{\langle \Phi_k^2(\xi) \rangle}. \quad (\text{C.1})$$

Evaluation of the expansion coefficients is carried out in the way described in section 2.3.2. The resulting $\hat{y}(\omega)$ is an approximation to the target Gaussian $y(\omega)$, and will be denoted as $G(\alpha, \beta)$ with $\alpha, \beta > -1$. Due to the symmetry of Gaussian distribution, we set $\alpha = \beta$ in the Jacobi-chaos.

In Figures C.1 to C.3, the PDFs of the Jacobi-chaos approximations are plotted, for values of $\alpha = \beta = 0$ to 10. For $\alpha = \beta = 0$, Jacobi-chaos becomes Legendre-chaos, and the first-order expansion is simply a uniform random variable. In this case, Gibb's oscillations are observed. As the values of (α, β) increase, the approximations improve. The expansion coefficients at different orders are tabulated in Table C.1, together with the errors in variance and kurtosis compared with the 'exact' Gaussian distribution. It is seen that with $\alpha = \beta = 10$, even the first-order approximation, which is simply a beta random variable, has error in variance as little as 0.1%. The errors in kurtosis are larger because the Jacobi-chaos approximations do not possess tails. This, however, is exactly our objective.

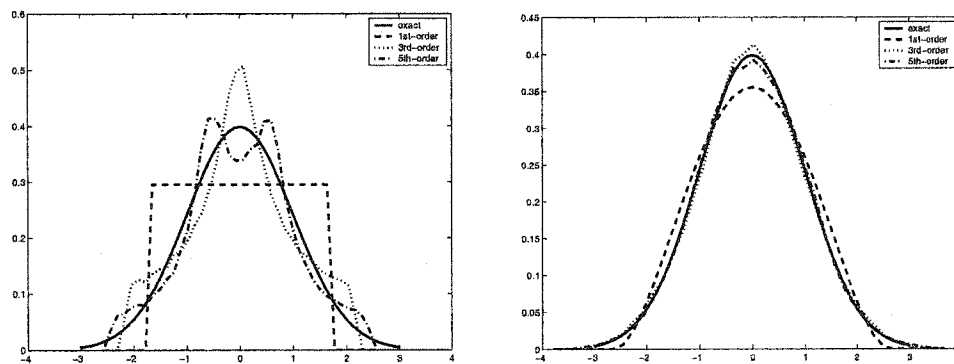


Figure C.1: Approximated Gaussian random variables by Jacobi-chaos; Left: $\alpha = \beta = 0$, Right: $\alpha = \beta = 2$.

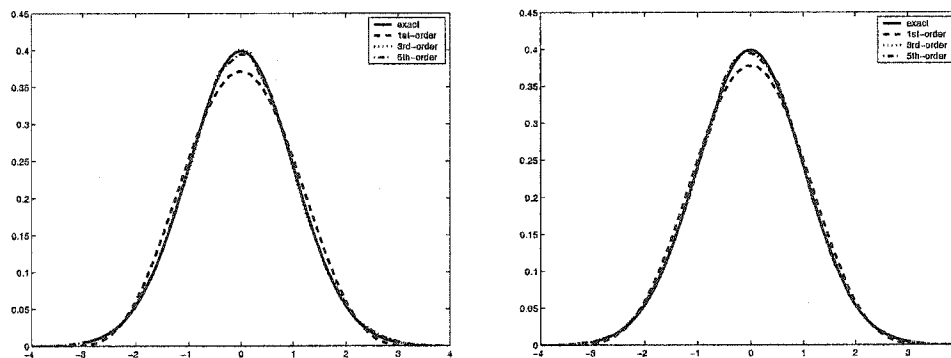


Figure C.2: Approximated Gaussian random variables by Jacobi-chaos; Left: $\alpha = \beta = 4$, Right: $\alpha = \beta = 6$.

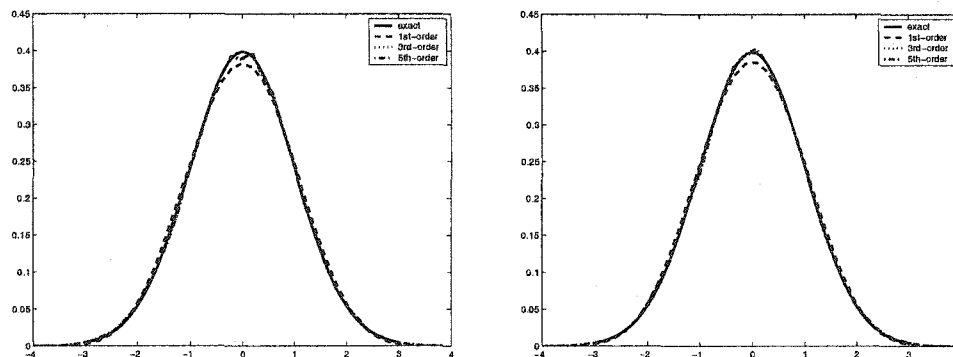


Figure C.3: Approximated Gaussian random variables by Jacobi-chaos; Left: $\alpha = \beta = 8$, Right: $\alpha = \beta = 10$.

Table C.1: Approximating Gaussian via Jacobi-chaos: expansion coefficients y_k and errors. (ϵ_2 is the error in variance; ϵ_4 is the error in kurtosis. There is no error in mean.) $y_k = 0$ when k is even.

	$\alpha = \beta = 0$	$\alpha = \beta = 2$	$\alpha = \beta = 4$	$\alpha = \beta = 6$	$\alpha = \beta = 8$	$\alpha = \beta = 10$
y_1	1.69248	8.7827(-1)	6.6218(-1)	5.5273(-1)	4.8399(-1)	4.3575(-1)
ϵ_2	4.51704(-2)	8.25346(-3)	3.46301(-3)	2.00729(-3)	1.38842(-3)	1.07231(-3)
ϵ_4	1.35894	7.05024(-1)	4.79089(-1)	3.63557(-1)	2.93246(-1)	2.45916(-1)
y_3	4.8399(-1)	7.5493(-2)	2.6011(-2)	1.2216(-2)	6.77970(-3)	4.17792(-3)
ϵ_2	1.17071(-2)	8.51816(-4)	4.49245(-4)	4.23983(-4)	4.33894(-4)	4.45282(-4)
ϵ_4	5.02097(-1)	7.97474(-2)	3.33201(-2)	2.40064(-2)	2.21484(-2)	2.22539(-2)
y_5	2.7064(-1)	1.9959(-2)	2.9936(-3)	2.3531(-4)	-3.30888(-4)	-4.19539(-4)
ϵ_2	5.04838(-3)	3.97059(-4)	3.96880(-4)	4.22903(-4)	4.28283(-4)	4.25043(-4)
ϵ_4	2.55526(-1)	2.29373(-2)	1.92101(-2)	2.15095(-2)	2.06846(-2)	2.08317(-2)

Appendix D

Numerical Results for Supersensitivity of Burgers' Equation

D.1 Numerical Results for Deterministic Supersensitivity

Here we summarize the deterministic results of the direct numerical simulations of problem (5.9). In Table D.1 and D.2 we tabulate the solutions at $\nu = 0.05$ and $\nu = 0.1$, respectively. Different values of δ are considered, and the orders of spectral elements are increased in order to obtain resolution independent solutions. It can be seen that with 20th-order spectral elements ($N = 20$), the locations of transition layer converge with eight significant digits, and they agree with exact solutions to seven digits.

D.2 Numerical Results for Stochastic Supersensitivity

In Table D.3, the numerical results of Burgers' equation (5.9) are shown for $\nu = 0.05$ and $\delta \sim U(0, 0.1)$. The mean locations of the transition layer and their standard deviations are tabulated, with different Legendre-chaos orders M and spectral element orders N . It can be seen that as the expansion orders, both N in physical space and M in random space, increase, the results converge to resolution-independent values. In this case, they

Table D.1: The locations of the transition layer at $\nu = 0.05$ with different values of perturbation δ . N is the order of spectral elements, and the dash “—” indicates the number there is the same as the one above it. Also shown are the results from exact formula.

	$\delta = 10^{-1}$	$\delta = 10^{-2}$	$\delta = 10^{-3}$	$\delta = 10^{-4}$	$\delta = 10^{-5}$
T_{\max}	60	400	3,480	13,500	88,000
$N = 10$	0.86162068	0.73745817	0.62032373	0.50485891	0.38969812
$N = 12$	0.86161448	0.73746021	0.62031203	0.50487016	0.39970204
$N = 14$	0.86161302	0.73746023	0.62030992	0.50487220	0.38970225
$N = 16$	0.86161270	0.73746017	0.62030961	0.50487256	0.38970223
$N = 18$	0.86161263	0.73746015	0.62030958	0.50487262	—
$N = 20$	0.86161262	—	0.62030957	0.50487263	—
$N = 21$	—	—	—	—	—
Exact	0.86161262	0.73746015	0.62030957	0.50487264	0.38970229

Table D.2: The locations of the transition layer at $\nu = 0.1$ with different values of perturbation δ . N is the order of spectral elements, and the dash “—” indicates the number there is the same as the one above it. Also shown are the results from exact formula.

	$\delta = 10^{-1}$	$\delta = 10^{-2}$	$\delta = 10^{-3}$	$\delta = 10^{-4}$	$\delta = 10^{-5}$
$N = 10$	0.72322540	0.47992739	0.24142359	0.052673383	0.0055171392
$N = 12$	0.72322524	0.47492741	0.24142361	0.052669622	0.0055085668
$N = 14$	0.72322525	0.47492741	—	0.052669616	0.0055085545
$N = 16$	—	—	—	—	—
Exact	0.72322525	0.47492741	0.24142361	0.052669612	0.0055085559

are $\bar{z} = 0.81390488$ and $\sigma_z = 0.41403291$, which are the same as the reference values obtained with a higher resolution of $M = 10$ and $N = 22$.

Table D.3: The stochastic solution of the locations of the transition layer at $\nu = 0.05$ listed in form of (\bar{z}, σ_z) , where \bar{z} is the mean location and σ_z its standard deviation. M is the order of Legendre-chaos; N is the order of spectral elements. The dash “—” indicates the number there is the same as the one above it. The reference values obtained by $M = 10$ and $N = 22$ are $(0.81390488, 0.41403291)$.

	$N = 14$	$N = 18$	$N = 20$
$M = 1$	0.81459325, 0.37660585	0.81459294, 0.37660750	0.81459294, 0.37660751
$M = 2$	0.81394065, 0.41100263	0.81394090, 0.41099364	0.81394090, 0.41099350
$M = 3$	0.81390669, 0.41382150	0.81390671, 0.41382035	0.81390671, 0.41382035
$M = 4$	0.81390493, 0.41401936	0.81390498, 0.41401904	0.81390498, 0.41401897
$M = 5$	0.81390481, 0.41403293	0.81390489, 0.41403210	0.81390489, 0.41403202
$M = 6$	—, 0.41403393	0.81390488, 0.41403291	0.81390488, 0.41403286
$M = 7$	—, —	—, 0.41403296	—, 0.41403291
$M = 8$	—, —	—, —	—, —

Similar resolution-independence tests were conducted for all the cases reported in this paper, and they are not further tabulated here.

Bibliography

- [1] Decision making under uncertainty. In C. Greengard and A. Ruszczynski, editors, *Series: The IMA Volumes in Mathematics and its Applications*, volume 128. Springer-Verlag, 2002.
- [2] M. Anders and M. Hori. Three-dimensional stochastic finite element method for elasto-plastic bodies. *Int. J. Numer. Meth. Engng.*, 51:449–478, 2001.
- [3] R. Askey and J. Wilson. Some basic hypergeometric polynomials that generalize Jacobi polynomials. *Memoirs Amer. Math. Soc., AMS, Providence RI*, 319, 1985.
- [4] I. Babuška. On randomized solutions of Laplace's equation. *Casopis Pest. Mat.*, 36:269–276, 1961.
- [5] I. Babuška and P. Chatzipantelidis. On solving elliptic stochastic partial differential equations. *Comput. Methods Appl. Mech. Engrg.*, 191:4093–4122, 2002.
- [6] I. Babuška, R. Tempone, and G.E. Zouraris. Galerkin finite element approximations of stochastic elliptic differential equations. Technical Report 02-38, TICAM, 2002.
- [7] G.A. Bécus and F.A. Cozzarelli. The random steady state diffusion problem. I. random generalized solutions to Laplace's equation. *SIAM J. Appl. Math.*, 31:134–147, 1976.
- [8] G.A. Bécus and F.A. Cozzarelli. The random steady state diffusion problem. II: random solutions to nonlinear inhomogeneous, steady state diffusion problems. *SIAM J. Appl. Math.*, 31:148–158, 1976.

- [9] G.A. Bécus and F.A. Cozzarelli. The random steady state diffusion problem. III: solutions to random diffusion problems by the method of random successive approximations. *SIAM J. Appl. Math.*, 31:159–178, 1976.
- [10] P. Beckmann. *Orthogonal Polynomials for Engineers and Physicists*. Golem Press, Boulder, Colorado, 1973.
- [11] K. Binder and D.W. Heermann. *Monte Carlo simulation in statistical physics : an introduction*. Springer-Verlag, 1998.
- [12] G.E.P. Box and N.R. Draper. *Empirical model-building and response surfaces*. John Wiley & Sons, New York, 1987.
- [13] C.G. Bucher and U. Bourgund. A fast and efficient response surfact approach for structural reliability problems. *Struc. Safety*, 7:57–66, 1990.
- [14] R.H. Cameron and W.T. Martin. The orthogonal development of nonlinear functionals in series of Fourier-Hermite functionals. *Ann. Math.*, 48:385–392, 1947.
- [15] C. Canuto, M.Y. Hussaini, A. Quarteroni, and T.A. Zang. *Spectral methods in fluid dynamics*. Springer-Verlag, Berlin/Heidelberg, 1988.
- [16] T.S. Chihara. *An Introduction to Orthogonal Polynomials*. Gordon and Breach, Science Publishers, Inc., 1978.
- [17] A.J. Chorin. Hermite expansion in Monte-Carlo simulations. *J. Comput. Phys.*, 8:472–482, 1971.
- [18] J.H. Cushman. *The physics of fluids in hierarchical porous media: angstroms to miles*. Kluwer Academic, Norwell, MA, 1997.
- [19] G. Dagan. *Flow and transport in porous formations*. Springer-Verlag, New York, 1989.
- [20] A.E. Deane, I.G. Kevrekidis, G.E. Karniadakis, and S. A. Orszag. Low-dimensional models for complex geometry flows: Application to grooved channels and circular cylinders. *Phys. Fluids*, 3(10):2337, 1991.

- [21] M.K. Deb, I. Babuška, and J.T. Oden. Solution of stochastic partial differential equations using Galerkin finite element techniques. *Comput. Methods Appl. Mech. Engrg.*, 190:6359–6372, 2001.
- [22] G. Deodatis. Weighted integral method. I: stochastic stiffness matrix. *J. Eng. Mech.*, 117(8):1851–1864, 1991.
- [23] G. Deodatis and M. Shinozuka. Weighted integral method. II: response variability and reliability. *J. Eng. Mech.*, 117(8):1865–1877, 1991.
- [24] J.D. Doll and D.L. Freeman. Randomly exact methods. *Science*, 234:1356–1360, 1986.
- [25] P.G. Drazin and W.H. Reid. *Hydrodynamic stability*. Cambridge University Press, 1981.
- [26] A. Dubi. *Monte Carlo applications in systems engineering*. John Wiley & Sons, 2000.
- [27] D.D. Engel. The multiple stochastic integral. *Memoirs Amer. Math. Soc.*, AMS, Providence, RI, 265, 1982.
- [28] T.D. Fadale and A.F. Emery. Transient effects of uncertainties on the sensitivities of temperatures and heat fluxes using stochastic finite elements. *J. Heat Trans.*, 116:808–814, 1994.
- [29] L. Faravelli. Response surface approach for reliability analysis. *J. Eng. Mech.*, 115:2763–2781, 1989.
- [30] G.S. Fishman. *Monte Carlo: Concepts, Algorithms, and Applications*. Springer-Verlag New York, Inc., 1996.
- [31] B.L. Fox. *Strategies for Quasi-Monte Carlo*. Kluwer Academic Pub., 1999.
- [32] D. Gamerman. *Markov Chain Monte Carlo : stochastic simulation for Bayesian inference*. Chapman & Hall, 1997.
- [33] M. Garbey and H.A. Kaper. Asymptotic-numerical study of supersensitivity for generalized Burgers' equations. *SIAM J. Sci. Comput.*, 22:368–385, 2000.

- [34] D.R. Gardner, S.A. Trogdon, and R.W. Douglass. A modified tau spectral method that eliminates spurious eigenvalues. *J. Comput. Phys.*, 80:137–167, 1989.
- [35] J.E. Gentle. *Random number generation and Monte Carlo methods (statistics and computing)*. Springer-Verlag, 1998.
- [36] N. Ghaddar, K. Korczak, B. Mikic, and A. Patera. Numerical investigation of incompressible flow in grooved channels. *J. Fluid Mech.*, 163:99–128, 1986.
- [37] R. Ghanem and B. Hayek. Probabilistic modeling of flow over rough terrain. *J. Fluids Eng.*, 124(1):42–50, 2002.
- [38] R.G. Ghanem. Scales of fluctuation and the propagation of uncertainty in random porous media. *Water Resources Research*, 34:2123, 1998.
- [39] R.G. Ghanem. Ingredients for a general purpose stochastic finite element formulation. *Comput. Methods Appl. Mech. Engrg.*, 168:19–34, 1999.
- [40] R.G. Ghanem. Stochastic finite elements for heterogeneous media with multiple random non-Gaussian properties. *ASCE J. Eng. Mech.*, 125(1):26–40, 1999.
- [41] R.G. Ghanem and W. Brzakala. Stochastic finite-element analysis of soil layers with random interface. *ASCE J. Eng. Mech.*, 122:361–369, 1996.
- [42] R.G. Ghanem and J. Red-Horse. Propagation of uncertainty in complex physical systems using a stochastic finite elements approach. *Physica D*, 133:137–144, 1999.
- [43] R.G. Ghanem and P.D. Spanos. *Stochastic Finite Elements: a Spectral Approach*. Springer-Verlag, 1991.
- [44] W.R. Gilks, S. Richardson, and D.J. Spiegelhalter. *Markov Chain Monte Carlo in practice*. Chapman & Hall, 1995.
- [45] J. Glimm. Nonlinear and stochastic phenomena: the grand challenge for partial differential equations. *SIAM Rev.*, 33:626–643, 1991.
- [46] J. Glimm and D.H. Sharp. Prediction and the quantification of uncertainty. *Physica D*, 133:152–170, 1999.

- [47] J. Glimm and D.H. Sharp. Stochastic partial differential equations: selected applications in continuum physics. In R.A. Carmona and B. Rozovskii, editors, *Stochastic partial differential equations: six perspectives*. American Mathematical Society, 1999.
- [48] B. Gustafsson, H.-O. Kreiss, and J. Oliger. *Time dependent problems and difference methods*. John Wiley & Sons, Inc., New York, 1995.
- [49] J.M. Hammersley and D.C. Handscomb. *Monte Carlo methods*. Fletcher & Son Ltd., Norwich, 1967.
- [50] C. Hastings. *Approximations for Digital Computers*. Princeton University Press, 1955.
- [51] T.D. Hien and M. Kleiber. Stochastic finite element modelling in linear transient heat transfer. *Comput. Meth. Appl. Mech. Eng.*, 144:111–124, 1997.
- [52] T.D. Hien and M. Kleiber. On solving nonlinear transient heat transfer problems with random parameters. *Comput. Meth. Appl. Mech. Eng.*, 151:287–299, 1998.
- [53] R.G. Hills and T.G. Trucano. Statistical validation of engineering and scientific models: Background. Technical Report SAND99-1256, Sandia National Laboratories, 1999.
- [54] H. Holden, Oksendal, J. Ubøe, and T. Zhang. *Stochastic partial differential equations: a modeling, white noise functional approach*. Birkhäuser Boston, 1996.
- [55] W. Huang and D.M. Sloan. The pseudospectral method for solving differential eigenvalue problems. *J. Comput. Phys.*, 111:399–409, 1994.
- [56] K. Ito. Multiple Wiener integral. *J. Math. Soc. Japan*, 3:157–169, 1951.
- [57] M. Jardak, C.-H. Su, and G.E. Karniadakis. Spectral polynomial chaos solutions of the stochastic advection equation. *J. Sci. Comput.*, 17:319–338, 2002.
- [58] L. Kaiktsis, G.E. Karniadakis, and S.A. Orszag. Unsteadiness and convective instabilities in two-dimensional flow over a backward-facing step. *J. Fluid Mech.*, 321:157–187, 1996.

- [59] M.H. Kalos and P.A. Whitlock. *Monte Carlo methods: basics*. John Wiley & Sons, New York, 1986.
- [60] M. Kaminski and T.D. Hien. Stochastic finite element modeling of transient heat transfer in layered composites. *Int. Comm. Heat Mass Transfer*, 26(6):801–810, 1999.
- [61] G.E. Karniadakis and A. Beskok. *Micro flows: fundamentals and simulation*. Springer-Verlag, 2002.
- [62] G.E. Karniadakis, M. Israeli, and S.A. Orszag. High-order splitting methods for incompressible Navier-Stokes equations. *J. Comput. Phys.*, 97:414, 1991.
- [63] G.E. Karniadakis and S.J. Sherwin. *Spectral/hp Element Methods for CFD*. Oxford University Press, 1999.
- [64] M. Kleiber and T.D. Hien. *The stochastic finite element method*. John Wiley & Sons Ltd, 1992.
- [65] R. Koekoek and R.F. Swarttouw. The Askey-scheme of hypergeometric orthogonal polynomials and its q-analogue. Technical Report 98-17, Department of Technical Mathematics and Informatics, Delft University of Technology, 1998.
- [66] G. Kreiss and H.-O. Kreiss. Convergence to steady state of solution of Burgers' equation. *Appl. Numer. Math.*, 2:161–179, 1986.
- [67] J.G.L. Laforgue and R.E. O'Malley, Jr. On the motion of viscous shocks and the supersensitivity of their steady-state limits. *Methods Appl. Anal.*, 1:465–487, 1994.
- [68] J.G.L. Laforgue and R.E. O'Malley, Jr. Shock layer movement for Burgers' equation. *SIAM J. Appl. Math.*, 55:332–347, 1994.
- [69] J.G.L. Laforgue and R.E. O'Malley, Jr. Viscous shock motion for advection-diffusion equations. *Stud. Appl. Math.*, 95:147–170, 1995.

- [70] J.G.L. Laforgue and R.E. O'Malley, Jr. Exponential asymptotics, the viscous Burgers' equation, and standing wave solutions for a reaction-advection-diffusion model. *Stud. Appl. Math.*, 102:137–172, 1999.
- [71] O. Le Maitre, O. Knio, H. Najm, and R. Ghanem. A stochastic projection method for fluid flow: basic formulation. *J. Comput. Phys.*, 173:481–511, 2001.
- [72] O. Le Maitre, O. Knio, H. Najm, and R. Ghanem. Uncertainty propagation using Wiener-Haar expansions. *J. Comput. Phys.*, submitted, 2003.
- [73] O. Le Maitre, M. Reagan, H. Najm, R. Ghanem, and O. Knio. A stochastic projection method for fluid flow: random process. *J. Comput. Phys.*, 181:9–44, 2002.
- [74] P.-L. Liu and A. Der Kiureghian. Finite element reliability of geometrically nonlinear uncertain structures. *J. Eng. Mech.*, 117:1806–1825, 1991.
- [75] W.K. Liu, T. Belytschko, and A. Mani. Probabilistic finite elements for nonlinear structural dynamics. *Comput. Methods Appl. Mech. Engrg.*, 56:61–81, 1986.
- [76] W.K. Liu, T. Belytschko, and A. Mani. Random field finite elements. *Int. J. Num. Meth. Engrg.*, 23(10):1831–1845, 1986.
- [77] W.K. Liu, T. Belytschko, and A. Mani. Applications of probabilistic finite element methods in elastic/plastic dynamics. *J. Engrg. Ind., ASME*, 109:2–8, 1987.
- [78] W.K. Liu, G.H. Besterfield, and T. Belytschko. Variational approach to probabilistic finite elements. *J. Eng. Mech.*, 114(12):2115–2133, 1988.
- [79] M. Loève. *Probability Theory, Fourth edition*. Springer-Verlag, 1977.
- [80] W.L. Loh. On Latin hypercube sampling. *Ann. Stat.*, 24(5):2058–2080, 1996.
- [81] J. Lorentz. Nonlinear singular perturbation problems and the Engquist-Osher difference scheme. Technical Report 8115, University of Nijmegen, Nijmegen, The Netherlands, 1981.
- [82] N. Madras. *Lectures on Monte Carlo methods*. American Mathematical Society, Providence, RI, 2002.

- [83] L. Mathelin, M.Y. Hussaini, and T.A. Zang. Stochastic approaches to uncertainty quantification in CFD simulations. *Numer. Algo.*, submitted, 2003.
- [84] L. Mathelin, M.Y. Hussaini, T.A. Zang, and F. Bataille. Uncertainty propagation for turbulent, compressible flow in a quasi-1d nozzle using stochastic methods. In *16th AIAA Computational Fluid Dynamics Conference, June 23-26, Orlando, FL*, volume AIAA 2003-4240, 2003.
- [85] H.G. Matthies and C. Bucher. Finite elements for stochastic media problems. *Comput. Methods Appl. Mech. Engrg.*, 168:3–17, 1999.
- [86] G.B. McFadden, B.T. Murray, and R.F. Boisvert. Elimination of spurious eigenvalues in the Chebyshev tau spectral method. *J. Comput. Phys.*, 91:228–239, 1990.
- [87] U.B. Mehta. Some aspects of uncertainty in computational fluid dynamics results. *J. Fluids Eng.*, 113:538–543, 1991.
- [88] J.D. Murray. *Asymptotic analysis*. Springer-Verlag, New York, 1984.
- [89] A.H. Nafeh. *Perturbation methods*. Wiley, New York, 1973.
- [90] S.P. Neuman. Stochastic approach to subsurface flow and transport: a view of the future. In G. Dagan and S.P. Neuman, editors, *Subsurface flow and transport: a stochastic approach*, pages 231–241. Cambridge University Press, 1997.
- [91] H. Niederreiter. *Random number generation and Quasi-Monte Carlo methods*. SIAM, 1992.
- [92] H. Niederreiter, P. Hellekalek, G. Larcher, and P. Zinterhof. *Monte Carlo and Quasi-Monte Carlo methods 1996*. Springer-Verlag, 1998.
- [93] W.L. Oberkampf and T.G. Trucano. Validation Methodology in Computational Fluid Dynamics. Technical Report AIAA 2000-2549, Sandia National Laboratories, Albuquerque, New Mexico, 2000.

- [94] W.L. Oberkampf, T.G. Trucano, and C. Hirsch. Verification, validation, and predictive capability in computational engineering and physics. Technical Report SAND2003-3769, Sandia National Laboratories, 2003.
- [95] H. Ogura. Orthogonal functionals of the Poisson process. *IEEE Trans. Info. Theory*, IT-18:473–481, 1972.
- [96] R.E. O'Malley. *Introduction to singular perturbations*. Academic Press, New York, 1974.
- [97] S.A. Orszag. Accurate solution of the Orr-Sommerfeld stability equation. *J. Fluid Mech.*, 50:689–703, 1971.
- [98] S.A. Orszag and L.R. Bissonnette. Dynamical properties of truncated Wiener-Hermite expansions. *Phys. Fluids*, 10:2603–2613, 1967.
- [99] G. Papanicolaou and X. Xin. Reaction diffusion front in periodically layered media. *J. Stat. Phys.*, 63:915–932, 1991.
- [100] G.C. Papanicolaou. Diffusion in random media. In J.B. Keller, D. McLaughlin, and G.C. Papanicolaou, editors, *Surveys in Applied Mathematics*, pages 205–255. Plenum Press, 1995.
- [101] Ph. Renard and G. de Marsily. Calculating equivalent permeability: a review. *Adv. Water Resour.*, 20:253–278, 1997.
- [102] H.J. Pradlwarter, G.I. Schuëller, P. Jehlicka, and H. Steinhilber. Structural failure probabilities of the HDR-containment. *J. Nuclear Eng. Design*, 128:237–246, 1991.
- [103] H.J. Pradlwarter, G.I. Schuëller, and P.G. Melnik-Melnikov. Reliability of MDOF-systems. *Prob. Eng. Mech.*, 9:235–243, 1994.
- [104] M.R. Rajaschekhar and B.R. Ellingwood. A new look at the response surface approach for reliability analysis. *Struc. Safety*, 123:205–220, 1993.
- [105] L.G. Reyna and M.J. Ward. On exponential ill-conditioning and internal layer behavior. *Numer. Funct. Anal. Optim.*, 16:475–500, 1995.

- [106] L.G. Reyna and M.J. Ward. On exponential slow motion of a viscous shock. *Comm. Pure Appl. Math.*, 48:79–120, 1995.
- [107] P.J. Roache. Quantification of uncertainty in computational fluid dynamics. *Annu. Rev. Fluid. Mech.*, 29:123–160, 1997.
- [108] P.J. Roache. Code verification by the method of manufactured solutions. *J. Fluids Eng.*, 124(1):4–10, 2002.
- [109] R.Y. Rubinstein. *Simulation and the Monte Carlo method*. John Wiley & Sons, New York, 1981.
- [110] L. Ryzhik, G. Papanicolaou, and J.B. Keller. Transport equations for elastic and other waves in random media. *Wave Motion*, 24:327–370, 1996.
- [111] W. Schoutens. *Stochastic processes in the Askey scheme*. PhD thesis, K.U. Leuven, 1999.
- [112] W. Schoutens. *Stochastic Processes and orthogonal polynomials*. Springer-Verlag, New York, 2000.
- [113] G.I. Schuëller, H.J. Pradlwarter, and C.G. Bucher. Efficient computational procedures for reliability estimate of MDOF-systems. *Int. J. Nonlinear Mech.*, 26:961–974, 1991.
- [114] M. Shinozuka and G. Deodatis. Response variability of stochastic finite element systems. *J. Eng. Mech.*, 114(3):499–519, 1988.
- [115] I.M. Sobol. *A primer for the Monte Carlo method*. CRC Press, 1994.
- [116] M. Stein. Large sample properties of simulations using Latin Hypercube Sampling. *Technometrics*, 29(2):143–151, 1987.
- [117] G. Szegö. *Orthogonal Polynomials*. American Mathematical Society, Providence, RI, 1939.
- [118] T. Takada. Weighted integral method in multi-dimensional stochastic finite element analysis. *Prob. Eng. Mech.*, 5(4):158–166, 1990.

- [119] T. Takada. Weighted integral method in stochastic finite element analysis. *Prob. Eng. Mech.*, 5(3):146–156, 1990.
- [120] M. Van Dyke. *Perturbations methods in fluid mechanics*. Panabolic Press, Stanford, 1975.
- [121] E.H. Vanmarcke and M. Grigoriu. Stochastic finite element analysis of simple beams. *J. Eng. Mech.*, 109(5):1203–1214, 1983.
- [122] X. Wan, D. Xiu, and G.E. Karniadakis. Stochastic solutions for the two-dimensional advection-diffusion equation. *SIAM J. Sci. Comput.*, submitted, 2003.
- [123] P. Whittle. On stationary processes in the plane. *Biometrika*, 41:434–449, 1954.
- [124] N. Wiener. The homogeneous chaos. *Amer. J. Math.*, 60:897–936, 1938.
- [125] C.H.K. Williamson. Vortex dynamics in the cylinder wake. *Ann. Rev. Fluid Mech.*, 28:477–539, 1996.
- [126] C.L. Winter, C.M. Newman, and S.P. Neuman. A perturbative expansion for diffusion in a random velocity field. *SIAM J. Appl. Math.*, 44(2):411–424, 1984.
- [127] C.L. Winter and D.M. Tartakovsky. Mean flow in composite porous media. *Geophy. Res. Lett.*, 27:1759–1762, 2000.
- [128] C.L. Winter and D.M. Tartakovsky. Groundwater flow in heterogeneous composite aquifers. *Water Resour. Res.*, 38:10.1029/2001WR000450, 2002.
- [129] D. Xiu and G.E. Karniadakis. Modeling uncertainty in steady state diffusion problems via generalized polynomial chaos. *Comput. Methods Appl. Math. Engrg.*, 191:4927–4948, 2002.
- [130] D. Xiu and G.E. Karniadakis. The Wiener-Askey polynomial chaos for stochastic differential equations. *SIAM J. Sci. Comput.*, 24(2):619–644, 2002.
- [131] D. Xiu and G.E. Karniadakis. Modeling uncertainty in flow simulations via generalized polynomial chaos. *J. Comput. Phys.*, 187:137–167, 2003.

- [132] D. Xiu and G.E. Karniadakis. A new stochastic approach to transient heat conduction modeling with uncertainty. *Inter. J. Heat Mass Trans.*, in press, 2003.
- [133] D. Xiu and G.E. Karniadakis. On the well-posedness of generalized polynomial chaos expansions for the stochastic diffusion equation. *SIAM J. Numer. Anal.*, submitted, 2003.
- [134] D. Xiu and G.E. Karniadakis. Supersensitivity due to uncertain boundary conditions. *Int. J. Numer. Meth. Engng.*, submitted, 2003.
- [135] D. Xiu, D. Lucor, C.-H. Su, and G.E. Karniadakis. Stochastic modeling of flow-structure interactions using generalized polynomial chaos. *J. Fluids Eng.*, 124(1):51–59, 2002.
- [136] F. Yamazaki, M. Shinozuka, and G. Dasgupta. Neumann expansion for stochastic finite element analysis. *J. Eng. Mech.*, 114(8):1335–1354, 1988.
- [137] D. Zhang. *Stochastic methods for flow in porous media*. Academic Press, 2002.
- [138] W.Q. Zhu, Y.J. Ren, and W.Q. Wu. Stochastic FEM based on local average of random vector fields. *J. Eng. Mech.*, 118(3):496–511, 1992.
- [139] W.Q. Zhu and W.Q. Wu. A stochastic finite element method for real eigenvalue problems. *Prob. Eng. Mech.*, 6:228–232, 1991.